

MULTIRESOLUTION MOLECULAR MECHANICS: THEORY AND APPLICATIONS

by

Qingcheng Yang

B.S. in Engineering Mechanics, Wuhan University, 2007

M.S in Solid Mechanics, Beihang University, 2010

Submitted to the Graduate Faculty of
Swanson School of Engineering in partial fulfillment
of the requirements for the degree of
Doctor of Philosophy

University of Pittsburgh

2016

UNIVERSITY OF PITTSBURGH
SWANSON SCHOOL OF ENGINEERING

This dissertation was presented

by

Qingcheng Yang

It was defended on

March 17, 2016

and approved by

William S. Slaughter, Ph.D., Associate Professor,

Department of Mechanical Engineering and Materials Science

Guofeng Wang, Ph.D., Associate Professor,

Department of Mechanical Engineering and Materials Science

Ivan Yotov, Ph.D., Professor,

Department of Mathematics

Dissertation Director: Albert C. To, Ph.D., Associate Professor

Department of Mechanical Engineering and Materials Science

Copyright © by Qingcheng Yang

2016

MULTIRESOLUTION MOLECULAR MECHANICS: THEORY AND APPLICATIONS

Qingcheng Yang, Ph.D.

University of Pittsburgh, 2016

A general mathematical framework, Multiresolution Molecular Mechanics (MMM), is proposed to consistently coarse-grain molecular mechanics at different resolutions in order to extend the length scale of nanoscale modeling of crystalline materials. MMM is consistent with molecular mechanics in the sense that the constitutive description such as energy and force calculations is exactly the same as molecular mechanics and no empirical and phenomenological constitutive relationships in continuum mechanics are employed. As such, MMM can converge to full molecular mechanics naturally.

As many coarse-graining approaches, MMM is based on approximating the total potential energy of a full atomistic model. Analogous to quadrature rules employed to evaluate energy integrals in finite element method (FEM), a summation rule is required to evaluate finite energy summations. Most existing summation rules are specifically designed for the linear interpolation shape function and their extensions to high order shape functions are currently not clear. What distinguishes MMM from existing works is that MMM proposes a novel summation rule framework SR^{MMM} that is valid and consistent for general shape functions. The key idea is to analytically derive the energy distribution of the coarse-grained atomistic model and then choose some quadrature-type (sampling) atoms to accurately represent the derived energy distribution for a given shape function. The optimal number, weight and position of sampling atoms are also determined accordingly, similar to the Gauss quadrature in FEM. The governing equations are then derived following the variational principle.

The proposed SR^{MMM} is verified and validated numerically and compared against many other summation rules such as Gauss-quadrature-like rule. And SR^{MMM} demonstrates better performance in terms of accuracy and computational cost. The convergence property of MMM is also studied numerically and MMM shows FEM-like behavior under certain circumstance. In addition, MMM has been applied to solve problems such as crack propagation, atomic sheet shear, beam bending and surface relaxations by employing high order interpolation shape functions in one (1D), two (2D) and three dimensions (3D) .

TABLE OF CONTENTS

PREFACE.....	XXI
1.0 INTRODUCTION.....	1
1.1 EXISTING MULTISCALE APPROACHES	3
1.2 SURFACE EFFECT ON NANOSIZED STRUCTURES	7
1.3 RESEARCH OBJECTIVE AND OUTLINE.....	10
1.3.1 Research objective	10
1.3.2 Outline	12
2.0 MULTIREOLUTION MOLECULAR MECHANICS	15
2.1 OVERVIEW.....	15
2.2 MMM SUMMATION RULE SR^{MMM}	17
2.3 SR^{MMM} DECOMPOSITION SR^B AND SR^S	23
2.3.1 Why the decomposition is needed	23
2.3.2 Examples of employed bulk and surface summation rules.....	24

2.3.3	Discussion of several summation rules	29
2.4	REMARKS OF SR ^{MMM} ON NONLINEAR POTENTIALS	34
2.5	SUMMARY OF ATOM CLASSIFICATION.....	37
2.6	GOVERNING EQUATIONS	39
2.7	SUMMARY	40
3.0	NUMERICAL VALIDATION OF BULK SUMMATION RULE: SR ^B	42
3.1	ERROR SOURCES	42
3.2	ERROR NORMS	45
3.3	DEFINITIONS OF COMPARED SUMMATION RULES.....	48
3.4	VALIDATION FOR SPRING POTENTIAL	58
3.4.1	1D quadratic tensile deformation.....	58
3.4.2	2D non-homogeneous shear deformation.....	63
3.5	SR ^B EXTENSION AND VALIDATION FOR LENNARD-JONES POTENTIAL.....	66
3.5.1	1D quadratic tensile deformation.....	67
3.5.2	2D non-homogeneous shear deformation	70
3.6	COMPARISON OF INTERFACE COMPATIBILITY	72
3.7	SOME APPLICATIONS	77

3.7.1	2D atomic sheet tensile model	77
3.7.2	2D atomic sheet shear model	82
3.7.3	2D atomic beam bending model	83
3.7.4	2D crack propagation	86
3.8	IRREGULAR ELEMENTS.....	90
3.8.1	2D irregular atomic sheet shear model.....	91
3.8.2	Mapped elements	95
3.9	SUMMARY	96
4.0	NUMERICAL VALIDATION OF SURFACE SUMMATION RULE SR ^S	98
4.1	2D SURFACE RELAXATION	98
4.2	3D SURFACE RELAXATION	102
4.3	SUMMARY	111
5.0	NUMERICAL CONVERGENCE AND ERROR STRUCTURE ANALYSIS ..	113
5.1	CONVERGENCE STUDY	113
5.1.1	1D convergence test	115
5.1.1.1	Quadratic-deformation force loading: harmonic potential	118
5.1.1.2	Quadratic-deformation force loading: Lennard-Jones potential .	120

5.1.1.3	Uniformly distributed force loading: harmonic potential.....	121
5.1.1.4	Uniformly distributed force loading: Lennard-Jones potential ...	122
5.1.1.5	Random force loadings of uniform distribution: harmonic and LJ potentials.....	123
5.1.2	2D convergence test	125
5.1.2.1	Atomic spring beam with the corresponding quadratic-deformation force loading	127
5.1.2.2	Atomic LJ beam with the corresponding quadratic-deformation force loading	130
5.1.2.3	Atomic beams with uniformly distributed force loadings: spring and LJ potentials.....	131
5.1.2.4	Atomic beams with random force loadings of uniform distribution: spring and LJ potentials.....	132
5.2	ERROR STRUCTURE ANALYSIS	134
5.2.1	Error structure analysis of 1D atomic models	134
5.2.1.1	Quadratic-deformation loadings	134
5.2.1.2	Uniformly distributed force loadings	137
5.2.1.3	Random force loadings of uniform distribution.....	140
5.2.2	Error structure analysis of 2D atomic models	144
5.2.2.1	Quadratic-deformation loadings	144

5.2.2.2	Uniformly distributed force loadings	146
5.2.2.3	Random force loadings of uniform distribution.....	149
5.2.3	An analysis of sampling errors	151
5.3	SUMMARY	154
6.0	CONCLUSIONS AND OUTLOOK.....	156
6.1	CONTRIBUTIONS	156
6.2	FUTURE OUTLOOK	158
	BIBLIOGRAPHY	163

LIST OF TABLES

Table 2.1: A qualitatively comparison of several different summation rules.....	34
Table 2.2: The employed bulk summation rule SR^B for different element types	36
Table 2.3: Classification of different atom types in MMM from the perspective of degrees of freedom (DOFs)	39
Table 2.4: Classification of different atom types in MMM from the perspective of energy sampling.....	39
Table 3.1: Errors in the solution of the 1D non-local spring problem obtained via different summation rules and different choices of positions of primary sampling atoms with linear element.	61
Table 3.2: Errors in the solution of the 1D non-local spring problem obtained via different summation rules and different choices of positions of primary sampling atoms with quadratic element.	62
Table 3.3: Errors in the solution of the 2D non-local spring shear problem obtained via different summation rules and different choices of positions of primary sampling atoms with linear element.	64
Table 3.4: Errors in the solution of the 2D non-local spring shear problem obtained via different summation rules and different choices of positions of primary sampling atoms with bilinear element Q4.....	65
Table 3.5: Errors in the solution of the 2D non-local spring shear problem obtained via different summation rules and different choices of positions of primary sampling atoms with quadratic triangle element T6.	66

Table 3.6: Errors in the solution of the 1D non-local LJ problem obtained via different summation rules and different choices of positions of primary sampling atoms with linear element.....	68
Table 3.7: Errors in the solution of the 1D non-local LJ problem obtained via different summation rules and different choices of positions of primary sampling atoms with quadratic element.....	69
Table 3.8: Errors in the solution of the 2D LJ shear problem obtained via different summation rules and different choices of positions of primary sampling atoms with linear element.	70
Table 3.9: Errors in the solution of the 2D LJ shear problem obtained via different summation rules and different choices of positions of primary sampling atoms with bilinear element Q4.....	71
Table 3.10: Errors in the solution of the 2D non-local LJ shear problem obtained via different summation rules and different choices of positions of primary sampling atoms with quadratic triangle element T6.	72
Table 3.11: Errors in the solution of the 2D LJ tensile problem obtained via different summation rules and different choices of positions of primary sampling atoms with bilinear element Q4.....	78
Table 3.12: Errors in the solution of the 2D LJ tensile problem obtained via different summation rules and different choices of positions of primary sampling atoms with quadratic triangle element T6.	80
Table 3.13: Errors in the solution of the 2D LJ shear problem obtained via different summation rules and different choices of positions of primary sampling atoms with bilinear element Q4.....	83
Table 3.14: Errors in the solution of the 2D LJ shear problem obtained via different summation rules and different choices of positions of primary sampling atoms with quadratic triangle element T6.	83
Table 3.15: Errors in the solution of the 2D LJ beam bending problem obtained via different summation rules and different choices of positions of primary sampling atoms with linear element T3	86

Table 3.16: Errors in the solution of the 2D LJ beam bending problem obtained via different summation rules and different choices of positions of primary sampling atoms with quadratic triangle element T6	86
Table 3.17: Errors in the solution of the 2D LJ biquadratic shear problem obtained via the proposed summation rules SR^B with different choices of positions of primary sampling atoms using irregular bilinear element Q4 with relatively large element size.....	93
Table 3.18: Errors in the solution of the 2D LJ biquadratic shear problem obtained via the proposed summation rules SR^B with different choices of positions of primary sampling atoms using irregular bilinear element Q4 with relatively small element size	93
Table 4.1: Normalized displacement comparison between full atomistic (FA) simulation and MMM calculation at the upper right corner and the middle of the edge at the right hand side	100
Table 4.2: Different types of errors in displacement and energy field in the 2D example	102
Table 4.3: Normalized displacement comparison between full atomistic (FA) simulation and MMM calculation at corner, middle of edge and face center in the 3D example.....	105
Table 4.4: Different types of errors in displacement and energy field in the 3D example	106

LIST OF FIGURES

Figure 1.1: Schematic illustration of point defect (a) and grain boundary (b)	2
Figure 1.2: Schematic of edge dislocation migration due to applied shear force	3
Figure 1.3: Hall-Petch Strengthening is constrained by the size of dislocations. Once the grain size d reaches around 10 nanometers, GB-based mechanism occurs to decrease the yield stress.....	4
Figure 1.4: Schematically Overview of the MMM methodology in analogy to Finite Element Method (FEM): FEM for continuum modeling (a) and MMM for discrete modeling (b). The meaning of different symbols will be explained in Section 2.1.	11
Figure 2.1: Schematically illustration of energy distributions for coarse-grained continuum model (a) and coarse-grained atomistic model (b). Solid line denotes a continuous curve and dashed line a curve passing through discrete energy point for each atom. The solid x axis means x_c continuously spans the continuum domain (a) and the dashed x axis represents that x_a discretely spans the space (b).....	22
Figure 2.2: Energy distribution for atoms in bulk region and atoms in surface areas.	24
Figure 2.3: Employed SR^{MMM} ($SR^B + SR^S$) in 2D for the selected 4-node quadrilateral element: SR^{MMM} for an element that contains a corner atom (a); SR^{MMM} for an element that contains only one surface edge (b); SR^{MMM} for an element that contains a corner atom and non-bulk layers (dashed line) (c); SR^{MMM} for an element that contains one surface edge and one non-bulk layer (d). SR^B is employed for bulk non-sampling atoms ($NSAs$) and SR^S for surface and non-bulk $NSAs$. Dashed rectangle denotes the element bulk region.	27
Figure 2.4: Schematically illustration of Quasicontinuum method with the respectively Cauchy-Born rule (a), cluster rule (SR^{CR}) (b), quadrature-type rule (SR^{QR}) and MMM with SR^{MMM} , using two 1D linear elements in the coarse-grained region.....	31

Figure 2.5: A schematically illustration of the Cauchy-Born rule in 2D: an atomic unit cell centered at a quadrature point (blue dot) is assumed to deform uniformly according to the deformation gradient \mathbf{F} at the quadrature point	32
Figure 2.6: A MMM model where both atomistic and coarse-grained regions exist. Molecular mechanics (black area) is employed to capture crack propagation and SR^{MMM} is employed in the coarse-grained region far away from the crack.....	38
Figure 3.1: Schematically demonstration of error sources and types: Model A: full atomistic model; Model B: a general MMM model with SR^{MMM} ; Model C: a specifically designed model where the energy of each atom is explicitly considered. Discretization error is fixed for a given mesh.....	44
Figure 3.2: Schematically illustration of the possibility in an error estimator that the distance between different displacement fields could be very large even though they produce the same potential energy scalar E_0 : \mathbf{U}^{FA} is from full atomistic simulation and \mathbf{U} from any other approximation	47
Figure 3.3: Schematic illustrations of primary sampling atom selections for different summation rules employed for 1D linear element: Gauss1 and $\text{SR}^{\text{B-1}}$ (a), $\text{SR}^{\text{B-2}}$ (b), SR^{naive} (c) and Scheme 0p*s (d).....	50
Figure 3.4: Schematic illustrations of primary sampling atom selections for different summation rules employed for 1D quadratic element: Gauss1 (a), Gauss2 (b), Bisection (c), $\text{SR}^{\text{B-2}}$ (d), $\text{SR}^{\text{B-1}}$ (e), Gauss4 (f), quartering (g) and Scheme 0p*s (h).....	52
Figure 3.5: Schematic illustrations of primary sampling atom selections for different summation rules employed for 2D linear triangle element (T3): Gauss1 and $\text{SR}^{\text{B-1}}$ (a), $\text{SR}^{\text{B-2}}$ (b), SR^{naive} (c) for spring model and SR^{naive} (d) for LJ model.	54
Figure 3.6: Schematic illustrations of primary sampling atom selections for different summation rules employed for 2D bilinear element (Q4). Part I: Gauss2 (a), Gauss3 (b), Bisection (c) and Trisection(d).	55
Figure 3.7: Schematic illustrations of primary sampling atom selections for different summation rules employed for 2D bilinear element (Q4). Part II: $\text{SR}^{\text{B-1}}$ (a) and $\text{SR}^{\text{B-2}}$ (b).	56
Figure 3.8: Schematic illustrations of primary sampling atom selections for different summation rules employed for 2D quadratic triangle element (T6). Part I: Gauss1 (a), Gauss2 (b), Gauss3(c), Gauss4 and $\text{SR}^{\text{B-1}}$ (d).	57

Figure 3.9: Schematic illustrations of primary sampling atom selections for different summation rules employed for 2D quadratic triangle element (T6). Part II: Gauss5 (a) and SR^B -2 (b).	58
Figure 3.10: Comparison between full atomistics, MMM and several other multiscale methods for the 1D non-local spring model under uniform deformation: MMM model (a), strain distribution of different methods near the interface (b)	74
Figure 3.11: Comparison between full atomistics, MMM and several other multiscale methods for the 1D non-local spring model under inhomogeneous deformation: MMM model (a), strain distribution of different methods near the interface (b)	75
Figure 3.12: Comparison between full atomistics, MMM and several other multiscale methods for the 1D non-local spring model under point force at interface: MMM model (a), strain distribution of different methods near the interface (b)	76
Figure 3.13: Schematic illustrations of primary sampling atom selections for the MMM models with bilinear element (Q4) and summation rules SR^B -1 (a) and SR^B -2 (b).	79
Figure 3.14: Schematic illustrations of primary sampling atom selections for the MMM models with quadratic triangle element (T6) and summation rules SR^B -1 (a) and SR^B -2 (b).	81
Figure 3.15: Snapshots from crack propagation of full atomistic (left) and MMM model I (right) simulations	87
Figure 3.16: Snapshots from crack propagation of full atomistic (left) and MMM model II (right) simulations	88
Figure 3.17: Stress-strain curves of full atomistic and MMM model I simulations of crack propagation	89
Figure 3.18: Stress-strain curves of full atomistic and MMM model II simulations of crack propagation	90
Figure 3.19: Schematic illustrations of primary sampling atom selections for the MMM models using irregular bilinear element (Q4) with relatively large element size and summation rules SR^B -1 and SR^B -2 employed in Section 5: SR^B -1 (a) and SR^B -2 (b).	92

Figure 3.20: Schematic illustrations of primary sampling atom selections for the MMM models using irregular bilinear element (Q4) with relatively small element size and summation rules SR^B -1 and SR^B -2 employed in Section 5: (a) SR^B -1 and (b) SR^B -2	94
Figure 4.1: The employed 4-node quadrilateral mesh (dashed line) and summation rule SR^{MMM} for the 2D surface relaxation problem: SR^B for the bulk region and SR^S for the surface and non-bulk region	100
Figure 4.2: Comparison of displacement distributions from full atomistic (FA) calculation and MMM: the x -displacement distributions from FA (a) and MMM (b); the y -displacement distributions from FA (c) and MMM (d)	101
Figure 4.3: The employed 8-node quadrilateral mesh (dashed line) for the 3D problem: the blue dots on the free surfaces and edges shows the applied SR^S ; SR^S and SR^B are also utilized for the non-bulk layers and bulk layers, respectively, and are invisible.....	103
Figure 4.4: The respective free surface, non-bulk and bulk layers of the 3D example: SR^S is applied to both free surface and non-bulk layers and SR^B is employed for bulk layers.	104
Figure 4.5: Schematically demonstration of the employed SR^B with 8-node hexahedral element for bulk layers: red dots are the nodal atoms and blue dots represent the selected primary sampling atoms ($PSAs$)	105
Figure 4.6: Comparison of x -displacement distributions on surfaces from full atomistics (FA) and MMM: $+x$ -displacement from FA (a) and MMM (b); $-x$ -displacement from FA (c) and MMM (d)	107
Figure 4.7: Comparison of y -displacement distributions on surfaces from full atomistics (FA) and MMM: $+y$ -displacement from FA (a) and MMM (b); $-y$ -displacement from FA (c) and MMM (d)	108
Figure 4.8: Comparison of z -displacement distributions on surfaces from full atomistics (FA) and MMM: $+z$ -displacement from FA (a) and MMM (b); $-z$ -displacement from FA (c) and MMM (d)	109
Figure 4.9: Comparison of x -displacement distributions from bulk along the plane $x = 0$ from full atomistics (FA) (a) and MMM (b)	110

Figure 4.10: Comparison of y -displacement distributions from bulk along the plane $y = 0$ from full atomistics (FA) (a) and MMM (b)	110
Figure 4.11: Comparison of z -displacement distributions from bulk along the plane $z = 0$ from full atomistics (FA) (a) and MMM (b)	111
Figure 5.1: Four different MMM models with the corresponding sampling schemes with an element size of $16r_0$ (r_0 is the initial atomic spacing): scheme 1p0s (a); scheme 1p~s (b); scheme 1p@s (c) and scheme 0p*s (d).....	114
Figure 5.2: Exact solutions from atomistics for the 1D spring model for the quadratic-deformation loading (black), the uniform force loading (blue) and the random force loading of uniform distribution (red)	117
Figure 5.3: Exact solutions from atomistics for the 1D LJ model for the quadratic-deformation loading (black), the uniform force loading (blue) and the random force loading of uniform distribution (red)	117
Figure 5.4: Convergence of the 1D spring model subject to the corresponding quadratic-deformation force loading in the relative displacement error norm (a) and the relative energy error norm (b); convergence of the 1D LJ model subject to the corresponding quadratic-deformation force loading in the relative displacement error norm (c) and the relative energy error norm (d).....	119
Figure 5.5: Convergence of the 1D spring model subject to the corresponding uniformly distributed force loading in the relative displacement error norm (a) and the relative energy error norm (b); convergence of 1D LJ model subject to the corresponding uniformly distributed force loading in the relative displacement error norm (c) and the relative energy error norm (d).....	122
Figure 5.6: Convergence of the 1D spring model subject to the corresponding random force loading of uniform distribution in the relative displacement error norm (a) and the relative energy error norm (b); convergence of the 1D LJ model subject to the corresponding random force loading of uniform distribution in the relative displacement error norm (c) and the relative energy error norm (d)	124
Figure 5.7: 2D mesh with uniform element size $h_x = 24r_0$ and $h_y = 63r_0$ for scheme 1p0s: interpolating rep-atoms, primary sampling atoms, non-sampling atoms are represented as red, blue and gray dots, respectively.....	126

Figure 5.8: A 2D beam commonly employed in solid mechanics to test the convergence of FEM	128
Figure 5.9: Convergence of the 2D <i>Us1</i> -spring model subject to the corresponding quadratic-deformation force loading in the relative displacement error norm (a) and the relative energy error norm (b); convergence of the 2D <i>Us2</i> -spring model subject to the corresponding quadratic-deformation force loading in the relative displacement error norm (c) and the relative energy error norm (d); convergence of the 2D LJ model subject to the corresponding quadratic-deformation force loading in the relative displacement error norm (e) and the relative energy error norm (f)	129
Figure 5.10: Convergence of 2D <i>Us2</i> -spring model subject to the corresponding uniformly distributed force loading in the relative displacement error norm (a) and the relative energy error norm (b); convergence of 2D LJ model subject to the corresponding uniformly distributed force loading in the relative displacement error norm (c) and the relative energy error norm (d).....	132
Figure 5.11: Convergence of 2D <i>Us2</i> -spring model subject to the corresponding random force loading of uniform distribution in the relative displacement error norm (a) and the relative energy error norm (b); convergence of 2D LJ model subject to the corresponding random force loading of uniform distribution in the relative displacement error norm (c) and the relative energy error norm (d)	133
Figure 5.12: Error structure analysis of scheme 1p0s ((a) and (b)), 1p~s ((c) and (d))and 1p@s ((e) and (f)) for the 1D spring model with the corresponding quadratic-deformation force loading.....	136
Figure 5.13: Error structure analysis of scheme 1p0s ((a) and (b)), 1p~s ((c) and (d))and 1p@s ((e) and (f))for the 1D LJ model with the corresponding quadratic-deformation force loading.....	137
Figure 5.14: Error structure analysis of scheme 1p0s ((a) and (b)), 1p~s ((c) and (d)) and 1p@s ((e) and (f)) for the 1D spring model with the corresponding uniformly distributed force loading.....	139
Figure 5.15: Error structure analysis of scheme 1p0s ((a) and (b)), 1p~s ((c) and (d)) and 1p@s ((e) and (f)) for the 1D LJ model with the corresponding uniformly distributed force loading.....	140

Figure 5.16: Error structure analysis of scheme 1p0s ((a) and (b)), 1p~s ((c) and (d)) and 1p@s ((e) and (f)) for the 1D spring model with the corresponding random force loading of uniform distribution	142
Figure 5.17: Error structure analysis of scheme 1p0s ((a) and (b)), 1p~s ((c) and (d)) and 1p@s ((e) and (f)) for the 1D LJ model with the corresponding random force loading of uniform distribution	143
Figure 5.18: Error structure analysis of scheme 1p0s ((a) and (b)), 1p~s ((c) and (d)) and 1p@s ((e) and (f)) for the 2D $Us2$ -spring model with the corresponding quadratic-deformation force loading	145
Figure 5.19: Error structure analysis of scheme 1p0s ((a) and (b)), 1p~s ((c) and (d)) and 1p@s ((e) and (f)) for the 2D LJ model with the corresponding quadratic-deformation force loading.....	146
Figure 5.20: Error structure analysis of scheme 1p0s ((a) and (b)), 1p~s ((c) and (d)) and 1p@s ((e) and (f)) for the 2D $Us2$ -spring model with the corresponding uniformly distributed force loading	148
Figure 5.21: Error structure analysis of scheme 1p0s ((a) and (b)), 1p~s ((c) and (d)) and 1p@s ((e) and (f)) for the 2D LJ model with the corresponding uniformly distributed force loading.....	149
Figure 5.22: Error structure analysis of scheme 1p0s ((a) and (b)), 1p~s ((c) and (d)) and 1p@s ((e) and (f)) for the 2D $Us2$ -spring model with the corresponding random force loading of uniform distribution.....	150
Figure 5.23: Error structure analysis of scheme 1p0s ((a) and (b)), 1p~s ((c) and (d)) and 1p@s ((e) and (f)) for the 2D LJ model with the corresponding random force loading of uniform distribution	151
Figure 5.24: Sampling error norm comparasion of the four MMM schemes for the 2D LJ model with the corresponding random force loading of uniform distribution in displacement error norm (a) and energy error norm (b)	153

PREFACE

With a strong desire to enhance my understanding of mechanics, particularly computational mechanics, I jointed the Ph.D. program at University of Pittsburgh. Looking back on my time here, I am grateful to many people who have supported me in different ways to accomplish this thesis. I would like to mention those who have helped the most here.

I would like to express my gratitude to my advisor Dr. Albert C. To for bringing me into the multiscale modeling world when I just started my Ph.D.. Since then, he has been providing consistent support and giving me freedom to explore different ideas. He also has provided me many opportunities to attend conferences and deliver presentations, and helped me polish my communication skills, which has been a valuable training for my future career.

I am also thankful to my committee members, Dr. Ivan Yotov, Dr. Guofeng Wang and Dr. William Slaughter, for their precious time and insightful suggestions. I am especially indebted to Dr. Ivan Yotov for what I learned from his math classes, Dr. Guofeng Wang for his helpful comments during the weekly joint group seminar and Dr. Rong Tian for his advice and guidance when I was at Chinese Academy of Science.

My special thank goes to group members, Dr. Yao Fu, Dr. Emre Biyikli, Dr. Pu Zhang, Lin Cheng, and many others for the discussions and friendship. Moreover, the basketball team I played with in the past five years certainly deserves my gratitude for the sweating and brain refreshment.

Finally, I am highly grateful to my wife Shiqi Ma, our baby Andy Yang, my father Jiayou Yang, my mother Qingxiu Tan, my sister Ying Yang, brother-in-law Huakai Lin; my father-in-law Yanjun Ma and mother-in-law Yanjie Zhang. Your love is the reason I am. You are my world.

1.0 INTRODUCTION

Material response of crystalline solids is characterized by the nucleation and dynamics of defects such as point defect (vacancies, interstitials, impurities) (Figure 1.1a), line defects (dislocations in Figure 1.2) and planar defects (grain boundaries, surfaces, crack, etc.) (Figure 1.1b). Material defects usually exist in localized regions but affect the overall mechanical behavior of materials. Such localized areas always involve more complicated deformations such as bond breaking and rearrangement and thus require atomistic modeling to resolve the details of the deformation mechanisms. For example, grain boundary (GB) strengthening mechanism [1-4] can be used to increase material yield strength by changing their average grain size. This mechanism is based on the observation that GB boundaries impede dislocation movement and the amount of dislocations within a grain affect how easily dislocations can move across GB boundaries and travel from grain to grain. This strengthening mechanism is described by the Hall-Petch relationship (Figure 1.3) [1, 2]. Decreasing grain size can dramatically increase the yield strength until a critical point where grain size is around 10 nanometers (nm). However, the dependency of yield stress on grain size is still not well understood below this critical grain size. Modelling approaches are called for to fully understand deformation mechanisms in materials across different length scales.

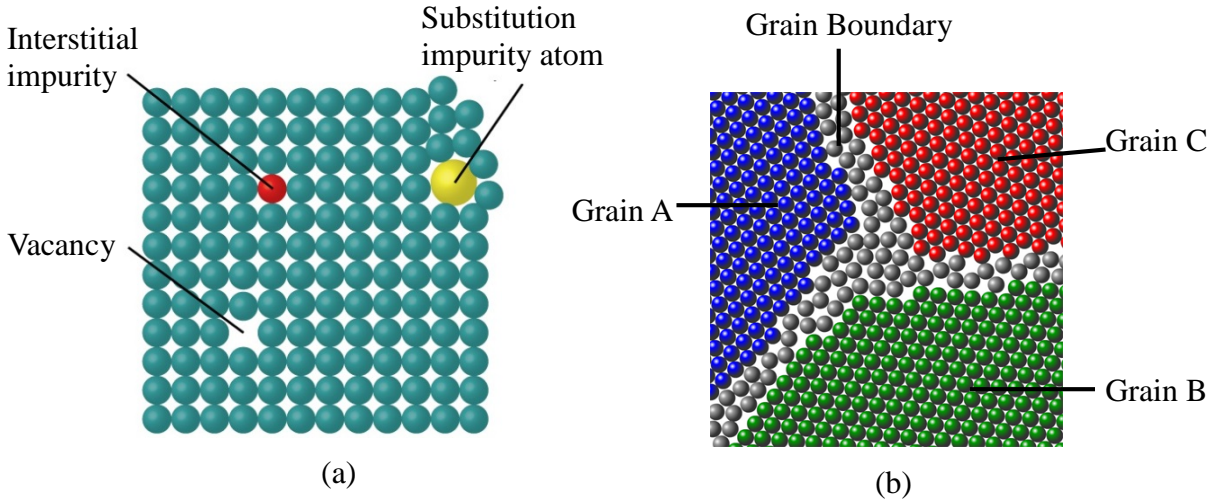


Figure 1.1: Schematic illustration of point defect (a) and grain boundary (b)

Traditional single scale approaches such as molecular dynamics (MD) and continuum mechanics have proven to be inadequate for modeling material deformations across multiple length scales. On the one hand, atomistic simulation is limited by the size of the model simulated [5-7]. The largest atomistic simulations performed with one of the fastest supercomputers in the world are on the order of 10^{13} atoms in 2015. However, there are around 10^{20} atoms in a metal cube with side length of 1 millimeter (mm). On the other hand, continuum mechanics techniques are developed for macroscale problems by describing the macroscale material behavior with empirical constitutive relationships whose parameters are obtained from macroscale experiments. The constitutive relationships require that variables such as temperature, displacement, and stress can be defined by an averaging process and that these variables are assumed to be smoothly varying continuous functions of position. Hence they represent the collective behavior of atoms, and thus continuum mechanics cannot accurately capture the deformation of discrete atoms. The mechanical deformation and failure of many

engineering materials are characterized at multiple scales and the observed macroscopic behavior is governed by physics that occur on many different scales. Since atomistic simulations have the size limitation of scaling up to macroscale systems and continuum mechanics cannot accurately scale down to the atomistic description, a novel approach that combines the best of these two approaches to simulate the behavior of materials at scales ranging from atomistic to macroscopic scales motivates the development of multiscale methods.

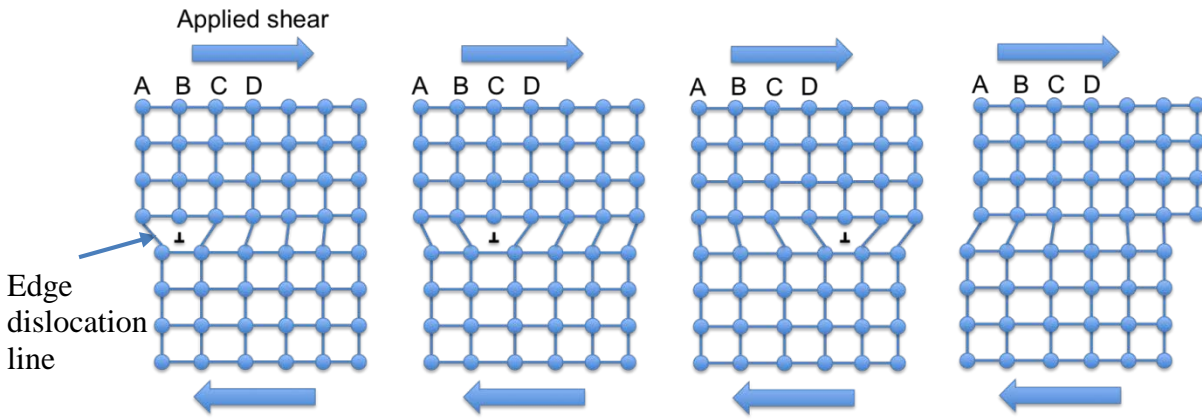


Figure 1.2: Schematic of edge dislocation migration due to applied shear force

1.1 EXISTING MULTISCALE APPROACHES

Many multiscale methods have been developed to bridge different spatial and time scales from Angstroms and femtoseconds to meters and seconds [8-50]. Capturing interaction of different scales is of main concern in multiscale modeling. Sequential or hierarchical multiscale models perform the simulations with step-by-step fashion in a bottom-up approach [17, 51, 52]. The simulations are performed independently of each other at each scale, and a complete separation

of both length and time scales is achieved. Iterative parameter passing between different length scale simulations are employed in sequential methods, which is best suited for coupling scales with weak dependences [52] where a clear separation of scales can be assumed. Concurrent multiscale methods employ the domain decomposition strategy and couple the atomistic region and continuum domain simultaneously [53]. The continually information exchange from one scale to another is to ensure consistency of field variables between the subdomains.

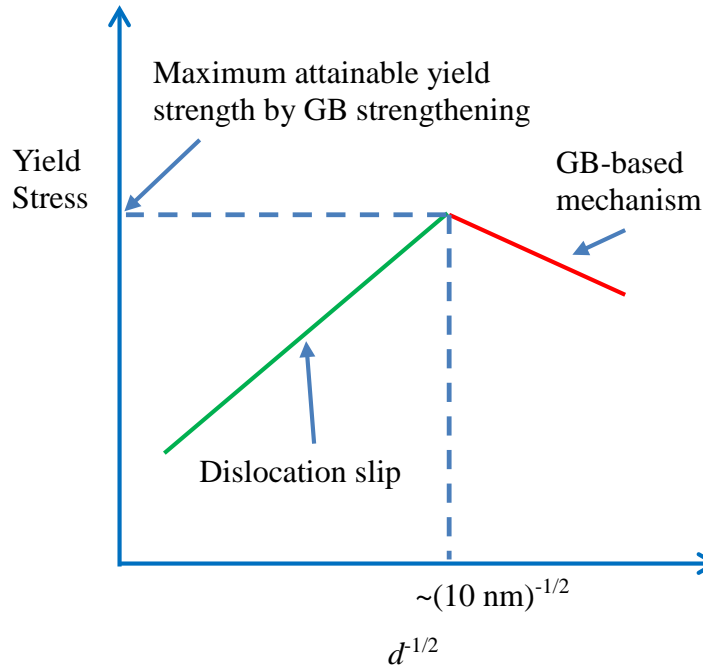


Figure 1.3: Hall-Petch Strengthening is constrained by the size of dislocations. Once the grain size d reaches around 10 nanometers, GB-based mechanism occurs to decrease the yield stress.

Most concurrent coupling schemes employ a region where information passing between atomistic region and continuum domain is achieved. This region is usually referred to as the transition region or ‘handshake region’. It is in this region that requires special treatment due to

the inherent incompatibility of the two subdomains: the non-local interaction of atomistics such as molecular mechanics (MM) and the local interaction of continuum mechanics such as finite element method (FEM). And various concurrent multiscale methods differ in the ways the approximations are made in the transition region [53, 54].

In general, concurrent methods can be further classified into (i) energy-based and (ii) force-based schemes. Energy-based schemes generally have a well-defined energy functional consisting of energy contributions from each subdomain to minimize to derive the force equilibrium equations analytically. This category includes the bridging domain method (BDM) [15, 21], the bridging scale method (BSM) [16, 23, 24, 27], the atomic-scale finite element method (AFEM) [18], the coupling of length scale method (CLS) [12], the local quasicontinuum (QC) method [9] and its energy-based variants [34, 37, 41, 44, 55-60] and the newly presented multiresolution molecular mechanics (MMM) [43, 45, 61], to name a few. Force-based approaches, in contrast, generally derive the force equilibrium equations directly on carefully chosen set of degrees of freedom without minimizing a corresponding energy functional. Among the force-based coupling schemes are the coupled atomistic and discrete dislocations (CADD) [14, 20], the atomic-to-continuum method (Atc) [28, 29], the finite element-atomistic method (FEAt) [8], the force-based variants of the quasicontinuum method [13, 46, 62], and the recently proposed atom collocation method (ACM) [40], just to name a few. As pointed out by R. E. Miller and E.B. Tadmor in [53], the disadvantage of the energy-based method is that the non-physical side effects of the combined energy functional, usually termed “ghost force”, is extremely difficult to eliminate. On the other hand, the drawbacks of the force-based approach are that it can be slow to equilibrate, can converge to unstable equilibrium states, are non-

conservative, and can be unstable numerically. Several excellent review papers [51-54, 63-65] address the details of various multiscale models and the existing challenging issues.

The constitutive description employed in the coarse-grained region plays a key role of determining the performance of a specific multiscale model since it directly relates to the treatment of interface between subdomains and thus to the information exchange. One popular approach to build up the constitutive model is the well-known Cauchy-Born (CB) rule, as first employed in the local QC approach [9]. However, there are two main disadvantages: (I) in nature, CB rule is a local continuum constitutive description that is incompatible with the non-locality of atomic interaction; thus it causes the local-nonlocal mismatch at the interface [54]; (II) CB rule requires sufficiently homogeneous deformation of the underlying crystal and is no longer valid (and thus inaccurate) if the deformation becomes inhomogeneous [66]. The local-nonlocal mismatch causes the so-called “ghost” force problem and has motivated the development of many ghost force correction techniques and the force-based multiscale models [53]. The inaccurate description of nonhomogeneous deformation has motivated the development of high-order CB rules [67-69].

On the other hand, the direct employment of the atomistic constitutive description or the interatomic potential in the coarse-grained region can avoid the aforementioned drawbacks of the CB rule [13, 34-37, 40, 41, 43-45]. Since the constitutive relationships employed in the atomistic and coarse-grained domains are the same, the interface mismatch does not exist. And since the atomic constitutive description has no requirement of the deformation smoothness of underlying crystal, the second disadvantage mentioned above is circumvented. In addition, the direct employment of atomic constitutive description in the coarse-grained region can also help capture

surface size on mechanical properties of nanosized structures, which is an important topic in the field of multiscale modeling.

1.2 SURFACE EFFECT ON NANOSIZED STRUCTURES

Materials with decreased size and dimensionality such as nanowires, nanotubes, nanofilms and nanoparticles may present exceptional properties, i.e., optical, mechanical, electrical and thermal, compared to those of the corresponding macroscopic materials. These size-dependent material properties have been experimentally viewed in [70-77] and computationally observed in [78-83]. For example, by *In situ* tensile testing, Young's modulus, yield strength and ultimate tensile strength are found to increase as the diameter of silver nanowire decreases [76]. Through large-scale atomistic simulations, the tensile yield strength increase and compressive yield strength decrease are observed by decreasing the diameter of metallic glass samples [80]

Nanotechnologies such as nanoscale resonant sensors, micro- and nano-electro-mechanical systems (M/NEMS), and stretchable nano-electronics, can be improved by a better understanding of size-dependent mechanical properties of nanostructures [84]. Applications range from mass and force detection [85-87], frequency synthesis [88, 89] to mechanical switches [90], etc.

The key factor in which nanostructures are different from their macroscopic counterpart lies in that the increasing surface-to-volume ratio at nanoscale is significantly larger than that at macroscopic scale. The presence of abundant free surfaces at nanoscale alters the effective material behavior in both the elastic region and beyond. In particular, surface relaxation changes the local atomic configuration close to the surface due to the lack of bonding neighbors, which in

turn alter the atomic interactions and thus affect the effective elastic moduli. Since the percentage of surface atoms increases with the increasing surface-to-volume ratio that characterizes nanomaterials, the surface effects become significant with decreasing material dimensionality.

The challenge in modelling surface effects for nanosized structures is that on the one hand, continuum hypothesizes that represent bulk material behavior cannot be applied directly but have to be modified to incorporate surface effects; on the other hand, traditional molecular mechanics is limited by the model size due to the demanding computational costs. A wide range of existing approaches have been proposed to solve this challenge. In general, existing models may be classified into three groups: (I) enhanced classical continuum mechanics [78, 91-99], (II) atomic-based continuum analysis [100-104] and (III) coarse-grained atomistic approaches [13, 34, 56, 105, 106].

Some of the works based on enhanced classical continuum model depend on further development of the surface elasticity formulation proposed by Gurtin and Murdoch [107]. In the theory of surface elasticity, a surface is normally considered as a two-dimensionally (2D) heterogeneous thin film bonded perfectly to the bulk material such that their displacements are continuous across the interface. The general idea is to introduce a surface stress tensor to augment the bulk stress tensor typically employed in continuum mechanics. As such, the conventional boundary conditions need to be modified to account for the presence of surface stresses. One major shortcoming of these models is that surface stress components perpendicular to or out-of-surface plane may not be able to be captured due to the equilibrium required between bulk and surface [108].

This has motivated the development of atomic-based continuum analysis. The well-known surface Cauchy-Born (SCB) theory proposed by Park in [100-102, 108, 109] is a representative in this category. The boundary Cauchy-Born (BCB) model is similar to SCB except that BCB also considers corner and edge effects [103, 104, 110, 111]. The main difference of models in group II from approaches in category I lies in that the derivation of the constitutive description in group II is from an underlying atomic structure and interatomic potential, rather than empirical rules and phenomenological models as employed in group I. The key feature of SCB to capture surface effects is based on decomposing the potential energy into bulk and surface components to naturally form a variational framework work that can be directly incorporated into standard nonlinear finite element analysis. Recently thermal effect was considered into SCB based on employing temperature-dependent interatomic potentials [112]. However, SCB cannot be directly applied to model surface-defect interaction due to that SCB is a continuum based on framework in nature, which makes it not universally applicable.

This aforementioned drawback calls for a powerful multiscale model that may not depend on continuum framework such as constitutive stress-strain relationship but pure atomistic description, which motivated the development of coarse-grained atomistic models [13, 34, 37, 44, 56, 57, 59, 61, 106, 113, 114] in group III. The nonlocal QC method [13, 34, 37, 44, 56, 57, 59] is a typical representative and has been recently applied to study surface effect in nanoscale structures based on newly proposed summation rules in [56]. A more detailed discussion on models regarding size-dependent mechanical properties can be found in several review papers [115-117].

1.3 RESEARCH OBJECTIVE AND OUTLINE

1.3.1 Research objective

The main challenging issue arises when using the atomic constitutive description in the coarse-grained region is that an accurate summation rule is needed to approximate the energy contribution from the coarse-grained domain, as shown in Figure 1.4 (the meaning of different symbols will be explained in Section 2.1). In general, the employed summation rule has to answer three questions: the optimal number, position and weight of each quadrature type (sampling) atom. The main merit of employing CB rule in the coarse-grained area is that the energy calculation can be put into the continuum framework that is rather mature and convenient to accurately estimate the energy contribution using quadrature rules. To overcome this challenging issue with employing the atomic constitutive description, Ortiz first proposed the node-based summation rule [13]. However, it caused rank-deficiency and instability problem, and the cluster-based summation rule was developed to overcome the drawbacks of node-based summation rule within the framework of the nonlocal QC method [13]. Luskin and Ortner performed the mathematical error analysis of the cluster summation rule [13, 34] and pointed out that even for the case of nearest neighbor interaction, the cluster-based summation rule may cause large errors in energy that is independent of cluster size when used with graded meshes [118]. This drawback has motivated the development of quadrature-type summation rule by Gunzburgh [35, 36] and the summation rules employed in the nonlocal QC variants [37, 41, 43-45, 61] .

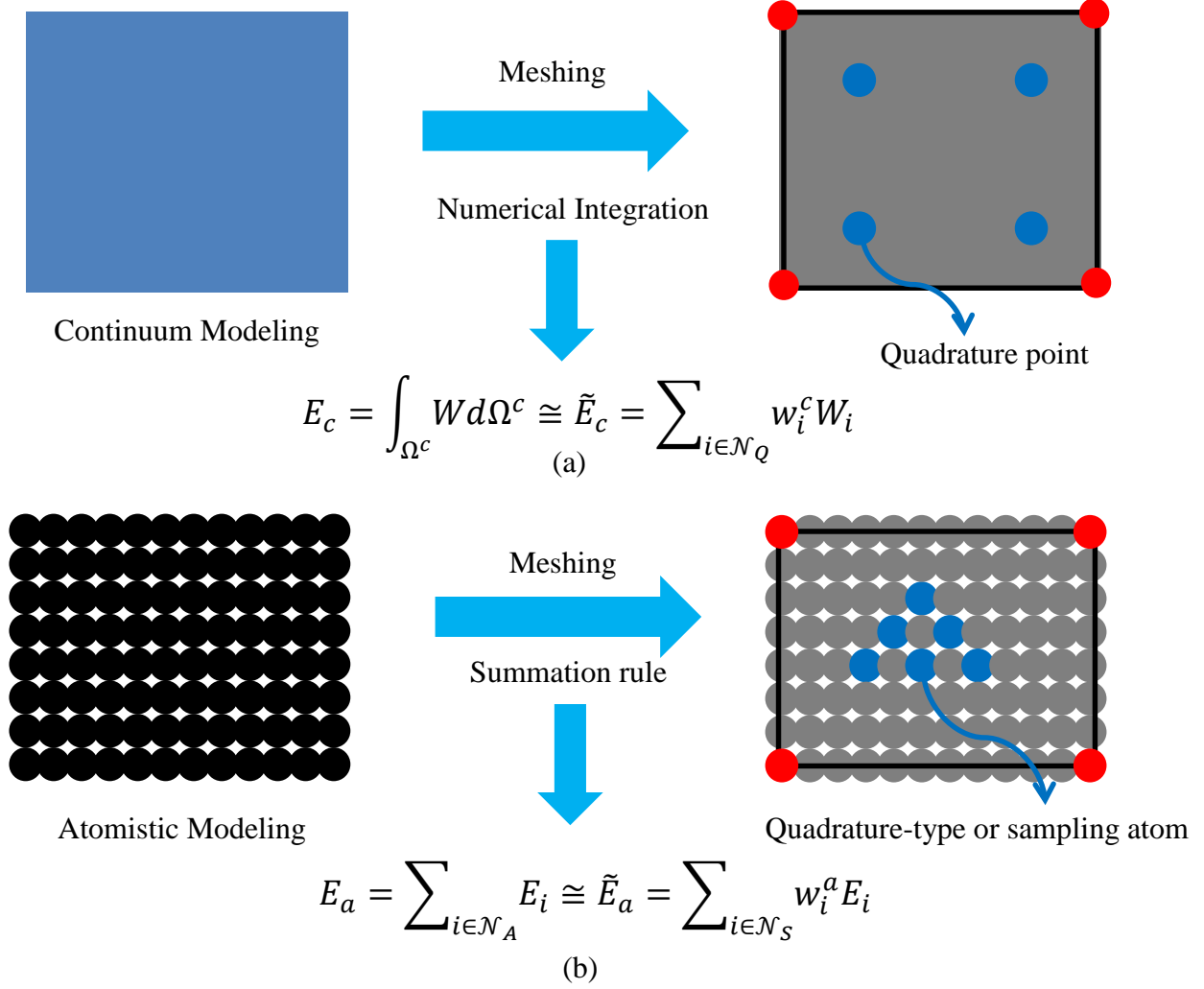


Figure 1.4: Schematically Overview of the MMM methodology in analogy to Finite Element Method (FEM): FEM for continuum modeling (a) and MMM for discrete modeling (b). The meaning of different symbols will be explained in Section 2.1.

Since the proposed summation rules employed in nonlocal QC framework are specifically designed for linear interpolation shape functions, the consistent extension to high order interpolation shape functions is not clear, as has been clearly observed in [58, 60]. Since linear shape function is not well suitable for deformations such as bending and bending

experiments are widely employed to identify the size-dependent mechanical properties of nanosized materials, there is a need to develop a coarse-grained atomistic framework that is universally applicable to generally types of interpolation shape functions and deformations.

The primary research objective of this dissertation is to establish a new coarse-grained atomistic framework, named Multiresolution Molecular Mechanics (MMM) by designing a new summation rule SR^{MMM} to mathematically determine the optimal number, position and weight of each quadrature-type (sampling) atom for linear to any high order interpolation shape function, analogous to Gauss quadrature that is widely employed in conventional finite element method (FEM). In addition, the proposed SR^{MMM} has the ability to naturally and accurately capture surface effects. We point out that though SR^{MMM} has similarity with the proposed summation rules in [37, 41, 56, 57] with respect to linear interpolation shape function, SR^{MMM} is fundamentally different from others in that it can be consistently derived for any order of shape function, as will be shown later. Mathematically, the main advantages of SR^{MMM} are: (1) it is derived consistently with any interpolation shape function employed; (2) it provides a theoretical foundation to analyze and design different summation rules. It is worth to note that though spatial and temporal coarse-graining are equally important, the present work will focus on coarse-graining in space for statics. Techniques employed to coarse-grain temporal scale at finite temperatures in [42, 119-121] may be applied to the present work.

1.3.2 Outline

This dissertation is organized as follows. Analogous to finite element method in continuum mechanics, the theory and framework of MMM is given in details in Chapter 2.0 . The proposed summation rule SR^{MMM} is based on mathematically deriving the order or distribution of finite

energy summations involved in coarse-grained atomistic model and then reproduces this distribution accurately to determine the number, position and weight for each quadrature-type (sampling) atom. SR^{MMM} is then consistently decomposed into the bulk summation rule SR^B and surface summation rule SR^S . This decomposition lies in the observation that the derived energy distribution of surface area is different from that of bulk region. Physically, the difference is caused by the fact that surface atoms are lack of neighboring bonding. As such, SR^S and SR^B are employed for surface and bulk domains, respectively. 1D quadratic, 2D bilinear and 3D hexahedral finite elements are employed as representative interpolation shape functions on how to derive SR^{MMM} in detail.

In Chapter 3.0 , we first identify two different error sources (discretization error and sampling error) and then define errors norms in displacement and energy fields, as inspired by the corresponding counterparts in classical FEM, in order to quantify the performance of MMM. The defined norms are employed to verify and validate the bulk summation rule SR^B with respect to linear, bilinear and quadratic elements in 1D and 2D. SR^B is also compared against different summation rules such as Gauss-quadrature-like rule. It is observed that SR^B outperforms other summation rules employed. The interface compatibility of MMM and several existing approaches are also compared against each other by employing a benchmark test. In addition, MMM has been applied to problems such as high-order tensile, shear and bending deformations. The ability of MMM to capture crack propagation is also demonstrated.

Chapter 4.0 specifically focuses on applying MMM to capture surface effect by the employment of the surface summation rule SR^S . Numerical examples using the respective 4-node quadrilateral and 8-node hexahedral meshes are employed to solve surface relaxation problems in 2D and 3D. It is shown that MMM with SR^{MMM} (SR^S+SR^B) can accurately capture corner,

edge and surface effects, compared against full atomistic (FA) simulation. The accuracy of FA simulation can be reasonably reproduced by employing MMM with 0.3% less in the number of degrees of freedom of the original atomistic system.

Chapter 5.0 numerically studies the convergence property and error structure of MMM for linear interpolation shape by employing relatively comprehensive numerical examples. Four different sampling schemes within the framework of SR^{MMM} are defined and studied. The convergence analysis is performed by reducing the size of a uniform mesh by half at each time, as in convention FEM. The effects of the regularity and smoothness of the exact solution and the nonlinearity of interatomic potential on the convergence behavior of MMM are considered. The error structure analysis is performed by numerically analyzing how the discretization error and sampling error behave at different element sizes. It is observed that MMM demonstrates FEM-like convergence behavior under certain circumstance.

Chapter 6.0 summarizes the dissertation with the main contributions and proposes future works with discussions in several directions such as iso-parametric and adaptive analysis, temporal scale acceleration and parallel implementation.

2.0 MULTIREOLUTION MOLECULAR MECHANICS

In this chapter, analogous to the well-known finite element method (FEM) in conventional continuum mechanics, the general framework of Multiresolution Molecular Mechanics (MMM) is presented with the introduction of the proposed novel summation rule SR^{MMM} for general interpolation shape functions. Several examples on how to derive the specific form of SR^{MMM} are given in detail with respect to 1D, 2D and 3D interpolation shape functions. Much of this section is from recent work in [40, 43, 45, 61, 113].

2.1 OVERVIEW

In Figure 1.4a, a finite element with shape function ϕ is introduced to approximate the original continuum model and the potential energy E_c can be approximated as:

$$E_c = \int_{\Omega^c} W d\Omega^c \cong \tilde{E}_c = \sum_{i \in \mathcal{N}_Q} w_i^c W_i \quad (2.1)$$

where W is potential energy density, Ω^c denotes the continuum domain, \mathcal{N}_Q represents the index set of N_Q quadrature points and w_i^c is the associated weight for a quadrature point $i \in \mathcal{N}_Q$. In the present work, calligraphic letter \mathcal{N} represents index set and the corresponding Roman letter N defines its cardinality.

In general, Gauss quadrature is widely employed to evaluate the energy integral in Eq.(2.1) and there is a standard way to determine the optimal number of quadrature points needed, the position and weight for each employed quadrature point. Similarly, in Figure 1.4b, a finite element is also employed to reduce the degrees of freedom of the original atomistic model and the potential energy E_a is approximated as:

$$E_a = \sum_{i \in \mathcal{N}_A} E_i \cong \tilde{E}_a = \sum_{i \in \mathcal{N}_S} w_i^a E_i \quad (2.2)$$

where \mathcal{N}_A is the index set of the N_A atoms in the original atomistic model, E_i is the atomic site energy of an atom $i \in \mathcal{N}_A$, \mathcal{N}_S denotes the index set of the chosen N_S sampling or quadrature-type atoms and w_i^a is the associated weight for a sampling atom $i \in \mathcal{N}_S$. The red dots in Figure 1.4 are either the conventional finite element nodes for continuum mechanics or the representative atoms (rep-atoms) or nodal atoms for atomistic modeling. And the blue dots represent either a quadrature point to evaluate an integral or a sampling atom to calculate a finite summation. Since the energy of gray atoms in Figure 1.4b is not considered explicitly but sampled by the energy of blue dots (sampling atoms), as the gray area in Figure 1.4a, we call these gray atoms non-sampling atoms (NSAs).

As conventional finite element nodes and nodal atoms play similar roles in their respective modeling method, we do not differentiate the coloring approach between coarse-grained continuum and atomistic model, so is the same for quadrature and quadrature-type dots. This coloring scheme will be consistently employed in this work if not otherwise mentioned. We note that if a quadrature point coincides with a finite element node, as it may occur for high order elements, we will clearly point it out. In addition, any symbol with a subscript or superscript “ c ” employed for continuum model has the same physical meaning as the same symbol with a subscript or superscript “ a ” utilized for atomistic system.

The key problem in Eq. (2.2) is to develop a standard and systematic theory to determine the optimal number N_s , weight w_i^a and position for each sampling atom for general finite element shape functions, as Gauss quadrature in continuum mechanics.

2.2 MMM SUMMATION RULE SR^{MMM}

In conventional FEM, it is well-known that the order of employed quadrature rule is shape-function dependent [122]. In the following derivation, we will show that the order of employed SR^{MMM} also depends on shape functions, which is different from the summation rule proposed in [57] where it is mentioned that the calculation of weight w_i^a is independent of employed interpolation scheme.

For simplicity, external loads are not considered and linear elasticity model is assumed for continuum mechanics. Then the potential energy approximation \tilde{E}_c in Eq. (2.1) can be expressed in the form of Eq. (2.3) as:

$$\tilde{E}_c = \frac{1}{2} \sum_{i \in \mathcal{N}_n^c} \sum_{j \in \mathcal{N}_n^c} \mathbf{u}_i^c{}^T \mathbf{K}_{ij}^c \mathbf{u}_j^c \quad (2.3)$$

where \mathcal{N}_n^c is the index set of N_n^c finite element nodes, \mathbf{u}_i^c is the nodal displacement vector for a node $i \in \mathcal{N}_n^c$ and \mathbf{K}_{ij}^c represents the nodal stiffness matrix for nodes i and j . \mathbf{K}_{ij}^c can be formulated as:

$$\mathbf{K}_{ij}^c = \int_{\Omega^c} \mathbf{B}_i^T \mathbf{D}^c \mathbf{B}_j d\Omega^c \quad (2.4)$$

where \mathbf{D}^c is a matrix of material constants that describes the continuum constitutive behavior, \mathbf{B}_i is the strain matrix for node i and can be defined in 3D as:

$$B_i = \begin{bmatrix} \phi_{i,x} & 0 & 0 \\ 0 & \phi_{i,y} & 0 \\ 0 & 0 & \phi_{i,z} \\ \phi_{i,y} & \phi_{i,x} & 0 \\ 0 & \phi_{i,z} & \phi_{i,y} \\ \phi_{i,z} & 0 & \phi_{i,x} \end{bmatrix} \quad (2.5)$$

From Eq. (2.5) we note that the order of employed quadrature rule to evaluate \tilde{E}_c or K_{ij}^c depends on the product order of two shape function derivatives. In particular, let Π_{ij}^c denote the product of shape functions derivatives in 1D, as follows:

$$\Pi_{ij}^c = \phi_{i,x} \phi_{j,x} \quad (2.6)$$

From Eqs. (2.3)-(2.6), we point out that the distribution of \tilde{E}_c is determined by the order of function bases in Π_{ij}^a . As an example, let ϕ be the one-dimensional quadratic shape function. Then, by a simple calculation, one can see that the solid line in Figure 2.1a that describes the distribution of \tilde{E}_c can be defined as:

$$f^c(x_c) = b_c^0 + b_c^1 x_c + b_c^2 x_c^2 \quad (2.7)$$

where b_c^i , $i = 0-2$ are constants in terms of nodal displace vector $\mathbf{u}_i^c, i \in \mathcal{N}_n^c$ and material constants in matrix D, x_c is a material point position that continuously spans continuum domain Ω^c . Then \tilde{E}_c can be evaluated as:

$$\tilde{E}_c = \int_{\Omega^c} f^c(x_c) d\Omega^c \quad (2.8)$$

Since $f^c(x_c)$ is a continuous quadratic function, then the optimal number of quadrature point N_Q is 2 and their corresponding weight w_i^c in Eq. (2.1) can be determined by Gauss quadrature rule, which shows how the employed shape function derivatives determine the order of selected quadrature rule in conventional FEM. Next, we will show how SR^{MMM} is derived and related to a given shape function differences.

Similarly, for an atomistic model, a nonlocal linear spring potential is assumed for interatomic interaction to ease the demonstration of the general picture in SR^{MMM}. Then the potential energy approximation \tilde{E}_α in Eq. (2.2) can be expressed as:

$$\tilde{E}_\alpha = \frac{1}{2} \sum_{i \in \mathcal{N}_\alpha^a} \sum_{j \in \mathcal{N}_\alpha^a} \mathbf{u}_i^{aT} \mathbf{K}_{ij}^a \mathbf{u}_j^a \quad (2.9)$$

where \mathbf{K}_{ij}^a is defined as:

$$\mathbf{K}_{ij}^a = \frac{1}{2} \sum_{\alpha \in \mathcal{N}_A} \sum_{\beta \in \mathcal{N}_\alpha} \mathbf{B}_i^{aT} \mathbf{D}^a \mathbf{B}_j^a \quad (2.10)$$

$$\mathbf{B}_i^a = [\phi_i(\mathbf{r}_{\alpha 0}) - \phi_i(\mathbf{r}_{\beta 0})] \mathbf{I} \quad (2.11)$$

where \mathcal{N}_α is the index set of N_α atoms that interacts with atom $\alpha \in \mathcal{N}_A$, $\mathbf{r}_{\alpha 0}$ denotes the initial position vector of atom α and \mathbf{D}^a is the material constants or the local stiffness matrix that describes the interatomic interaction in each direction. For linear spring potentials in 3D, \mathbf{I} is 3 by 3 identity matrix. Note that \mathbf{B}_i^a is different from \mathbf{B}_i^c since there is no shape function directive involved and we do not have shear strain in the interatomic potential. Physically, this difference is due to the fact that the constitutive relationship in continuum mechanics generally contains six strains; however, the interatomic potential in atomistic modeling depends on pair distance difference in x , y and z directions.

For lattice or crystal structures, $\mathbf{r}_{\beta 0}$ can be determined in terms of $\mathbf{r}_{\alpha 0}$, as follows:

$$\mathbf{r}_{\beta 0} = \mathbf{r}_{\alpha 0} + \mathbf{C}(a_0) \quad (2.12)$$

where \mathbf{C} is a non-zero constant vector in terms of the lattice constant a_0 . If Eq. (2.12) is plugged back into Eq. (2.10), we note that the evaluation of \mathbf{K}_{ij}^a is determined by the product of employed shape function difference calculated at an atom $\alpha \in \mathcal{N}_A$. For example, let ϕ be the one-dimensional quadratic shape function. Then \mathbf{I} is 1 and \mathbf{D}^a is the pair-wise spring constant. Let Π_{ij}^a denote the shape function difference product as follows:

$$\Pi_{ij}^a = [\phi_i(\mathbf{r}_{\alpha 0}) - \phi_i(\mathbf{r}_{\alpha 0} + \mathbf{C}(a_0))][\phi_j(\mathbf{r}_{\alpha 0}) - \phi_j(\mathbf{r}_{\alpha 0} + \mathbf{C}(a_0))] \quad (2.13)$$

By a simple calculation, one can see that Π_{ij}^a is also quadratic in terms of components of $\mathbf{r}_{\alpha 0}$. Then, from Eqs. (2.9)-(2.13), we note that the dashed line in Figure 2.1b that describes the distribution of \tilde{E}_a can also be defined as:

$$f^a(x_a) = b_a^0 + b_a^1 x_a + b_a^2 x_a^2 \quad (2.14)$$

where b_a^i , $i = 0-2$ are constants in terms of nodal displace vector $\mathbf{u}_i^a, i \in \mathcal{N}_n^a$ and material constants in the employed linear spring potential, x_a is an atomic position that discretely spans atomic domain Ω^a . Then \tilde{E}_a can be evaluated as:

$$\tilde{E}_a = \sum_{i \in \mathcal{N}_A} f^a(x_a^i) \quad (2.15)$$

where x_a^i is the atomic position of an atom $i \in \mathcal{N}_A$. We note that the difference between the energy of a surface atom and that of a bulk atom is not distinguished so far for the sake of simplifying the general idea of SR^{MM}. From Figure 2.1, one can see that the similarity between \tilde{E}_c and \tilde{E}_a lies in that they have the same distribution order. The main difference between them is that $f^c(x_c)$ is a continuous function (solid line) in terms of x_c but $f^a(x_a)$ is a set of discrete points in terms of x_a that pass through the dashed line. As such, three sampling or quadrature-type atoms are required to exactly represent the dashed energy distribution line. Then the optimal number for sampling atoms N_s is 3 and the corresponding weight w_i^a in Eq. (2.2) can be determined as in any curve-fitting process. For example, as the dashed line in Figure 2.1b has a quadratic form, three sampling atoms (2 blue dots and the interior red node) are selected. Then the dashed line can be expressed as:

$$f^a(x_a) = \sum_{i \in \mathcal{N}_S} \Phi_i(x_a) E_i \quad (2.16)$$

where Φ_i is defined as:

$$\Phi_i = \prod_{i \neq j, i \in \mathcal{N}_S, j \in \mathcal{N}_S} \frac{x_a - x_a^j}{x_a^i - x_a^j} \quad (2.17)$$

As can be seen from Eq. (2.17), Φ_i satisfies partition of unity and the Kronecker delta property, as follows:

$$\sum_{i \in \mathcal{N}_S} \Phi_i(x_a^k) = 1, \forall k \in \mathcal{N}_A \quad (2.18)$$

$$\Phi_i(x_a^j) = \delta_{ij}, \forall i, j \in \mathcal{N}_S \quad (2.19)$$

Then the energy summation \tilde{E}_a in Eq. (2.15) at the discrete atoms is calculated as:

$$\tilde{E}_a = \sum_{j \in \mathcal{N}_A} f(x_a^j) = \sum_{j \in \mathcal{N}_A} \sum_{i \in \mathcal{N}_S} \Phi_i(x_a^j) E_i = \sum_{i \in \mathcal{N}_S} \sum_{j \in \mathcal{N}_A} \Phi_i(x_a^j) E_i \quad (2.20)$$

Comparing Eqs. (2.20) and (2.2), we note that:

$$w_i^a = \sum_{j \in \mathcal{N}_A} \Phi_i(x_a^j) \quad (2.21)$$

The above curve-fitting-like process to determine the optimal number of sampling atoms N_S and the corresponding weight w_i^a forms the MMM summation rule SR^{MMM} , which clearly shows how SR^{MMM} is related to the employed shape function differences.

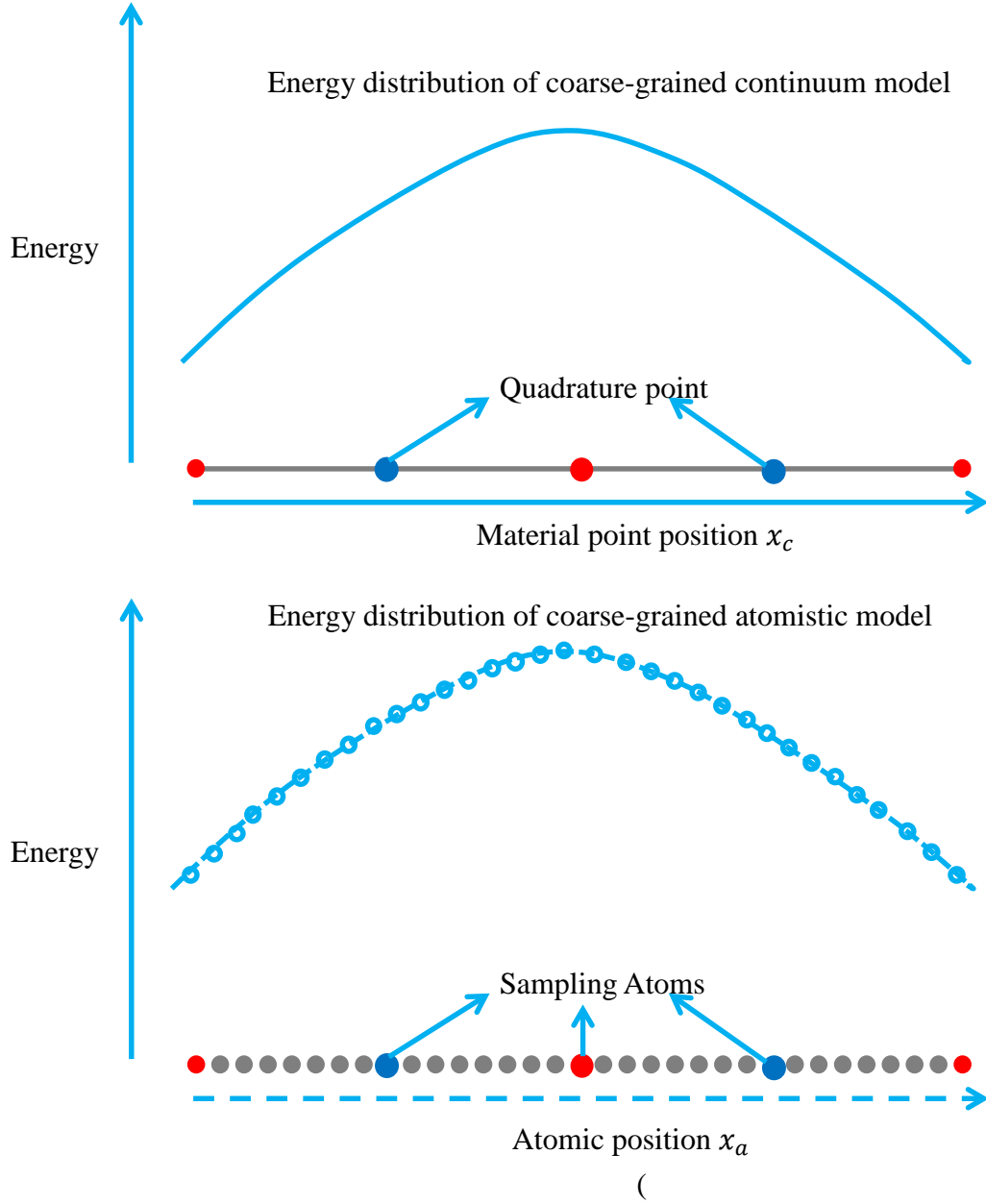


Figure 2.1: Schematically illustration of energy distributions for coarse-grained continuum model (a) and coarse-grained atomistic model (b). Solid line denotes a continuous curve and dashed line a curve passing through discrete energy point for each atom. The solid x axis means x_c continuously spans the continuum domain (a) and the dashed x axis represents that x_a discretely spans the space (b).

2.3 SR^{MMM} DECOMPOSITION SR^B AND SR^S

2.3.1 Why the decomposition is needed

In this sub-section, we will explain why there is a need to distinguish the difference between the energy of a surface atom and that of a bulk atom and as such to decompose SR^{MMM} into the bulk summation rule SR^B and the surface summation rule SR^S.

We note that \mathcal{N}_α in Eq. (2.10) is the index set of N_α neighboring atoms that interacts with an atom $\alpha \in \mathcal{N}_A$. Physically, the fundamental difference between surface atoms and bulk counterpart is that surface atoms are not fully coordinated and are lack of bonding neighbors. As such, N_α^S , the number of neighboring atoms of a surface atom α that belongs the index set of surface atoms \mathcal{N}_A^S , is different from N_α^B , the number of neighboring atoms that interacts with a bulk atom α that resides in the index set of bulk atoms \mathcal{N}_A^B . As a result, the energy distribution of surface atoms, $f_S^a(x_a)$, will be different from that of bulk atoms, $f_B^a(x_a)$, even though they both reserve the quadratic form in Eq. (2.14) for the one-dimensional quadratic shape function considered in Section 2.2. Mathematically, this is because the coefficient b_a^i , $i = 0-2$, in Eq. (2.14) take different values for $f_S^a(x_a)$ and $f_B^a(x_a)$, respectively. This is schematically demonstrated in Figure 2.2 where the energy of surface atoms (empty circles in rectangle boxes) does not follow the bulk energy distribution curve (dashed line).

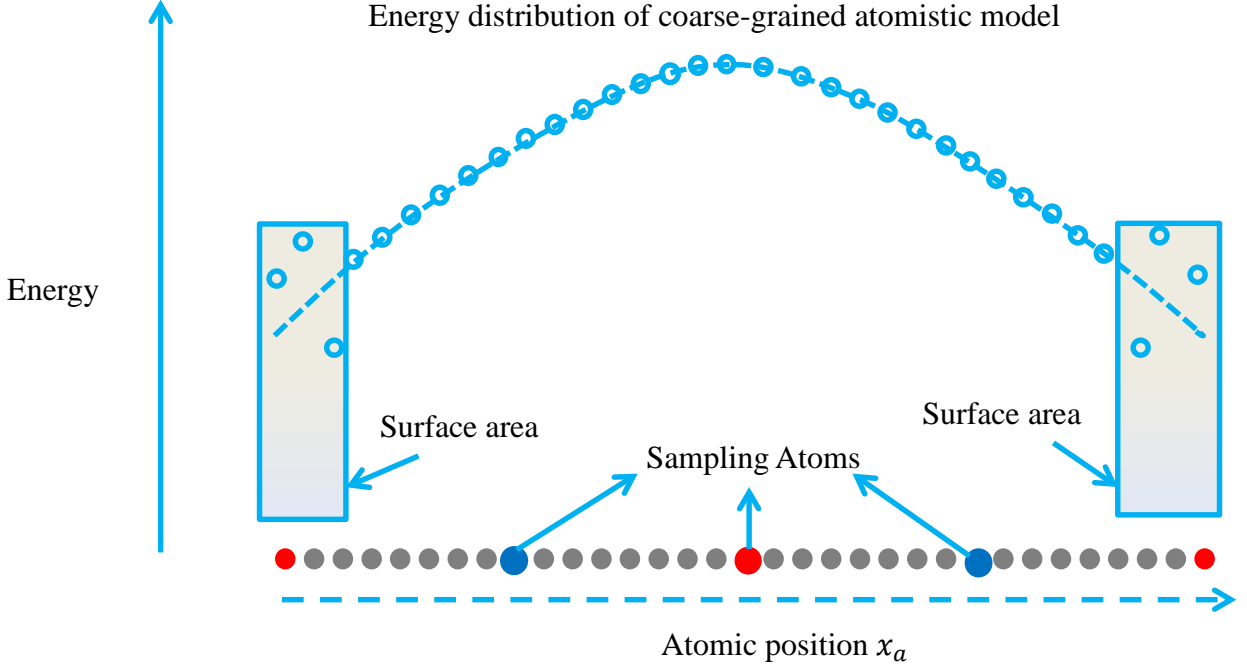


Figure 2.2: Energy distribution for atoms in bulk region and atoms in surface areas.

For the reasons discussed above, SR^{MMM} is decomposed to SR^{B} and SR^{S} . Basically, SR^{B} is employed to treat bulk atoms and SR^{S} is used to treat surface atoms to accurately represent the energy distribution over the whole atomic domain Ω^a . The methodology to determine the optimal number of sampling atom N_s and their respective weights w_i^a in SR^{B} and SR^{S} are exactly the same as how they are determined in SR^{MMM} in Section 2.2.

2.3.2 Examples of employed bulk and surface summation rules

In this sub-section, we will use 4-node quadrilateral and 8-node hexahedral elements as representative examples to demonstrate how to design the bulk and surface summation rules for a certain type of interpolation shape function in 2D and 3D.

From Section 2.2, we know that a key step to derive SR^{MMM} is to determine $f^a(x_a)$ in Eq. (2.14). For the 4-node quadrilateral element in 2D, the shape function ϕ_i for a node $i \in \mathcal{N}_n^a$ takes the following form:

$$\phi_i(x, y) = a_i^0 + a_i^1 x + a_i^2 y + a_i^3 xy \quad (2.22)$$

where x and y are the respective projection of position vector $\mathbf{r} = \begin{pmatrix} x \\ y \end{pmatrix}$ of an arbitrary atom in x and y directions, a_i^α , $\alpha = 0-3$ are constants in terms of the chosen nodal positions to construct ϕ_i . Let C_x and C_y be the projection of the non-zero constant vector $\mathbf{C} = \begin{pmatrix} C_x \\ C_y \end{pmatrix}$ in Eq. (2.12) in x and y directions, respectively. Then $\phi_i(\mathbf{r} + \mathbf{C})$ in Eq. (2.13) is calculated as:

$$\phi_i(x + C_x, y + C_y) = a_i^0 + a_i^1(x + C_x) + a_i^2(y + C_y) + a_i^3(x + C_x)(y + C_y) \quad (2.23)$$

such that the shape function difference is expressed as:

$$\phi_i(x, y) - \phi_i(x + C_x, y + C_y) = b_i^0 + b_i^1 x + b_i^2 y \quad (2.24)$$

where b_i^α , $\alpha = 0-2$ are given in terms of a_i^α , $\alpha = 0-3$ and constants C_x and C_y . Then, Π_{ij}^a in Eq. (2.13) is defined as:

$$\Pi_{ij}^a = c_{ij}^0 + c_{ij}^1 x + c_{ij}^2 y + c_{ij}^3 xy + c_{ij}^4 x^2 + c_{ij}^5 y^2 \quad (2.25)$$

where c_{ij}^α , $\alpha = 0-5$, are constants given in terms of b_i^α and b_j^α , $\alpha = 0-2$. Finally, $f^a(x_a)$ in Eq. (2.14) takes the following form:

$$f^a(x_a) = b_a^0 + b_a^1 x + b_a^2 y + b_a^3 xy + b_a^4 x^2 + b_a^5 y^2 \quad (2.26)$$

where b_a^i , $i = 0-5$ are constants in terms of nodal displace vector $\mathbf{u}_i^a, i \in \mathcal{N}_n^a$ and material constants in the employed linear spring potential and the coefficients in the given bilinear shape function.

From Eq. (2.26), we note that the optimal number of sampling atoms N_S^B for SR^B is 6 and Φ_i in Eq. (2.17) also has a fully quadratic form and can be determined in a curve-fitting-like

process, as discussed in Section 2.2, such that w_i^a is also identified correspondingly in Eq. (2.21).

The derivation of $f^a(x_a)$ for the employed 8-node hexahedral element in 3D follows exactly the same ways as for the 4-node quadrilateral element in 2D. We find that $f^a(x_a)$ reserves a fully quadratic order plus some mixed high order terms for the employed 8-node element in 3D. In this thesis, we will discard the mixed terms and assume $f^a(x_a)$ takes the following form:

$$f^a(x_a) = b_a^0 + b_a^1x + b_a^2y + b_a^3z + b_a^4xy + b_a^5xz + b_a^6yz + b_a^7x^2 + b_a^8y^2 + b_a^9z^2 \quad (2.27)$$

such that N_S^B is 10 and Φ_i and w_i^a can be determined correspondingly, following the above discussed curve-fitting-like process.

So far, the optimal number of sampling atoms N_S^B and their corresponding weight w_i^a in bulk summation rule SR^B are discussed and determined. Next, we will show how N_S^S , the optimal number of sampling atoms in SR^S , and their corresponding weight w_i^a are identified.

For the rectangle triangular lattice in 2D, as shown in Figure 2.3, we note that either x or y is constant for the respective surface edge and non-bulk edges. As such, $f^a(x_a)$ in Eq. (2.26) can be reduced to fewer terms. For instance, for the surface edge on the left hand side, y is constant such that $f_S^a(x_a)$ can be reformed as:

$$f_S^a(x_a) = \varepsilon_a^0 + \varepsilon_a^1x + \varepsilon_a^2x^2 \quad (2.28)$$

where ε_a^i , $i = 0-2$ are constants in terms of b_a^i in Eq. (2.26) and y . Then from Eq. (2.28), it is clearly seen that N_S^S is 3 and w_i^a in SR^S can be calculated as in SR^B . If a non-bulk layer is considered, the same SR^S can also be applied, as in the employed 2D example in Section 4.0 . Figure 2.3 schematically demonstrates the idea about how SR^{MM} ($SR^S + SR^B$) is employed for the four-node quadrilateral element with (Figure 2.3a and Figure 2.3c) and without a corner atom

(Figure 2.3c and Figure 2.3d). In order to distinguish the aforementioned sampling atoms from secondary sampling atoms (*SSAs*) that will be introduced later in this section, we name these sampling atoms primary sampling atoms (*PSAs*) (blue dots in Figure 1.4-Figure 2.3). In addition, the *PSAs* where SR^S is applied are named surface *PSAs* (*SPSAs*) and *PSAs* inside the dashed rectangle where SR^B is applied are called bulk *PSAs* (*BPSAs*).

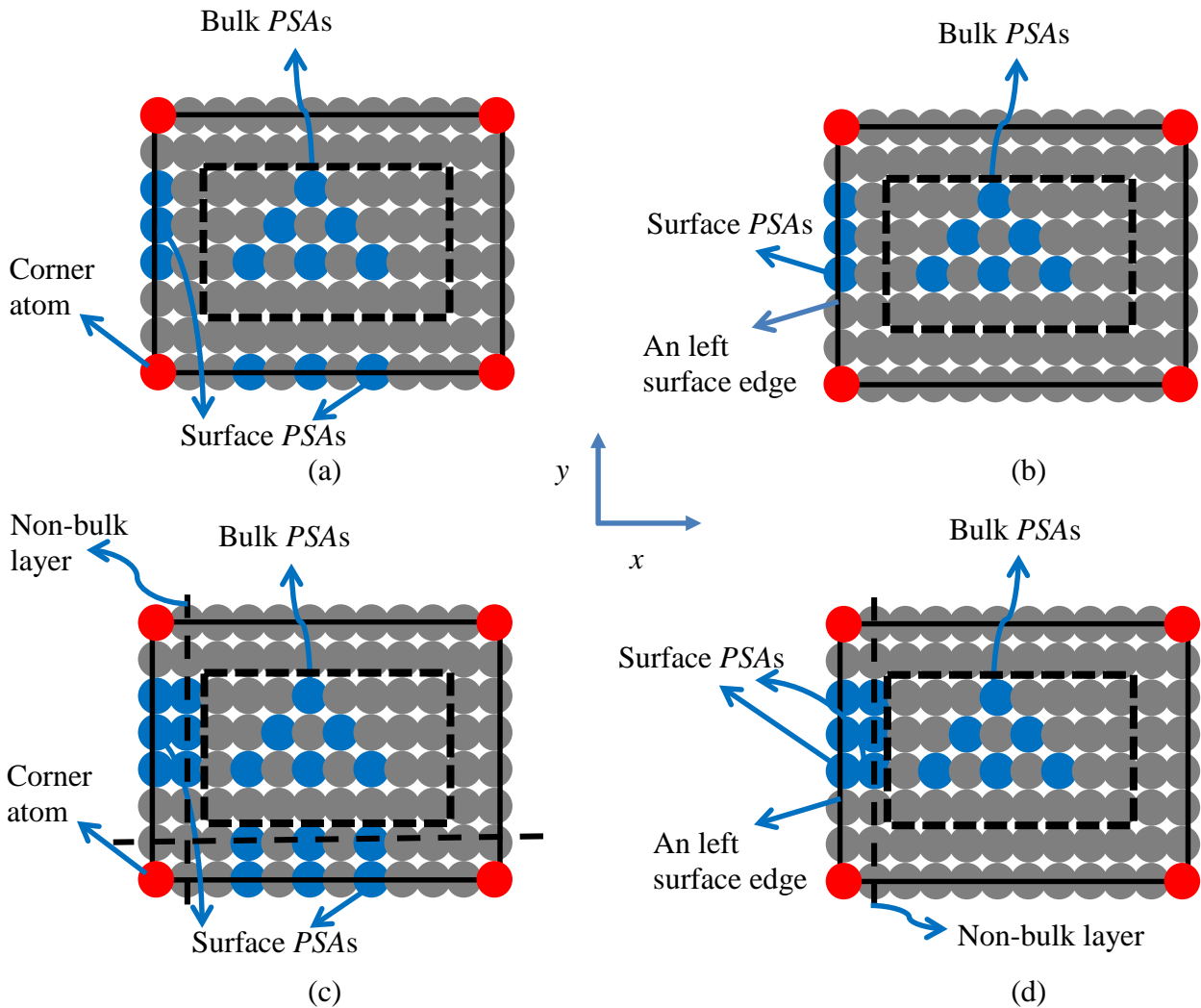


Figure 2.3: Employed SR^{MMM} ($SR^B + SR^S$) in 2D for the selected 4-node quadrilateral element: SR^{MMM} for an element that contains a corner atom (a); SR^{MMM} for an element that contains only

one surface edge (b); SR^{MMM} for an element that contains a corner atom and non-bulk layers (dashed line) (c); SR^{MMM} for an element that contains one surface edge and one non-bulk layer (d). SR^{B} is employed for bulk non-sampling atoms (*NSAs*) and SR^{S} for surface and non-bulk *NSAs*. Dished rectangle denotes the element bulk region.

The same idea can be applied to a face-centered cubic (FCC) lattice in 3D. For each of the surface and non-bulk layers, either x , y or z is constant such that $f^a(x_a)$ in Eq. (2.27) can also be trimmed to fewer terms. For example, for the surface layer on the bottom, z is a constant such that $f_s^a(x_a)$ can be redefined as:

$$f_s^a(x_a) = b_a^0 + b_a^1x + b_a^2y + b_a^3xy + b_a^4x^2 + b_a^5y^2 \quad (2.29)$$

where the summation rule SR^{MMM} in 2D can be directly applied such that N_s^S and w_i^a can be determined accordingly. We note that, mathematically, SR^{S} in 3D is, in fact, the SR^{MMM} ($\text{SR}^{\text{B}} + \text{SR}^{\text{S}}$) in 2D and the SR^{S} in 2D is actually the SR^{MMM} ($\text{SR}^{\text{B}} + \text{SR}^{\text{S}}$) in 1D. This is understandable since, physically, it is obvious that the surfaces of 3D model are 2D and the edges of 2D are 1D. Note that the 2D surface or 1D edge could be curved. In the present work, we focus on regular shapes. Surfaces and edges with curvature will be considered in our future work.

For positions of primary sampling atoms, we note that different selections of primary sampling atoms in SR^{B} (thus called bulk sampling atoms) may not produce a significant difference as long as they are selected from the bulk region such that they are not coplanar. This is understandable from the perspective of curve-fitting process. For instance, a 2D quadratic surface can be represented by 6 selected points provided that they are not coplanar. The same conclusion applies to the selection of surface primary sampling atoms in SR^{S} . Numerical

examples in Chapter 3.0 will discuss more about the *PSAs* selection effect on the performance of SR^{MMM} .

It is worth to note that the energy of corner atoms does not exactly follow $f_S^a(x_a)$ or $f_B^a(x_a)$ for the reason that the neighbors of corner atoms are located on more surfaces than that of surface or bulk atoms. Similarly, the energy of atoms that coincide with N_n^a finite element nodes (called nodal atoms) and energy of atoms near element edges (called element edge atoms) within a potential cut-off distance (r_{cut}) also do not exactly follow $f_S^a(x_a)$ or $f_B^a(x_a)$ due to that neighbors of these atoms are located in more finite elements. As will be shown in Chapter 3.0 , the assumption that the energy of element edge atoms follows $f_S^a(x_a)$ or $f_B^a(x_a)$ may not introduce significant errors. However, the energy of nodal atoms will be considered explicitly instead of being sampled by energy of primary sampling atoms. For this reason, we call the atoms whose energy are considered explicitly secondary sampling atom (*SSA*) to represent their own energies (such that the weight w_i^a is 1 for each *SSA*). A more detailed explanation and atom classification will be discussed in Section 2.5.

2.3.3 Discussion of several summation rules

In this sub-section, the proposed summation rule SR^{MMM} will be qualitatively compared with several proposed summation rules within the Quasicontinuum (QC) method in terms of employed constitutive model, energy distribution and element type in the coarse-grained region (Figure 2.4).

For different summation rules employed in Figure 2.4, two linear elements are utilized in the coarse-grained region to schematically show the idea of each employed summation rule. In the local QC framework [9], the well-known Cauchy-Born (CB) rule is used (Figure 2.4a). The

Cauchy-Born rule is based on the assumption that the underlying atomic unit cell at a quadrature point (blue dots in Figure 2.4a) deforms uniformly according to the deformation gradient \mathbf{F} that is evaluated at the corresponding quadrature point (Figure 2.5). The stored potential energy in the deformed unit cell divided by its volume is then taken as the continuum strain energy density. CB assumption is valid for linear element where deformation gradient \mathbf{F} is constant. And for high order elements, CB rule is inaccurate to evaluate the continuum strain energy since the variation of deformation gradient \mathbf{F} is not captured. In addition, CB framework is, in nature, a continuum-based description such that the employed constitutive relationship in the coarse-grained region is local, which is incompatible with the nonlocal constitutive model in the atomistic domain, as described by the employed interatomic potential. Thus an unphysical phenomenon, usually called “ghost force”, will occur near the interface between atomistic and coarse-grained regions.

This aforementioned interface mismatch has motivated the development of the nonlocal Quasicontinuum framework [13, 34, 37, 57]. In the nonlocal QC approach, atomistic description is consistently used in both atomistic region and coarse-grained domain. The energy and force calculations in the coarse-grained domain are exactly the same as what we do for full atomistic description. The only difference is that the gray atoms (gray dots in Figure 2.4) are not degrees of freedoms (DOFs) of the system anymore. The information of these gray atoms can be determined by interpolating the information of the nodal atoms (red dots in Figure 2.4). The main challenge within the nonlocal QC method or coarse-grained atomistic framework is how to efficiently and accurately evaluate the potential energy for the coarse-grained region, as shown in Eq.(2.2).

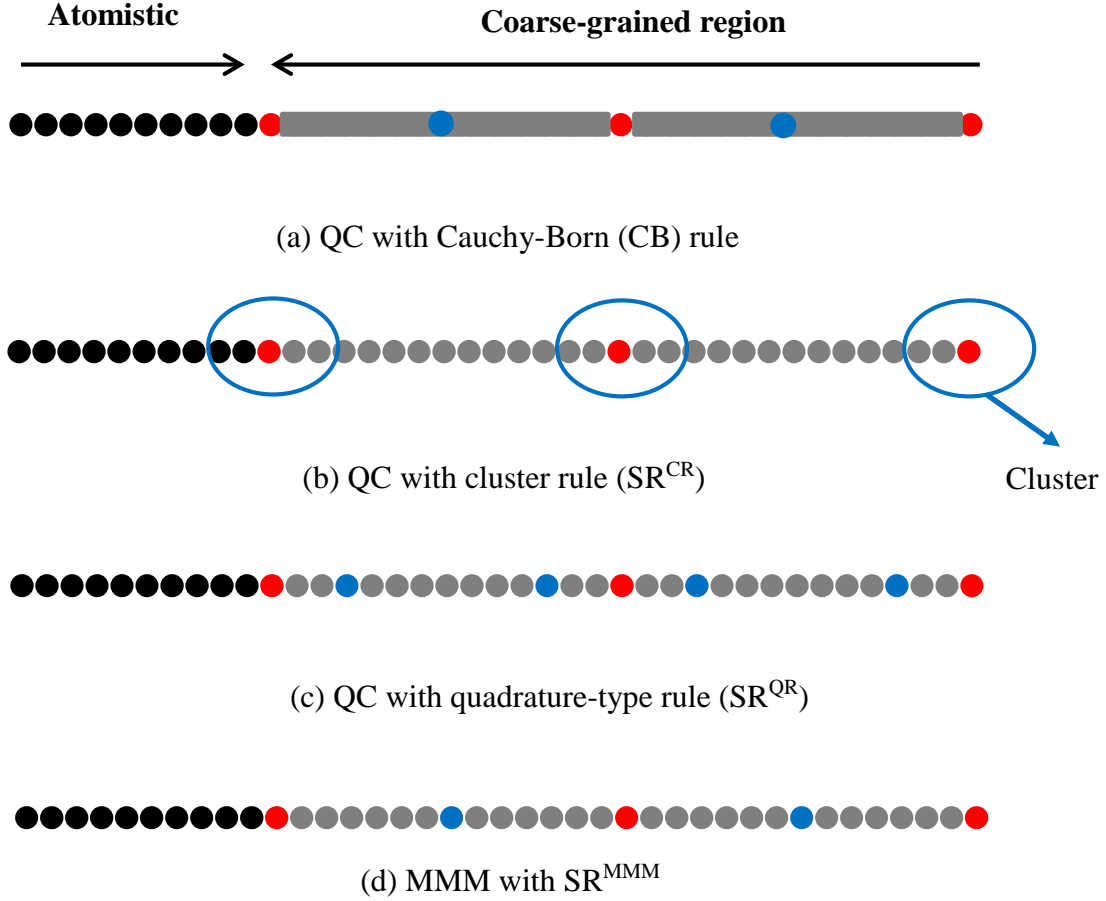


Figure 2.4: Schematically illustration of Quasicontinuum method with the respectively Cauchy-Born rule (a), cluster rule (SR^{CR}) (b), quadrature-type rule (SR^{QR}) and MMM with SR^{MMM} , using two 1D linear elements in the coarse-grained region

To overcome this challenge, the nodal summation rule was first proposed to efficiently calculate the potential energy [13]. The proposed nodal summation rule is similar to the nodal integration rule in numerical integration and it caused numerical instability issue due the inaccurate approximation of the potential energy. And to remove the instability problem, the cluster summation rule (SR^{CR}) was designed. The basic idea of SR^{CR} is to use the energy of clusters with a certain radius (circles in Figure 2.4b) to sample the energy of each element in

Section 2.3.2. And in order to determine the weight of each cluster, the assumption that the energy distribution of a piece-wise linear element is also piece-wise linear is made. Then the weight for each cluster is determined by reproducing the assumed piece-wise linear energy distribution for each element. However, from our analysis in Section 2.3.2, we know that atoms in each cluster, similar to element edge atoms, have very different energy distribution from that of element bulk atoms. Since large elements are usually used to efficiently coarse-grain atomistic models, the number of bulk atoms dominates the number of atoms in each cluster. As such, SR^{CR} will introduce large errors in approximating the potential energy for coarse-grained region, as has been mathematically shown in [118]. In addition, SR^{CR} was originally designed for linear element in [13]. Though some work has been done using high order elements with SR^{CR} , the way to determine the weight for each cluster was the same as for linear element, following the piece-wise energy distribution assumption [69]. As such, the relationship about how the employed element type or interpolation shape function affects SR^{CR} is not clear.

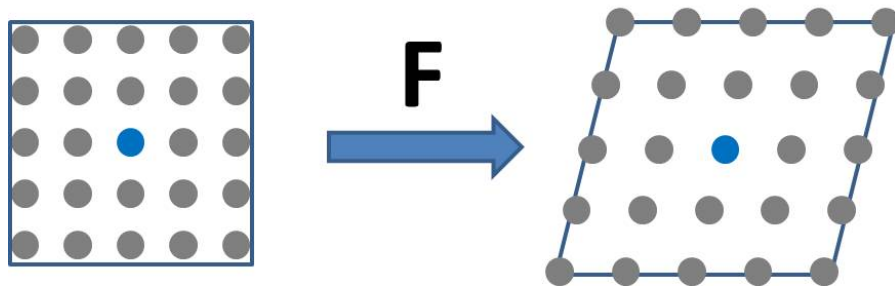


Figure 2.5: A schematic illustration of the Cauchy-Born rule in 2D: an atomic unit cell centered at a quadrature point (blue dot) is assumed to deform uniformly according to the deformation gradient \mathbf{F} at the quadrature point

The quadrature-type summation rule was proposed in [35, 36] to avoid drawbacks of SR^{CR} . The general idea of SR^{QR} is to firstly select some quadrature-type or sampling atoms (blue dots in Figure 2.4c). And the energy of selected sampling atoms is then employed to sample the energy of each element. Similar to SR^{CR} , the weight for each sampling atom is determined by assuming that the energy distribution of each piece-wise linear element is also piece-wise linear. As such, two sampling atoms are selected in each linear element (Figure 2.4c). To determine position of sampling atoms, the atoms nearest to $L/3$ and $2L/3$ are selected where L is the length of a 1D linear element. SR^{QR} was originally employed in 1D linear element in [35] and its extension to high order element is not clearly stated.

The proposed SR^{MMM} in Section 2.2 is also based on the coarse-grained atomistic framework such that atomistic description is consistently used across the whole system. The distinguishing feature of SR^{MMM} is that the energy distribution of each element can be analytically derived for harmonic potentials. As such, the optimal (minimum) number of sampling atoms and their weights can be analytically formulated. For instance, based on the proposed SR^{MMM} , the energy distribution of element bulk atoms in the employed linear element is piece-wise constant (see Table 2.2) such that only one sampling atom is selected (Figure 2.4d). It is worth to note that similarity exists between SR^{MMM} and the summation rules proposed in [37, 57] with respect to linear element type. However, what distinguishes SR^{MMM} from other summation rules is that SR^{MMM} is derived for general element types. In that sense, the proposed MMM with SR^{MMM} is the generalization of the nonlocal Quasicontinuum method. Table 2.1 summarizes the comparison of several summation rules discussed in this section in terms of the employed constitutive model, energy distribution and originally applied element types in the coarse-grained region.

Table 2.1: A qualitatively comparison of several different summation rules

Method	Constitutive model	Energy distribution	Element type
QC-CB	Continuum description	Piece-wise constant	Linear
QC-SR ^{CR}	Atomistic description	Piece-wise linear (assumed)	Linear
QC-SR ^{QR}	Atomistic description	Piece-wise linear (assumed)	Linear
MMM-SR ^{MMM}	Atomistic description	Analytical (for harmonic potentials)	General

2.4 REMARKS OF SR^{MMM} ON NONLINEAR POTENTIALS



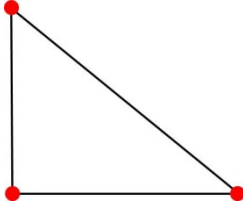
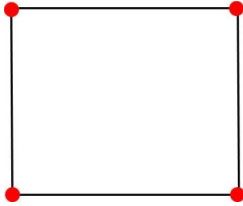
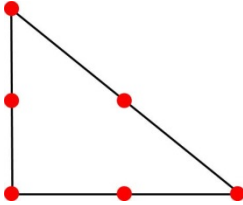
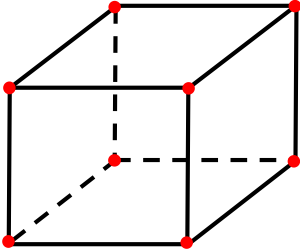
In conventional FEM, the selected order of quadrature rule to evaluate the energy (Eq. (2.3)) or stiffness integral (Eq. (2.4)) is generally determined by the accuracy of Gauss quadrature for linear elasticity. For nonlinear continuum constitutive relationships, a relatively higher order of Gauss quadrature may be employed, especially for large deformation problems.

Similarly, SR^{MMM} has been introduced by assuming a nonlocal harmonic spring potential, as mentioned earlier. However, since any nonlinear interatomic potential can be well-approximated by a harmonic spring within its convex region, SR^{MMM} may be expected to be effective for nonlinear potentials, as will be demonstrated in Chapters 3.0 and 4.0 . In fact, the proposed SR^{MMM} framework is interatomic-potential independent. As such, we do not employ a specific form for the assumed harmonic spring potential in the derivation of SR^{MMM}. The proposed SR^{MMM} can be directly applied to a general form of pair or many-body potential. For

cases where large deformation is expected, a relatively higher order of SR^{MMM} may be employed, as quadrature rules in FEM.

Note that for atomistic regions where interatomic potential is within its non-convex domain, full molecular mechanics can be employed since defects are likely to occur in that region. Since MMM is a fully coarse-grain atomistic model and no continuum description is introduced, full molecular mechanics can be directly and organically incorporated into MMM without any modification. Table 2.2 summarizes the employed bulk summation rule SR^B for several element types.

Table 2.2: The employed bulk summation rule SR^B for different element types

	Element type	Function basis of SR^B	Optimal number of PSAs
1D	Linear element 	1	1
	Quadratic element 	$1, x, x^2$	3
2D	Linear triangle element 	1	1
	Bilinear quadrilateral element 	$1, x, y, xy, x^2, y^2$	6
	Quadratic triangle element 	$1, x, y, xy, x^2, y^2$	6
3D	Tri-linear hexahedral element 	$1, x, y, z, xy, xz, yz, x^2, y^2, y^2$	10

2.5 SUMMARY OF ATOM CLASSIFICATION

So far, different atom types such as primary sampling atoms (PSAs), secondary sampling atoms (SSAs) and non-sampling atoms (NSAs) have been introduced from the perspective of energy sampling in the coarse-grained region. In this section, atoms will be classified from the point of view of degrees of freedom (DOFs) for the case that both atomistic and coarse-grained regions exist. Then the definition and role of each atom type will be summarized.

Figure 2.6 shows a comprehensive MMM model where molecular mechanics is employed around the crack in the middle of the panel and the proposed summation SR^{MMM} ($SR^B + SR^S$) is used in the coarse-grained region and surface that are away from the crack. In this thesis, atoms in the atomistic region will be colored black. Note that only the information of atoms (black dots) in the atomistic region and nodal atoms (red dots) that coincide with element nodes are the DOFs of the MMM model. As such, these atoms (black and red dots) are named as representative atoms (rep-atoms) and the rest atoms are called ghost atoms. In addition, since only the nodal atoms play a role in the interpolation shape function, the nodal atoms are also called interpolating rep-atoms and the atoms in the atomistic region non-interpolating rep-atoms.

In addition, since the atoms in the atomistic region behave in the same way as in full atomistic simulation, their energy is considered explicitly. As such, from the point of view of energy sampling, they belong to secondary sampling atoms (SSAs). Since nodal atoms also belong to SSAs, all the rep-atoms are SSAs.

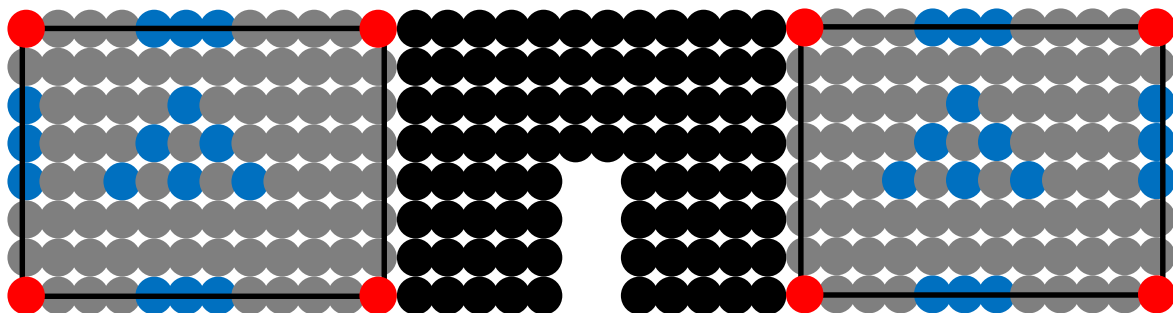


Figure 2.6: A MMM model where both atomistic and coarse-grained regions exist. Molecular mechanics (black area) is employed to capture crack propagation and SR^{MMM} is employed in the coarse-grained region far away from the crack.

To summarize, atoms are classified into rep-atoms and ghost atoms from the perspective of DOFs and atoms are grouped into *PSAs*, *SSAs*, and *NSAs* from the angle of energy sampling. The definition and role of each atom type from different points of view are presented in Table 2.3 and Table 2.4, respectively.

Table 2.3: Classification of different atom types in MMM from the perspective of degrees of freedom (DOFs)

Atom classification: from the perspective of DOFs	Rep-atom: atom: whose information is the DOFs of the coarse-grained system	Interpolating rep-atom: rep- atom that takes part in constructing shape function
	Ghost atom: atom whose coordinate is given by interpolation	Non-interpolating atom: rep- atoms that resides in the atomistic region

Table 2.4: Classification of different atom types in MMM from the perspective of energy sampling

	Primary sampling	Secondary sampling	Non-sampling atom:
Atom classification: from the point of view of energy sampling	atom: an atom whose energy is employed to represent the energy of itself and the non- sampling atoms	atom: an atom whose energy is used to represent the energy of itself only and is explicitly calculated	an atom whose energy is represented by the energy of a primary sampling atom

2.6 GOVERNING EQUATIONS

In this section, the governing equations of MMM employing SR^{MMM} ($\text{SR}^{\text{B}} + \text{SR}^{\text{S}}$) will be derived from the potential energy approximation \tilde{E}_a following the variational principle. As

mentioned in Section 2.4, we do not assume a specific form of the interatomic potential E_i employed below.

Since atoms are classified into *PSAs*, *SSAs* and *NSAs* from the perspective of energy sampling, then \tilde{E}_a in Eq. (2.2) can be reformed as:

$$\tilde{E}_a = \sum_{i \in \mathcal{N}_S} w_i^a E_i = \sum_{i \in \mathcal{N}_{SSA}} E_i + \sum_{i \in \mathcal{N}_{PSA}} w_i^a E_i \quad (2.30)$$

where \mathcal{N}_{SSA} and \mathcal{N}_{PSA} are the respective index set of *SSAs* and *PSAs*. Note that $w_i^a = 1$ for each *SSA* and w_i^a is determined in SR^{MMM} except that Eq. (2.21) has to be modified to account for the introduction of *SSAs*, as follows:

$$w_i^a = \sum_{j \in (\mathcal{N}_A \setminus \mathcal{N}_{SSA})} \Phi_i(x_a^j) \quad (2.31)$$

Let \mathbf{U}^a denote the displacement vector for all the N_n^a nodal atoms and $\mathbf{f}_\alpha^{\text{ext}}$ be an external force vector applied to an atom $\alpha \in \mathcal{N}_A$. Following the variational principle to derive the equilibrium equations of an MMM model, the negative derivative of \tilde{E}_a with respect to the nodal displace vector $\mathbf{u}_i^a, i \in \mathcal{N}_n^a$, which are the degrees of freedom in MMM as in FEM, must be zero.

Then we have:

$$\mathbf{F}_i^a(\mathbf{U}^a) = - \sum_{j \in \mathcal{N}_{SSA}} \frac{\partial E_j(\mathbf{U}^a)}{\partial \mathbf{u}_i^a} - \sum_{k \in \mathcal{N}_{PSA}} w_k^a \frac{\partial E_k(\mathbf{U}^a)}{\partial \mathbf{u}_i^a} + \sum_{\alpha \in \mathcal{N}_A} \phi_i(\mathbf{r} = \mathbf{r}_{\alpha 0}) \mathbf{f}_\alpha^{\text{ext}} = \mathbf{0}, \forall i \in \mathcal{N}_n^a \quad (2.32)$$

where $\mathbf{f}_\alpha^{\text{ext}}$ is partitioned to a nodal atom as in FEM. Eq. (2.32) is the governing equations of MMM for statics in general.

2.7 SUMMARY

To summarize, the framework of the proposed multiresolution molecular mechanics (MMM) is introduced by analogy to the well-known finite element method (FEM). The novelty of MMM

lies in the proposed summation rule SR^{MMM} to determine the optimal number, weight and position for quadrature-type (sampling) atoms to evaluate finite energy summations in coarse-grained molecular mechanics model, similar to quadrature rules to evaluate integrals involved in FEM .

The derivation of SR^{MMM} is valid for general interpolation shape functions. The idea is to analytically derive the energy distribution of the coarse-grained region for harmonic interatomic potential, and then accurately represents the energy distribution by selecting sampling atoms in a curve-fitting-like process. SR^{MMM} is then consistently decomposed into the bulk summation rule SR^B and the surface summation rule SR^S . Mathematically, this decomposition is based on the observation that the energy distribution of surface area is different from that of the bulk domain. Physically, the difference is due to the fact that surface atoms lack bonding neighbors and are not fully coordinated compared with their bulk counterpart. In addition, the effectiveness of SR^{MMM} for nonlinear potentials is also discussed.

The definitions of different atom types are clearly tabulated for referencing convenience, and the governing equations are derived following the variational principle. This chapter lays down the theoretical foundations for the following chapters.

3.0 NUMERICAL VALIDATION OF BULK SUMMATION RULE: SR^B

In this Chapter, in order to quantify the performance of MMM, error norms, as inspired by the L_2 and H_1 norm in continuum mechanics to analyze the performance of FEM, are defined in the respective displacement and energy field. Then different error sources (discretization error and sampling error) are identified and quantified by the defined norm. The defined sampling error can serve as a good indicator of the accuracy of any proposed summation rule. To validate the proposed bulk summation rule SR^B and compare SR^B with other summation rules, a harmonic interatomic potential is employed first. Then the extension to non-harmonic interatomic potential is presented by taking the standard Lennard-Jones (LJ) potential as a representative. Numerical examples such as high order atomic sheet shear and beam bending are considered by employing linear, bilinear and quadratic interpolation shape functions. A crack propagation problem is employed to show the capability of MMM to capture material defects.

3.1 ERROR SOURCES

It is well-known that there are two different types of error in conventional FEM: (I) discretization error that relates to the employed element size and shape function order and (II) numerical integration error that relates to the quadrature rule utilized to evaluate involved integrals. Similarly, there are also two different error sources in MMM: (I) discretization error as

in FEM and (II) sampling error that relates to the employed summation rules to evaluate involved finite summations.

As a simple example, let \mathbf{U}^{FA} be the displacement solution vector from full atomistic simulation (Model A in Figure 3.1) and \mathbf{U}^{MMM} be the one from MMM calculation (Model B in Figure 3.1). In addition, in order to quantify the discretization error, a special MMM model (Model C in Figure 3.1) is designed. In Model C, after using finite elements to coarse-grain full atomistic model, the energy of each atom is considered explicitly such that each atom is taken as a second sampling atom (SSA), denoted as green dots in this thesis. We note that nodal atoms (red dots in Figure 3.1) belong to SSA. Since they also represent degrees of freedom, we stay with color red for them. In Model C, there is only discretization error and no any other error is introduced. As such, model c is, in general, the most accurate and of course, the most computationally intensive model one can have for a given discretization. Since there is no primary sampling atom (PSA) in Model C, we denote the displacement field gained from it as $\mathbf{U}_{0\text{p}*s}^{\text{MMM}}$ with “0p” meaning no PSA and “*s” representing SSA everywhere.

As such, for displacement field, the distance between Mode A and Model B, e_U^{tot} can be decomposed as:

$$\mathbf{U}^{\text{FA}} - \mathbf{U}^{\text{MMM}} = \underbrace{\mathbf{U}^{\text{FA}} - \mathbf{U}_{0\text{p}*s}^{\text{MMM}}}_{\text{discretization error}} + \underbrace{\mathbf{U}_{0\text{p}*s}^{\text{MMM}} - \mathbf{U}^{\text{MMM}}}_{\text{sampling error}} \quad (3.1)$$

where $\mathbf{U}^{\text{FA}} - \mathbf{U}_{0\text{p}*s}^{\text{MMM}}$ is the distance between Model A and Model C, named as discretization error e_U^{disc} and $\mathbf{U}_{0\text{p}*s}^{\text{MMM}} - \mathbf{U}^{\text{MMM}}$ is the distance between Model C and Model B, named as sampling error e_U^{sam} . The different types of error are schematically shown in Figure 3.1

For a given discretization, the discretization error e_U^{disc} is fixed. Then a good indicator to estimate the performance of a coarse-grained model or a summation rule is to identify the

sampling error. As many other coarse-grained models do not clearly differentiate and quantify different error sources, we note that the identification of different error types is important, especially when spatial convergence is performed, as will be shown in Chapter 5.0 .

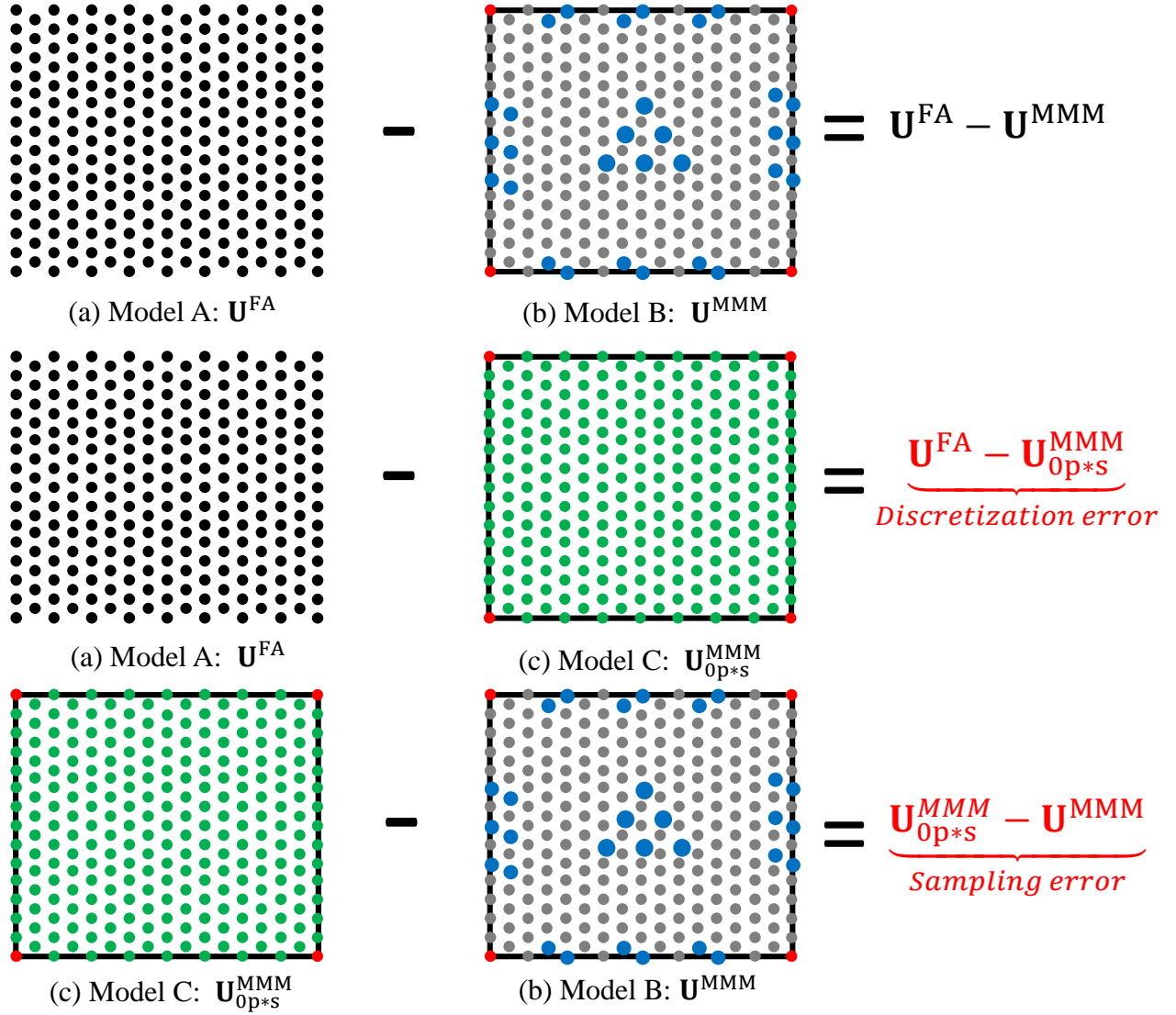


Figure 3.1: Schematically demonstration of error sources and types: Model A: full atomistic model; Model B: a general MMM model with SR^{MMM} ; Model C: a specifically designed model

where the energy of each atom is explicitly considered. Discretization error is fixed for a given mesh.

3.2 ERROR NORMS

It is well-known that the following L_2 and H_1 error norms are widely employed to quantify the performance of FEM in continuum mechanics [122]:

$$e_U = \left[\int_{\Omega^c} (\mathbf{U}^{\text{exact}} - \mathbf{U}^{\text{FEM}})^T (\mathbf{U}^{\text{exact}} - \mathbf{U}^{\text{FEM}}) d\Omega^c \right]^{1/2} \quad (3.2)$$

$$e_E = \left[\int_{\Omega^c} (\boldsymbol{\epsilon}^{\text{exact}} - \boldsymbol{\epsilon}^{\text{FEM}})^T (\boldsymbol{\epsilon}^{\text{exact}} - \boldsymbol{\epsilon}^{\text{FEM}}) d\Omega^c \right]^{1/2} \quad (3.3)$$

where e_U and e_E are the errors in displacement and energy fields, respectively, $\mathbf{U}^{\text{exact}}$ and $\boldsymbol{\epsilon}^{\text{exact}}$ are the respective displacement and strain fields from exact solution.

Similarly, inspired by the L_2 and H_1 norms in continuum mechanics, the following two norms are defined to quantify the accuracy of MMM in atomistic modeling:

$$e_U^{\text{total}} = \left[\frac{\sum_{i \in \mathcal{N}_A} (\mathbf{u}_i^{\text{FA}} - \mathbf{u}_i^{\text{MMM}})^T (\mathbf{u}_i^{\text{FA}} - \mathbf{u}_i^{\text{MMM}})}{\sum_{i \in \mathcal{N}_A} (\mathbf{u}_i^{\text{FA}})^T \mathbf{u}_i^{\text{FA}}} \right]^{1/2} = \frac{\|\mathbf{U}^{\text{FA}} - \mathbf{U}^{\text{MMM}}\|_2}{\|\mathbf{U}^{\text{FA}}\|_2} \quad (3.4)$$

$$e_E^{\text{total}} = \left[\frac{\sum_{i \in \mathcal{N}_A} \sum_{j \in \mathcal{N}_i} ((\mathbf{r}_{ij}^{\text{FA}} - \mathbf{r}_{ij}^0) - (\mathbf{r}_{ij}^{\text{MMM}} - \mathbf{r}_{ij}^0))^T ((\mathbf{r}_{ij}^{\text{FA}} - \mathbf{r}_{ij}^0) - (\mathbf{r}_{ij}^{\text{MMM}} - \mathbf{r}_{ij}^0))}{\sum_{i \in \mathcal{N}_A} \sum_{j \in \mathcal{N}_i} (\mathbf{r}_{ij}^{\text{FA}} - \mathbf{r}_{ij}^0)^T (\mathbf{r}_{ij}^{\text{FA}} - \mathbf{r}_{ij}^0)} \right]^{1/2} \quad (3.5)$$

where \mathbf{u}_i^{FA} and $\mathbf{u}_i^{\text{MMM}}$ are the displacement vectors from full atomistic calculation and a MMM model, respectively, for an atom $i \in \mathcal{N}_A$; \mathcal{N}_i is the index set of neighbors of the i th atom, $\mathbf{r}_{ij}^{\text{FA}}$ and $\mathbf{r}_{ij}^{\text{MMM}}$ denote the pair distance vector from each model and \mathbf{r}_{ij}^0 represents the initial pair distance vector. Note that all the errors are normalized by the solution from full atomistic model.

In linear elasticity, the potential energy of a continuum model is a function in terms of strain fields $\boldsymbol{\epsilon}$ such that Eq. (3.3) defines error in energy field. For an atomistic model, the strain field is not defined here. Instead, the pair distance vectors are measured for the reason that interatomic (pair) potential energy is a function in terms of pair distance, analogous to the strain defined in continuum mechanics. We note that even for many-body potentials, the difference in each pair distance vector is a good error indicator in potential energy. As such, the differences in strain vector field and in pair distance vector field are good error indicators in energy for the respective continuum and atomistic modeling.

We note that in many of the existing works, errors are always measured in such a way that the displacement vectors \mathbf{U} or pair distance vector \mathbf{r}_{ij} from different models are first operated to generate a scalar and then the difference between generated scalars is employed as the error. For instance, let E_{tot}^{FA} and \tilde{E}_{tot} be the respective total potential energy scalar from atomistic modeling and any other model generated by operations on the respective \mathbf{r}_{ij} or \mathbf{U} from each model, then the error is calculated as:

$$err = \left| \frac{E_{tot}^{FA} - \tilde{E}_{tot}}{E_{tot}^{FA}} \right| \quad (3.6)$$

We comment that this is not a good error indicator because there are cases that the difference, for instance, in displacement field is significant but err is quite small, as schematically shown in Figure 3.2. In contrast, the error norms defined in Eqs. (3.4)-(3.5) can eliminate this possibility.

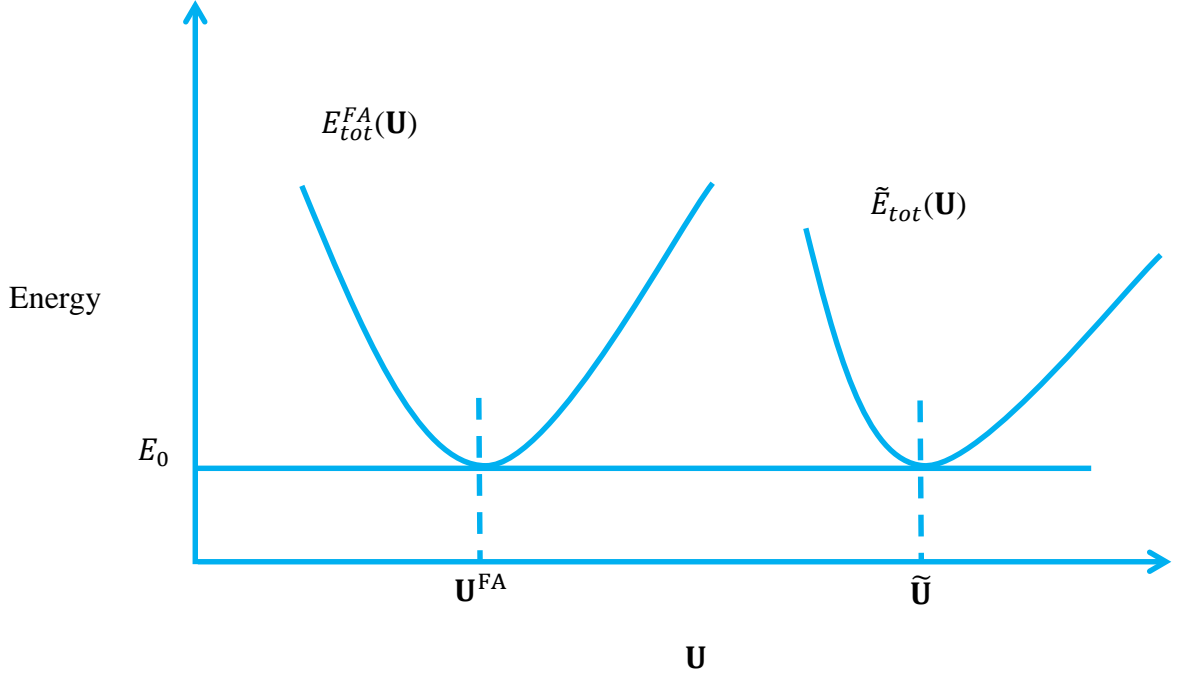


Figure 3.2: Schematically illustration of the possibility in an error estimator that the distance between different displacement fields could be very large even though they produce the same potential energy scalar E_0 : \mathbf{U}^{FA} is from full atomistic simulation and $\tilde{\mathbf{U}}$ from any other approximation

Then using the error norms defined in Eq.(3.4), the discretization error e_U^{disc} and sampling error e_U^{sam} in displacement field are quantified as:

$$e_U^{disc} = \left[\frac{\sum_{i \in \mathcal{N}_A} (\mathbf{u}_i^{FA} - \mathbf{u}_{0p*s_i}^{MMM})^T (\mathbf{u}_i^{FA} - \mathbf{u}_{0p*s_i}^{MMM})}{\sum_{i \in \mathcal{N}_A} (\mathbf{u}_i^{FA})^T \mathbf{u}_i^{FA}} \right]^{1/2} = \frac{\|\mathbf{U}^{FA} - \mathbf{U}_{0p*s}^{MMM}\|_2}{\|\mathbf{U}^{FA}\|_2} \quad (3.7)$$

$$e_U^{sam} = \left[\frac{\sum_{i \in \mathcal{N}_A} (\mathbf{u}_{0p*s_i}^{MMM} - \mathbf{u}_i^{MMM})^T ((\mathbf{u}_{0p*s_i}^{MMM} - \mathbf{u}_i^{MMM}))}{\sum_{i \in \mathcal{N}_A} (\mathbf{u}_i^{FA})^T \mathbf{u}_i^{FA}} \right]^{1/2} = \frac{\|\mathbf{U}_{0p*s}^{MMM} - \mathbf{U}^{MMM}\|_2}{\|\mathbf{U}^{FA}\|_2} \quad (3.8)$$

Note that e_U^{total} , e_U^{disc} and e_U^{sam} are all normalized by $\|\mathbf{U}^{FA}\|_2$ such that they are comparable to each other.

Similarly, the discretization error e_E^{disc} and sampling error e_E^{sam} in energy field are defined as:

$$e_E^{disc} = \left[\frac{\sum_{i \in \mathcal{N}_A} \sum_{j \in \mathcal{N}_i} \left((\mathbf{r}_{ij}^{FA} - \mathbf{r}_{ij}^0) - (\mathbf{r}_{0p*s_{ij}}^{MMM} - \mathbf{r}_{ij}^0) \right)^T \left((\mathbf{r}_{ij}^{FA} - \mathbf{r}_{ij}^0) - (\mathbf{r}_{0p*s_{ij}}^{MMM} - \mathbf{r}_{ij}^0) \right)}{\sum_{i \in \mathcal{N}_A} \sum_{j \in \mathcal{N}_i} \left((\mathbf{r}_{ij}^{FA} - \mathbf{r}_{ij}^0) \right)^T \left((\mathbf{r}_{ij}^{FA} - \mathbf{r}_{ij}^0) \right)} \right]^{1/2} \quad (3.9)$$

$$e_E^{sam} = \left[\frac{\sum_{i \in \mathcal{N}_A} \sum_{j \in \mathcal{N}_i} \left((\mathbf{r}_{0p*s_{ij}}^{MMM} - \mathbf{r}_{ij}^0) - (\mathbf{r}_{ij}^{MMM} - \mathbf{r}_{ij}^0) \right)^T \left((\mathbf{r}_{0p*s_{ij}}^{MMM} - \mathbf{r}_{ij}^0) - (\mathbf{r}_{ij}^{MMM} - \mathbf{r}_{ij}^0) \right)}{\sum_{i \in \mathcal{N}_A} \sum_{j \in \mathcal{N}_i} \left((\mathbf{r}_{ij}^{FA} - \mathbf{r}_{ij}^0) \right)^T \left((\mathbf{r}_{ij}^{FA} - \mathbf{r}_{ij}^0) \right)} \right]^{1/2} \quad (3.10)$$

The errors defined in this section will be employed to quantify the performance of MMM consistently throughout this thesis.

3.3 DEFINITIONS OF COMPARED SUMMATION RULES

In this section, different summation rules such as Gauss-quadrature-like rule are defined in order to compare against the proposed bulk summation rule SR^B . In this chapter, all surface atoms are treated as *SSAs* for all the summation rules employed such that SR^S is not employed. We name such a scheme as Scheme “#p~s”. The character “#” in front of “p” means the optimal number of *PSAs* in SR^B with “~” representing surfaces and “s” *SSA*. For instance, Scheme #p~s is equivalent to Scheme 1p~s for MMM with linear element since only one primary sampling atom is selected for each element (Figure 3.3a). Thus the weights of all employed summation rules are adjusted accordingly. The surface summation rule SR^S will be employed in Chapter 4.0 to specifically capture surface effects

Let h_x and h_y denote the nearest nodal spacing for different orders of element in x and y directions, respectively. Let “Gauss1”, “Gauss2”, “Gauss3”, “Gauss4” and “Gauss5” represent

the first five orders of Gauss-quadrature-like rule employed. For 1D linear element, they denote how many quadrature points are employed; for instance, “Gauss3” means 3 Gauss quadrature points are selected. For 2D bilinear element, they represent the number of Gauss quadrature points selected in each direction; e.g., “Gauss3” means 3x3 Gauss quadrature. For 2D triangular element, they denote the first, second, third, fourth and fifth order Gauss quadrature, respectively. Note that if a prescribed Gauss quadrature point location does not align with an atom location, and then the nearest atom is selected instead.

Let SR^B-1 , SR^B-2 and SR^{naive} represent three different choices of positions of *PSAs* within the framework of SR^B . SR^B-1 is designed to directly compare with the corresponding Gauss quadrature (if possible). SR^B-2 is designed to compare with SR^B-1 to study the effect of the *PSA* positions on the accuracy of SR^B . SR^{naive} is designed to show the potential drawbacks of an inaccurate summation rule due to the naive choice of *PSA*.

For 1D linear element (2 linear elements in Figure 3.3), “Gauss1” (SR^B-1) (Figure 3.3a), SR^B-2 (Figure 3.3b) and SR^{naive} (Figure 3.3c) are employed respectively. Note that Gauss1 and SR^B-1 are identical in this case.

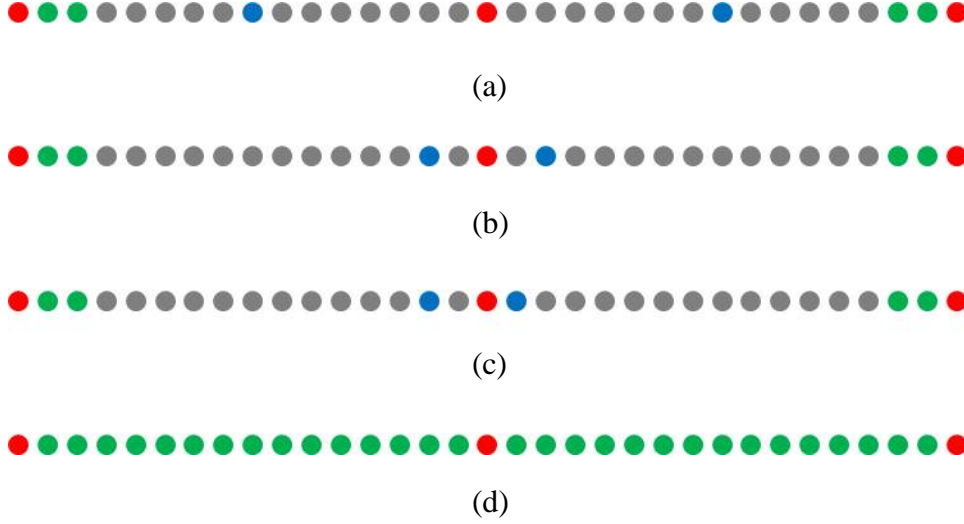


Figure 3.3: Schematic illustrations of primary sampling atom selections for different summation rules employed for 1D linear element: Gauss1 and SR^B-1 (a), SR^B-2 (b), SR^{naive} (c) and Scheme $Op*s$ (d).

For 1D quadratic element (one quadratic element in Figure 3.4), eight different summation rules are used: four different orders of Gauss quadrature; two proposed bulk summation rules (SR^B-1 and SR^B-2) and two other summation rules (“bisection” and “quartering” defined below) inspired from numerical integration. The *PSA* selections for Gauss1, Gauss 2, Gauss 3 and Gauss 4 are shown in Figure 3.4a, Figure 3.4b, Figure 3.4e and Figure 3.4f, respectively. To compare with “Gauss2”, two of the three interior points that quarters an element (Figure 3.4c) are selected as *PSAs* and the corresponding weight for each is determined by evenly dividing the numbers of *NSAs* within that element. This summation rule is named “bisection”, which means that the *PSAs* bisects the nearest nodal spacing. Note that “bisection” and “Gauss2” have the same number of quadrature points by design. To directly compare with “Gauss3”, SR^B-1 employs the same *PSA* selection as used in “Gauss3” (Figure 3.4e). The

selected *PSAs* for SR^B-2 are shown in Figure 3.4d. To compare with “Gauss4”, four of the seven interior points that evenly divide an element (Figure 3.4g) are taken as *PSAs* and the associated weight for each is assigned through averaging the *NSA* number residing in that element. This summation rule is named “quartering”, which means that the *PSAs* quarters the nearest nodal spacing. Note that “quartering” and “Gauss4” have the same number of quadrature points by design. The summation rules shown in Figure 3.4 are presented in the order of number of quadrature points employed for each summation rule.

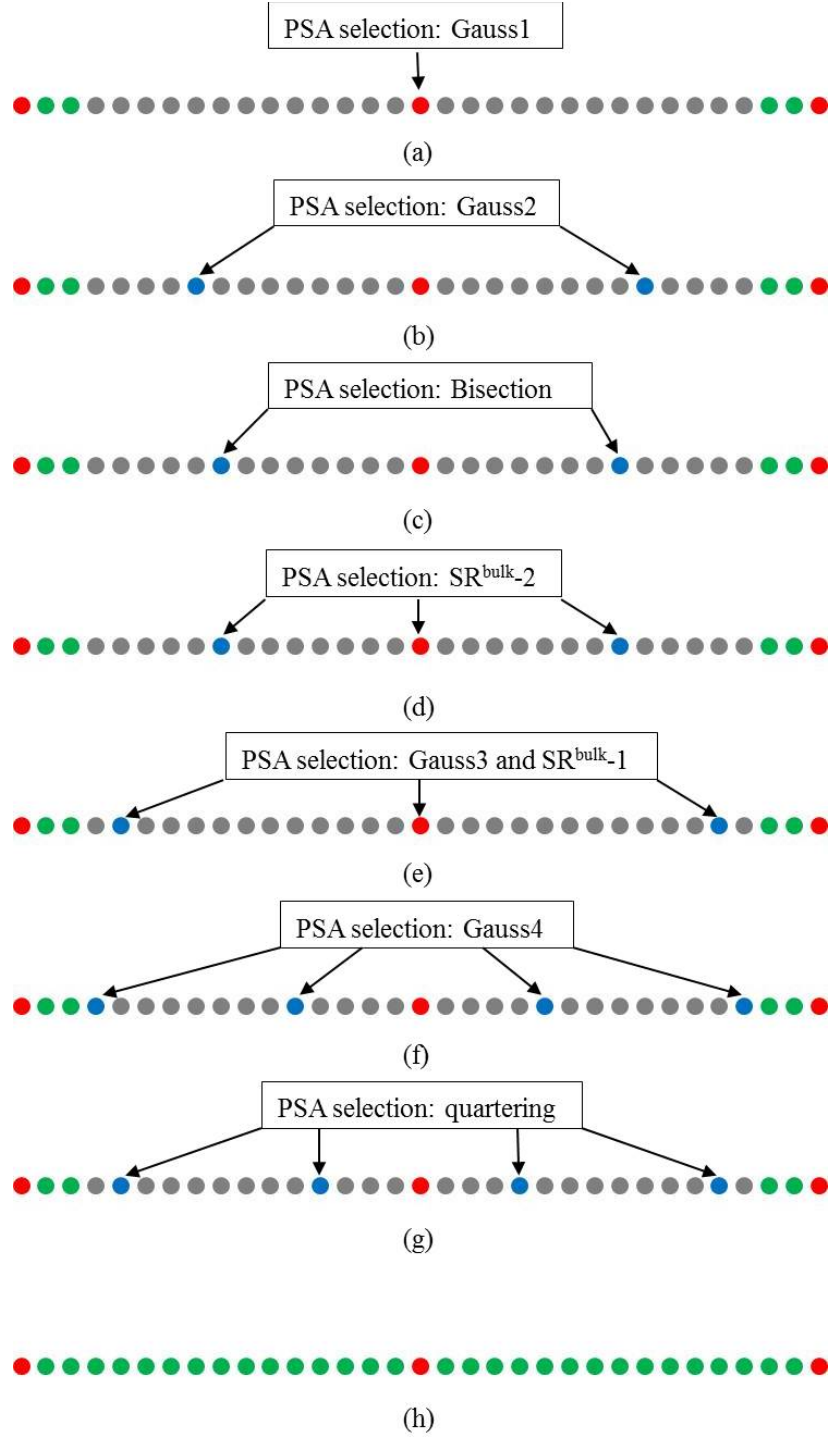


Figure 3.4: Schematic illustrations of primary sampling atom selections for different summation rules employed for 1D quadratic element: Gauss1 (a), Gauss2 (b), Bisection (c), SR^{B}_{-2} (d), SR^{B}_{-1} (e), Gauss4 (f), quartering (g) and Scheme Op*s (h)

In 2D, for linear triangle element (T3) (two T3s in Figure 3.5), “Gauss1” ($\text{SR}^{\text{B}}\text{-1}$), $\text{SR}^{\text{B}}\text{-2}$ and SR^{naive} are shown in Figure 3.5. For bilinear element (Q4), “bisection” defined in the 1D case is extended in y direction to compare with “Gauss2” (Figure 3.6a), as shown in Figure 3.6c. To compare with “Gauss3” (Figure 3.6b), “trisection” is defined in a similar way “bisection” is determined except that three of the five points that evenly divide h_x and h_y in each direction are employed as *PSAs*, as shown in Figure 3.6d. $\text{SR}^{\text{B}}\text{-1}$ and $\text{SR}^{\text{B}}\text{-2}$ are illustrated in Figure 3.7. For quadratic triangle element (T6) (two T6s in Figure 3.8 and Figure 3.9), different summation rules are illustrated in Figure 3.8 and Figure 3.9. Note that $\text{SR}^{\text{B}}\text{-1}$ and “Gauss4” share the same selection of *PSAs*.

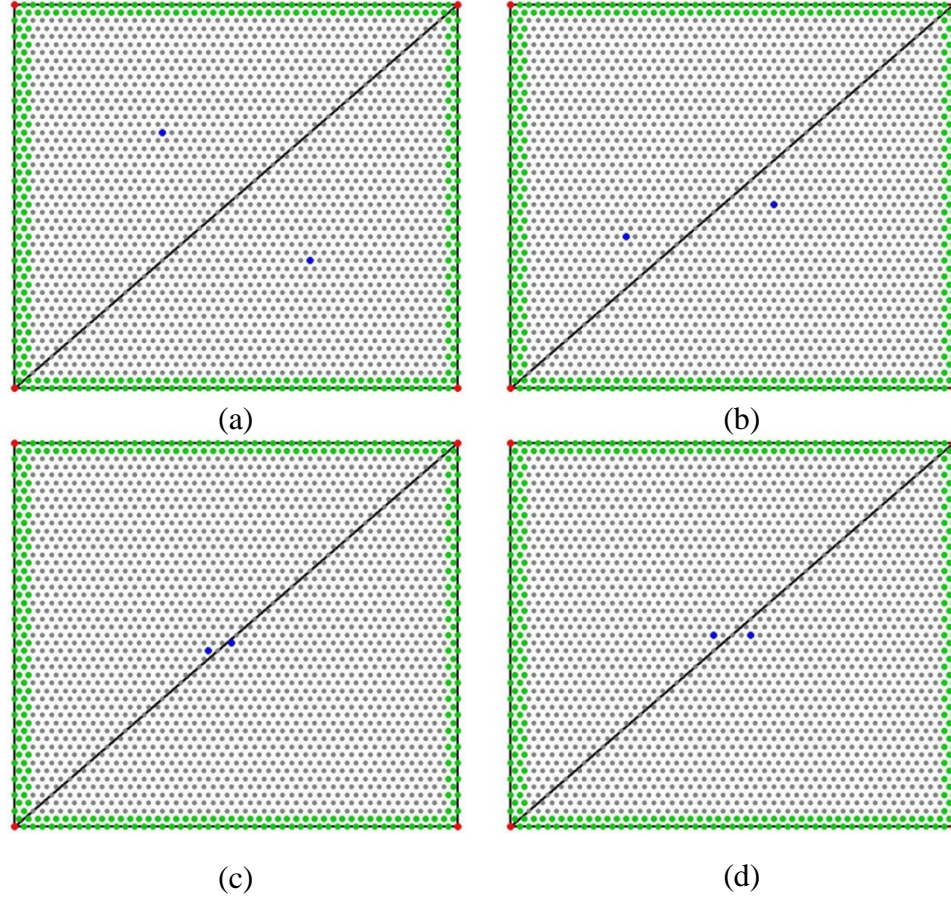


Figure 3.5: Schematic illustrations of primary sampling atom selections for different summation rules employed for 2D linear triangle element (T3): Gauss1 and SR^B-1 (a), SR^B-2 (b), SR^{naive} (c) for spring model and SR^{naive} (d) for LJ model.

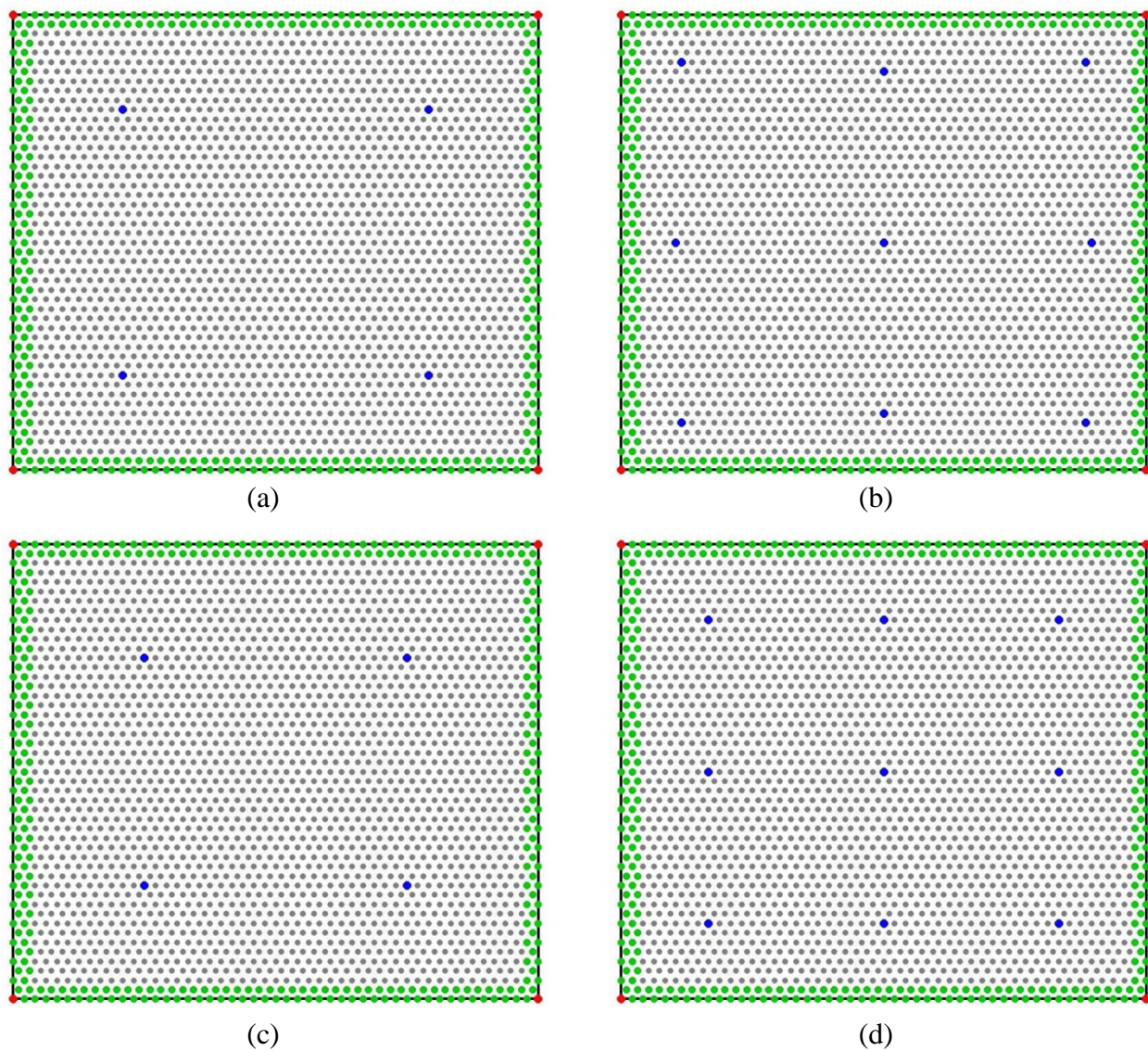


Figure 3.6: Schematic illustrations of primary sampling atom selections for different summation rules employed for 2D bilinear element (Q4). Part I: Gauss2 (a), Gauss3 (b), Bisection (c) and Trisection(d).

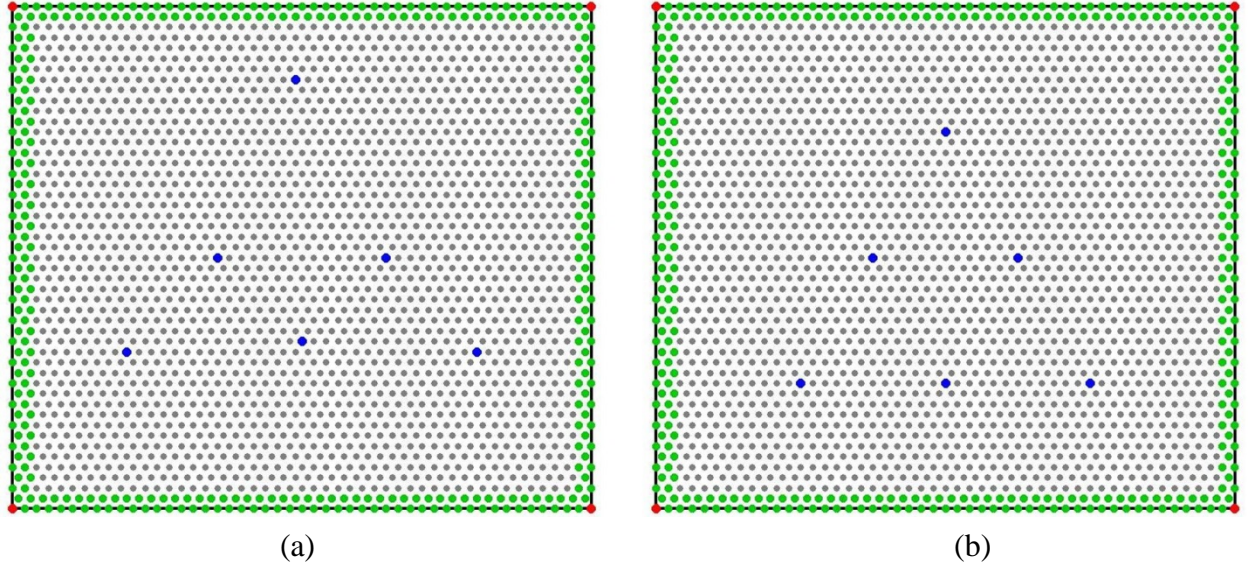


Figure 3.7: Schematic illustrations of primary sampling atom selections for different summation rules employed for 2D bilinear element (Q4). Part II: SR^B-1 (a) and SR^B-2 (b).

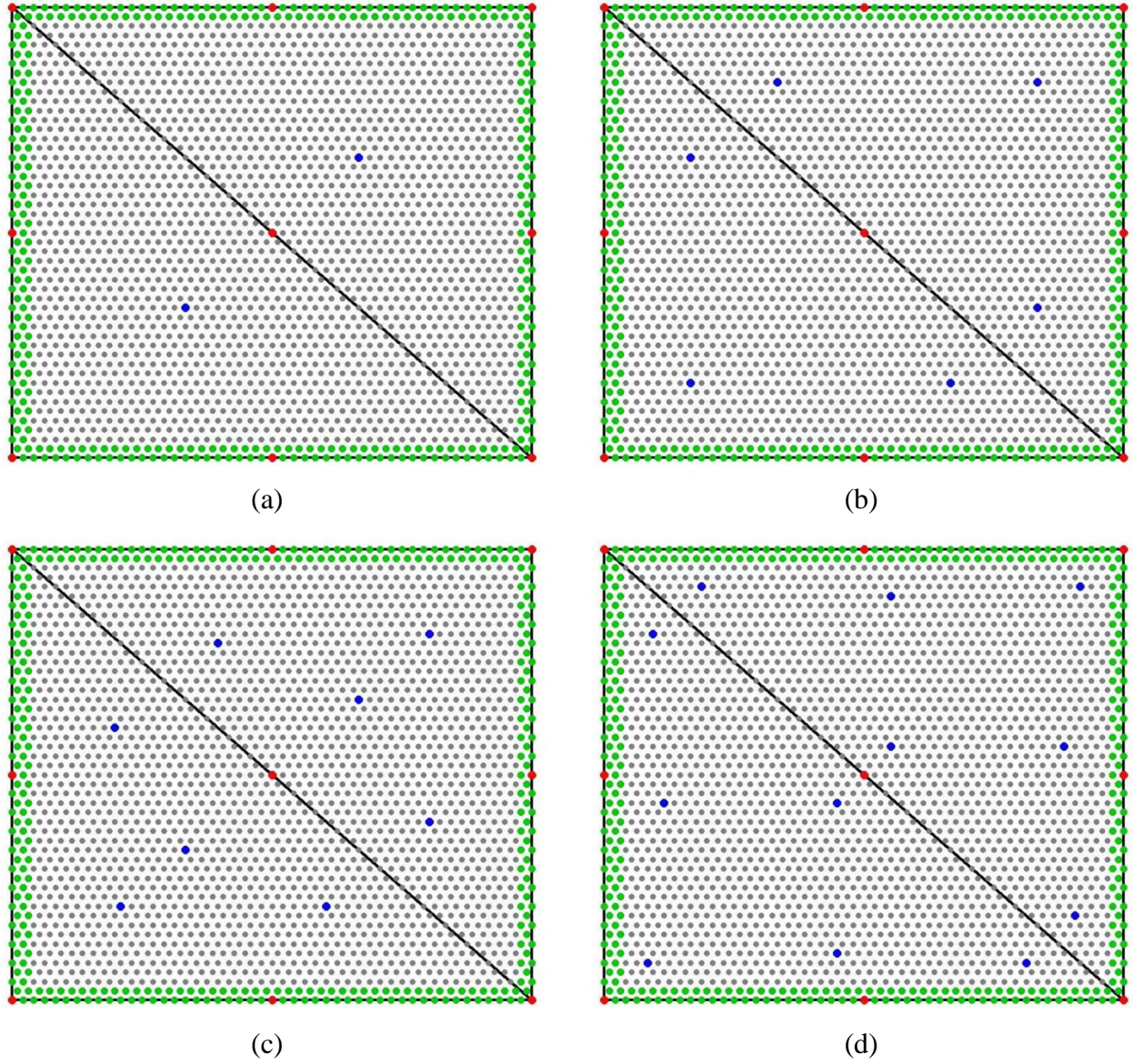


Figure 3.8: Schematic illustrations of primary sampling atom selections for different summation rules employed for 2D quadratic triangle element (T6). Part I: Gauss1 (a), Gauss2 (b), Gauss3(c), Gauss4 and SR^B-1 (d).

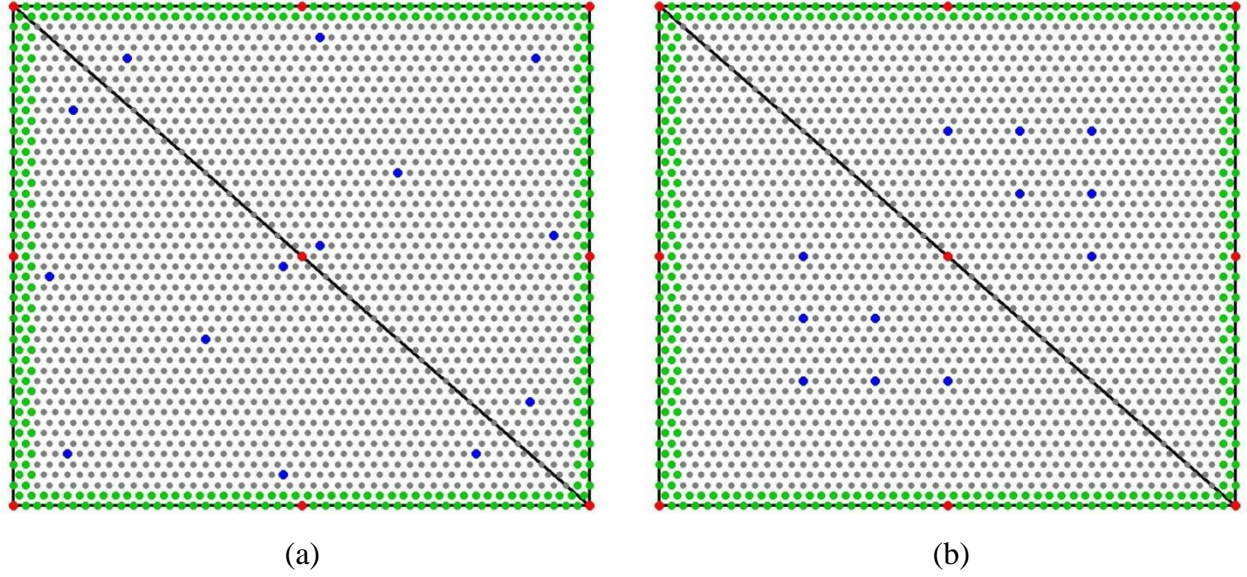


Figure 3.9: Schematic illustrations of primary sampling atom selections for different summation rules employed for 2D quadratic triangle element (T6). Part II: Gauss5 (a) and $\text{SR}^{\text{B}}\text{-2}$ (b).

3.4 VALIDATION FOR SPRING POTENTIAL

In this section, the proposed bulk summation rule SR^{B} will be validated and compared to the summation rules defined in Section 3.3 for a harmonic potential by employing linear, bilinear and quadratic elements.

3.4.1 1D quadratic tensile deformation

The 1D nonlocal spring model consists of 33 atoms with a harmonic potential considering the first and second nearest neighbor interactions. The atoms are initially placed as $r_i = ir_0$, $i = 1\text{-}33$, where r_0 is the zero-force spring length for the first neighbor springs. Let k_1 and k_2 represent the spring constants for the nearest-neighbor interaction and the second-neighbor interaction,

respectively. The zero-force spring lengths for the first neighbor spring and second neighbor spring are assumed to be r_0 and $2r_0$, respectively. In the numerical simulations, 1.0, 0.25, and 1.0 are assigned to be the values of k_1 , k_2 , r_0 , respectively.

The quadratic deformation field employed in [61, 123] to study the convergence of FEM, meshfree methods with linear element is used to validate SR^B. The quadratic deformation field takes the following form:

$$\mathbf{u} = -\frac{1}{2}X^2 + l_0X \quad (3.11)$$

where \mathbf{u} is the displacement and X represents the original atomic coordinate. Three steps are taken to generate such a deformation distribution: (I) Eq. (3.11) is used to generate the final deformation for each atom by substituting in its original coordinate; (II) the force required to balance each atom can be calculated with the given final deformation; (III) the forces from step II are employed as external forces and are applied to the atomic chain to generate the deformation given step I. The same three steps are also taken for the other simulations with a given displacement field other than Eq. (3.11). For boundary conditions, the atomic chain is fixed at the left end. The quadratic deformation defined above will also be employed to study the convergence behavior of MMM in Chapter 5.0 .

Linear and quadratic elements are employed with Scheme #p~s to verify SR^B. h_x is taken to be $16r_0$ for both linear and quadratic element, as shown in Figure 3.3 and Figure 3.4 . As a first step to perform the simulations, the function bases for SR^B are determined to be 1 for linear element and $1, x, x^2$ for quadratic element, respectively, as shown in Table 2.2. Thus, only one primary sampling atom is needed for linear element and three PSAs are required for quadratic element under the framework of SR^B. Based on this observation, the interpolant Φ_i for a primary sampling atom i in Eq. (2.16) is the constant 1 for linear element and is a quadratic function for

quadratic element. Then the corresponding weight can be determined by Eq. (2.21). To complete SR^B , the positions of the *PSAs* have to be determined. Since the global stiffness for the spring model employed is constant and thus is independent of atom positions, we claim that the SR^B is independent of the positions of *PSAs* as long as the selected primary sampling atom $i \in \mathcal{N}_{bulk}^e$ and are not coplanar, where \mathcal{N}_{bulk}^e means the index set of atoms that reside in the bulk region of an element. This claim will be verified by numerical simulations by choosing different positions of *PSAs*. The MMM models with linear and quadratic element using SR^B and different summation rules are illustrated in Figure 3.3 and Figure 3.4.

Table 3.1 shows results from different summation rules with linear element. Since “Gauss1” and SR^B -1 (Figure 3.3a) are the same for linear element, they produce the same results. With different choices of *PSAs*, SR^B -1 and SR^B -2 (Figure 3.3b) also yield the same accuracy. This shows that SR^B is independent of *PSA* positions as long as the selected primary sampling atom $i \in \mathcal{N}_{bulk}^e$. In SR^{naive} (Figure 3.3c), $i \in \mathcal{N}_{bulk}^e$ is violated, which causes accuracy to deteriorate significantly. This shows the significance of having a robust summation rule with appropriate choice of *PSAs* and partially explains the performance the node-based and cluster-based summation rules, as pointed out in [118]. Note that the sampling error for SR^B -1 and SR^B -2 is not zero since that the energy of edge atoms are assumed to follow the bulk energy distribution inside each element, as mentioned in Sub-section 2.3.2. This introduces some error across the element interface. In this case, only 0.3% and 0.69% extra errors are introduced in the respective displacement error norm and energy error norm, compared to the most accurate scheme (Scheme 0p*s) given by Figure 3.3d.

Table 3.1: Errors in the solution of the 1D non-local spring problem obtained via different summation rules and different choices of positions of primary sampling atoms with linear element.

Summation rules	Relative displacement errors			Relative energy errors		
	e_{disp}	e_{disp}^{sam}	e_{disp}^{disc}	e_E	e_E^{sam}	e_E^{disc}
Gauss1(SR ^B -1)	6.41%	0.31%	6.16%	24.96%	0.69%	24.95%
SR ^B -2	6.41%	0.31%	6.16%	24.96%	0.69%	24.95%
SR ^{naive}	11.25%	5.60%	6.16%	25.81%	6.59%	24.95%

For quadratic element, 8 different summation rules are employed as shown in Figure 3.4. Table 3.2 gives the results for the respective summation rule. Several interesting phenomena are observed: (I) high-order Gauss quadrature may give worse accuracy than low-order Gauss quadrature; for instance, “Gauss2” outperforms “Gauss3”; (II) “bisection” and “quartering” perform better than the corresponding Gauss quadrature rule that has the same number of quadrature points; (III) SR^B-1 and SR^B-2 again give the same and best results and the sampling errors are numerically zero; this observation validates SR^B and the claim that SR^B is independent of *PSA* positions as long as the selected primary sampling atom $i \in \mathcal{N}_{bulk}^e$, where \mathcal{N}_{bulk}^e is the index set of element bulk atoms (atoms in the dashed rectangle in Figure 2.3). Note that due to the discrete nature of atomistic modeling, the theoretical foundation for Gauss quadrature, which depends on continuum modeling and integral form, does not hold any more. Therefore, Gauss quadrature may not outperform other numerical techniques, which explains the first two observations above. In contrast, the proposed SR^B provides a theoretical foundation explaining the third observation. Note that SR^B can produce the same accuracy as the most accurate model

(Figure 3.4h) does with much less computation cost. The magnitude of the discretization errors indicates that the quadratic element can reproduce the quadratic deformation field exactly if there is no sampling error and thus is second-order consistent. It is worth to note that “Gauss3” and SR^B -1 share the same positions of *PSAs* and that the interior rep-atom is selected as a primary sampling atom in SR^B -1 and SR^B -2.

Table 3.2: Errors in the solution of the 1D non-local spring problem obtained via different summation rules and different choices of positions of primary sampling atoms with quadratic element.

Summation rules	Relative displacement errors			Relative energy errors		
	e_{disp}	e_{disp}^{sam}	e_{disp}^{disc}	e_E	e_E^{sam}	e_E^{disc}
Gauss1	41.78%	41.78%	5.91e-15	84.75%	84.75%	1.52e-14
Gauss2	3.75%	3.75%	5.91e-15	7.62%	7.62%	1.52e-14
Bisection	0.24%	0.24%	5.91e-15	0.49%	0.49%	1.52e-14
Gauss3	4.11%	4.11%	5.91e-15	8.35%	8.35%	1.52e-14
Gauss4	3.04%	3.04%	5.91e-15	7.00%	7.00%	1.52e-14
Quartering	3.56%	3.56%	5.91e-15	7.25%	7.25%	1.52e-14
SR^B -1	5.91e-15	0	5.91e-15	1.52e-14	0	1.52e-14
SR^B -2	5.91e-15	0	5.91e-15	1.52e-14	0	1.52e-14

For all the simulations in 1D, the discretization errors in displacement error norm are smaller than the discretization errors in energy error norm, which is consistent with the observation in FEM in continuum mechanics in that the accuracy in L_2 is generally better than that in H_1 .

3.4.2 2D non-homogeneous shear deformation

The 2D atomic model that is subjected to shear deformation consists of 49 by 49 atoms (2377 atoms in total) on a triangular lattice shown in Figure 3.5 and Figure 3.6. The harmonic spring potential with constant stiffness is employed here to describe the interatomic interaction. A zero-force spring length of $r_0 = 1$ is assumed for the first-nearest neighbor springs and of $\sqrt{3}r_0$ for the second-nearest neighbor springs. The parameters employed in the 1D case are also used here.

The non-homogeneous shear deformation employed in [66] to study the validity of CB rule is taken here to validate SR^B and make comparison with different summation rules. The deformation field is obtained by adding a quadratic term to the simple shear deformation field as follows:

$$\begin{bmatrix} x \\ y \end{bmatrix} = \begin{bmatrix} X+BY+AXY \\ Y \end{bmatrix} \quad (3.12)$$

where X and Y are reference coordinates in horizontal and vertical directions and x and y are the current coordinates. In the implementation, B is chosen to be 0.001 and A to be 1.5. For boundary conditions, the lower left corner is fixed in both horizontal and vertical directions and the lower right corner is fixed in horizontal direction.

For the linear triangle element (T3) in 2D, the function base for SR^B is unity and thus only one primary sampling atom is needed. For bilinear element (Q4), the function bases for SR^B are determined to be 1, x , y , xy , x^2 and y^2 , which is a complete second order base of polynomials in 2D. Interestingly, the quadratic triangle element T6 has the same function bases as Q4, as shown in Table 2.2. Thus 6 *PSAs* are needed for each Q4 and T6. Then the interpolant Φ_i in Eq. (2.16) is a complete quadratic polynomial. The MMM models with linear element (T3), bilinear element (Q4) and quadratic triangle element (T6) employing different summation rules are

shown in Figure 3.5, Figure 3.6, Figure 3.7, Figure 3.8, and Figure 3.9. Table 3.3 gives the results for linear element with “Gauss1” (SR^B -1) (Figure 3.5a), SR^B -2 (Figure 3.5b) and SR^{naive} (Figure 3.5c). As has been observed in the 1D case, SR^B -1 and SR^B -2 gives the same results while SR^{naive} has the worst accuracy out of the three rules. The sampling errors are not zero because of the employment of SR^B across the element edge. Extra errors of 0.49% and 0.75% are introduced in displacement and energy error norms with SR^B only with respect to the most accurate Scheme 0p*s, showing the robustness of SR^B . The discretization errors are due to the inability of linear element to reproduce a bilinear deformation field.

Table 3.3: Errors in the solution of the 2D non-local spring shear problem obtained via different summation rules and different choices of positions of primary sampling atoms with linear element.

Summation rules	Relative displacement errors			Relative energy errors		
	e_{disp}	e_{disp}^{sam}	e_{disp}^{disc}	e_E	e_E^{sam}	e_E^{disc}
Gauss1(SR^B -1)	27.14%	0.49%	26.81%	50.57%	0.75%	50.57%
SR^B -2	27.14%	0.49%	26.81%	50.57%	0.75%	50.57%
SR^{naive}	29.65%	12.46	26.81%	52.77%	14.87%	50.57%

For bilinear element, 7 different summation techniques are used, as shown respectively in Figure 3.6 and Figure 3.7. As shown in Table 3.4, “Gauss 2” (Figure 3.6a) and “Gauss 3” (Figure 3.6b) generate comparable accuracy and outperform “Gauss1”. Note that in continuum mechanics, “Gauss2” is required for the exact integration for bilinear element. “Bisection” (Figure 3.6c) gives less accurate results compared to “Gauss2”. Interestingly, “Trisection” performs better than “Gauss3”. The justification used in the 1D can also be employed here. In contrast, SR^B -1 and SR^B -2 outperform all the other summation rules. Note that 6 and 9 *PSAs* are

used in SR^B and “Gauss3”, respectively. Thus, SR^B is more accurate and efficient when compared to “Gauss3”. SR^B -1 and SR^B -2 produce almost the same results and the sampling error is negligible, which again validates SR^B and shows the effectiveness of SR^B . The slight difference and small sampling errors may be due to round-off errors. The magnitude of discretization errors indicates the ability of bilinear element (Q4) in reproducing the bilinear deformation field.

Table 3.4: Errors in the solution of the 2D non-local spring shear problem obtained via different summation rules and different choices of positions of primary sampling atoms with bilinear element Q4.

Summation rules	Relative displacement errors			Relative energy errors		
	e_{disp}	e_{disp}^{sam}	e_{disp}^{disc}	e_E	e_E^{sam}	e_E^{disc}
Gauss1	25.83%	25.83%	2.51e-14	39.14%	39.14%	8.92e-14
Gauss2	2.35%	2.35%	2.51e-14	3.43%	3.43%	8.92e-14
Bisection	3.05%	3.05%	2.51e-14	4.50%	4.50%	8.92e-14
Gauss3	2.12%	2.12%	2.51e-14	3.08%	3.08%	8.92e-14
Trisection	0.80%	0.80%	2.51e-14	0.63%	0.63%	8.92e-14
SR^B -1	1.60e-14	1.02e-14	2.51e-14	8.75e-14	7.07e-14	8.92e-14
SR^B -2	2.61e-14	1.93e-15	2.51e-14	8.78e-14	4.61e-14	8.92e-14

For quadratic triangular element (T6), 7 different summation rules are employed and respectively shown in Figure 3.8 and Figure 3.9. As shown in Table 3.5, “Gauss 4” and “Gauss 5” give less accurate results compared to “Gauss3”. As has been observed with bilinear element, SR^B -1 and SR^B -2 outperforms Gauss quadrature. Note that “Gauss 4” and SR^B -1 have the same selection of the 6 selected *PSAs* and “Gauss 5” employs 7 *PSAs*, which shows the robustness of SR^B . The same results from SR^B -1 and SR^B -2 verify the proposed SR^B . Since there is an interface

between the two employed T6 elements, an extra error of 0.89% and 1.41% are introduced in the respective displacement and energy error norm.

As observed in the 1D case, the accuracy in displacement field is also better than that in energy field in 2D.

Table 3.5: Errors in the solution of the 2D non-local spring shear problem obtained via different summation rules and different choices of positions of primary sampling atoms with quadratic triangle element T6.

Summation rules	Relative displacement errors			Relative energy errors		
	e_{disp}	e_{disp}^{sam}	e_{disp}^{disc}	e_E	e_E^{sam}	e_E^{disc}
Gauss1	31.64%	31.64%	2.21e-14	76.80%	76.80%	9.13e-14
Gauss2	3.00%	3.00%	2.21e-14	7.37%	7.37%	9.13e-14
Gauss3	2.53%	2.53%	2.21e-14	7.78%	7.78%	9.13e-14
Gauss4	3.30%	3.30%	2.21e-14	9.14%	9.14%	9.13e-14
Gauss5	2.61%	2.61%	2.21e-14	7.34%	7.34%	9.13e-14
SR ^B -1	0.89%	0.89%	2.21e-14	1.41%	1.41%	9.13e-14
SR ^B -2	0.89%	0.89%	2.21e-14	1.41%	1.41%	9.13e-14

3.5 SR^B EXTENSION AND VALIDATION FOR LENNARD-JONES POTENTIAL

In general, interatomic potentials employed in atomistic simulations are non-convex and the atom-wise stiffness (i.e. the negative second derivative of the interatomic potential with respect to atomic positions) is not constant. Since the SR^B is derived for the nonlocal harmonic spring model, the performance of MMM with SR^B for non-convex potentials has to be tested. In this section, MMM with SR^B will be extended and validated for the standard Lennard-Jones (LJ) potential, i.e. $U_{LJ}=4\epsilon[(\sigma/r)^{12}-(\sigma/r)^6]$, where r is the interatomic distance with the initial value

$r_0=2^{1/6}$ and potential parameters $\sigma=\epsilon=1$. The first and second nearest neighbor interactions are taken to describe the interaction between atoms. MMM models employing linear (T3), bilinear (Q4) and quadratic triangle (T6) elements with SR^B and other summation rules will be tested by the numerical examples as used for the spring potentials in Section 3.4. Note that for MMM models with different summation rules, the function bases of SR^B for different elements are the same as in the corresponding spring case. The only difference is that the LJ potential is used instead of the spring potential.

3.5.1 1D quadratic tensile deformation

The same atomic chain and boundary condition used in the previous spring case is employed here except that LJ potential is taken to describe the interatomic interaction. The same deformation field in the corresponding spring case scaled by a factor $\alpha = 3.07e-5$ is used to give the quadratic deformation field.

Linear elements with “Gauss1” (SR^B -1), SR^B -2 and SR^{naive} are shown in Figure 3.3a, Figure 3.3b and Figure 3.3c, respectively. The results with the respective summation rule are shown in Table 3.6. Interestingly, SR^B -1 and SR^B -2 produce the same results; although there is a difference in the 10th digit after the decimal point, SR^B is still valid. The sampling errors with SR^B -1 and SR^B -2 are due to the employment of SR^B across the element interface. The magnitude of the sampling errors indicates that SR^B is accurate even across linear element edges. In contrast, SR^{naive} introduces large sampling errors and lose significant accuracy as observed and explained in the corresponding spring case, which again demonstrates the importance of the right selection of *PSA* positions for anharmonic potentials.

Table 3.6: Errors in the solution of the 1D non-local LJ problem obtained via different summation rules and different choices of positions of primary sampling atoms with linear element.

Summation rules	Relative displacement errors			Relative energy errors		
	e_{disp}	e_{disp}^{sam}	e_{disp}^{disc}	e_E	e_E^{sam}	e_E^{disc}
Gauss1(SR ^B -1)	6.18%	0.01%	6.19%	27.20%	0.03%	27.20%
SR ^B -2	6.18%	0.01%	6.19%	27.20%	0.03%	27.20%
SR ^{naive}	42.81%	37.76%	6.19%	91.14%	91.44%	27.20%

Figure 3.4 shows the primary sampling atom selections of the respective summation rule for the employed quadratic element, as used in the spring case. In addition, the standard Cauchy-Born (CB) rule is also employed in the comparison. Since the deformation gradient is no longer constant for quadratic elements, the deformation gradient at a Gauss quadrature point is employed when reconstructing the deformed crystal cell structure underneath. Different orders of Gauss quadrature have been implemented with CB rule to consider the effect of non-constant deformation gradient. The “#” in “CB#” means the number of Gauss quadrature points employed in the CB rule. To perform the error decomposition for CB rule, after the displacements at the element nodes have been determined, they are interpolated to determine the displacements of the ghost atoms such that the errors defined in Section 3.2 can be calculated.

The phenomena observed in the corresponding spring case are also seen here in Table 3.7. For instance, “Gauss4” has significant errors and the sampling errors from SR^B-1 and SR^B-2 are the same up to the 7th decimal point. Note that in the corresponding spring case, the sampling errors are the same and numerically zero to the computer precision. The difference is due to that SR^B is exact for the spring model and is an accurate and efficient approximation for the LJ potential. The standard CB rule produces less accurate results when compared to other

summation rules and “CB4” performs worse than “CB2” and “CB3”. The inaccuracy of the standard CB rule may be due mainly to the inaccurate description of non-homogenous deformations.

Based on the observations from both linear and quadratic elements in 1D for the LJ case, it is safe to say that the position of $PSAs$ may not affect the accuracy of SR^B significantly as long as the selected $PSAs$ belongs to \mathcal{N}_{bulk}^e , though there is a slightly difference between SR^B -1 and SR^B -2.

Table 3.7: Errors in the solution of the 1D non-local LJ problem obtained via different summation rules and different choices of positions of primary sampling atoms with quadratic element.

Summation rules	Relative displacement errors			Relative energy errors		
	e_{disp}	e_{disp}^{sam}	e_{disp}^{disc}	e_E	e_E^{sam}	e_E^{disc}
Gauss1	37.05%	37.05%	1.04e-13	75.88%	75.88%	3.59e-12
Gauss2	3.62%	3.62%	1.04e-13	7.41%	7.41%	3.59e-12
CB2	11.88%	11.88%	1.04e-13	14.09%	14.09%	3.59e-12
Bisection	0.23%	0.23%	1.04e-13	0.48%	0.48%	3.59e-12
Gauss3	3.97%	3.97%	1.04e-13	8.13%	8.13%	3.59e-12
CB3	11.89%	11.89%	1.04e-13	14.09%	14.09%	3.59e-12
Gauss4	21.22%	21.22%	1.04e-13	29.46%	29.46%	3.59e-12
CB4	21.85%	21.85%	1.04e-13	43.91%	43.91%	3.59e-12
Quartering	3.45%	3.45%	1.04e-13	7.06%	7.06%	3.59e-12
SR^B -1	3.90e-7	3.90e-7	1.04e-13	7.96e-7	7.96e-7	3.59e-12
SR^B -2	5.01e-7	5.01e-7	1.04e-13	1.02e-6	1.02e-6	3.59e-12

3.5.2 2D non-homogeneous shear deformation

The same 2D atomic sheet with the same boundary conditions and non-homogeneous shear deformation used in the spring case are employed for the LJ potential.

“Gauss1” (SR^B -1), SR^B -2 and SR^{naive} for the linear element are shown in Figure 3.5a, Figure 3.5b and Figure 3.5d, respectively. Table 3.8 shows the results from the respective summation rule. Again, as observed in the corresponding 2D spring case and the 1D LJ model, the sampling errors from SR^B -1 and SR^B -2 are the same up to the 12th decimal point and the discretization errors dominate the sampling errors.

Table 3.8: Errors in the solution of the 2D LJ shear problem obtained via different summation rules and different choices of positions of primary sampling atoms with linear element.

Summation rules	Relative displacement errors			Relative energy errors		
	e_{disp}	e_{disp}^{sam}	e_{disp}^{disc}	e_E	e_E^{sam}	e_E^{disc}
Gauss1(SR^B -1)	41.22%	0.55%	41.06%	56.28%	1.00%	56.30%
SR^B -2	41.22%	0.55%	41.06%	56.28%	1.00%	56.30%
SR^{naive}	41.36%	0.78%	41.06%	56.35%	1.43%	56.30%

For bilinear element (Q4), the primary sampling atom selections of the corresponding summation rules are also demonstrated in Figure 3.6 and Figure 3.7. As in the corresponding spring case, similar pattern in accuracy among the different summation rules are observed in Table 3.9. Note that due to the approximation property of SR^B for non-convex potentials, the difference between SR^B -1 and SR^B -2 is clearly observed. However, the difference is still relatively small (i.e. only 2.53% in displacement error norm). It is worth to note that SR^B even

outperforms “Gauss3” with less *PSAs*, which again shows the robustness of SR^{B} over Gauss quadrature.

Table 3.9: Errors in the solution of the 2D LJ shear problem obtained via different summation rules and different choices of positions of primary sampling atoms with bilinear element Q4.

Summation rules	Relative displacement errors			Relative energy errors		
	e_{disp}	$e_{\text{disp}}^{\text{sam}}$	$e_{\text{disp}}^{\text{disc}}$	e_E	e_E^{sam}	e_E^{disc}
Gauss1	40.51%	40.51%	1.58e-12	52.57%	52.57%	2.39e-12
Gauss2	3.18%	3.18%	1.58e-12	3.90%	3.90%	2.39e-12
Bisection	3.63%	3.63%	1.58e-12	5.49%	5.49%	2.39e-12
Gauss3	3.08%	3.08%	1.58e-12	3.79%	3.79%	2.39e-12
Trisection	1.18%	1.18%	1.58e-12	1.12%	1.12%	2.39e-12
$\text{SR}^{\text{B}}\text{-1}$	0.77%	0.77%	1.58e-12	1.19%	1.19%	2.39e-12
$\text{SR}^{\text{B}}\text{-2}$	0.79%	0.79%	1.58e-12	1.08%	1.08%	2.39e-12

For quadratic triangle element (T6), Figure 3.8 and Figure 3.9 show primary sampling atom selections of the 7 different summation rules employed, respectively. In Table 3.10, as has been observed before, $\text{SR}^{\text{B}}\text{-1}$ and $\text{SR}^{\text{B}}\text{-2}$ outperform all the other summation rules and the advantage is more significant when examining the energy errors. Note that “Gauss4” and $\text{SR}^{\text{B}}\text{-1}$ have the same *PSAs* selection and “Gauss5” employs 7 quadrature atoms.

Table 3.10: Errors in the solution of the 2D non-local LJ shear problem obtained via different summation rules and different choices of positions of primary sampling atoms with quadratic triangle element T6.

Summation rules	Relative displacement errors			Relative energy errors		
	e_{disp}	e_{disp}^{sam}	e_{disp}^{disc}	e_E	e_E^{sam}	e_E^{disc}
Gauss1	66.03%	66.03%	6.62e-11	84.94%	84.94%	1.13e-10
Gauss2	4.20%	4.20%	6.62e-11	12.66%	12.66%	1.13e-10
Gauss3	3.66%	3.66%	6.62e-11	12.22%	12.22%	1.13e-10
Gauss4	5.45%	5.45%	6.62e-11	16.32%	16.32%	1.13e-10
Gauss5	3.98%	3.98%	6.62e-11	12.30%	12.30%	1.13e-10
SR ^B -1	1.14%	1.14%	6.62e-11	2.35%	2.35%	1.13e-10
SR ^B -2	1.26%	1.26%	6.62e-11	2.22%	2.22%	1.13e-10

The simulations employing the LJ potential show that SR^B is still accurate and outperforms Gauss quadrature and other summation rules. As long as the selected *PSAs* belong to \mathcal{N}_{bulk}^e , the different choices of *PSAs* in SR^B may not affect the accuracy dramatically. As expected, the errors in energy error norm are relatively larger compared to those in displacement error norm. Compared to the corresponding spring models, the error is relatively larger when the LJ model is employed.

3.6 COMPARISON OF INTERFACE COMPATIBILITY

In this section, the interface compatibility of MMM and some existing methods are compared through some 1D benchmark problems devised by Curtin and Miller in an excellent review paper about multiscale method development [54].

The original QC method [9], CLS approach [12], QC-GFC scheme [11], FEAt method [8], CADD approach [14, 20], and MMM are applied to solve these benchmark problems and

compared against full atomistics. The model utilized for these problems consists of 101 atoms positioned as $r_i = ia$, $i = 0-100$. The concurrent coupling model is with the interface at $i = 50$, the region from the left end to the interface is the atomistic region and that from $i = 50$ to $i = 100$ is the continuum region or coarse-grained region for all the multiscale methods. It is worth to point out that a uniform mesh with the size reduced to the atomistic distance is adopted for the QC, CLS, QC-GFC, FEAt and CADD models in the continuum region. In contrast, a uniform mesh with size $= 25a$ (Figure 3.10a) is used in the coarse-grained area in MMM. Three loading conditions including uniform deformation, non-uniform deformation, and single point force are considered. The left end is fixed and the right end is subject to a unit load for all the loading conditions.

For the uniform deformation condition, Figure 3.10b demonstrates the local strain $(u_i - u_{i-1})/a$ between neighboring atoms or nodes near the interface of the full atomistic model as well as all the multiscale models. In Figure 3.10b, as pointed out in [54], unphysical deformations of the atoms/nodes in the transition region arise in QC/CLS models due to the existence of ghost forces. The results of CADD are qualitatively similar, but quantitatively different from that of the QC/CLS model. In contrast, the QC-GFC, FEAt and MMM models show perfect agreement of strain distribution in full atomistics. Note that the uniform deformation assumption in both the CB rule and energy-sampling scheme is satisfied in this loading condition. However, the QC method needs further computation to correct the ghost force. In contrast, MMM directly gives accurate solution without any heuristic modification.

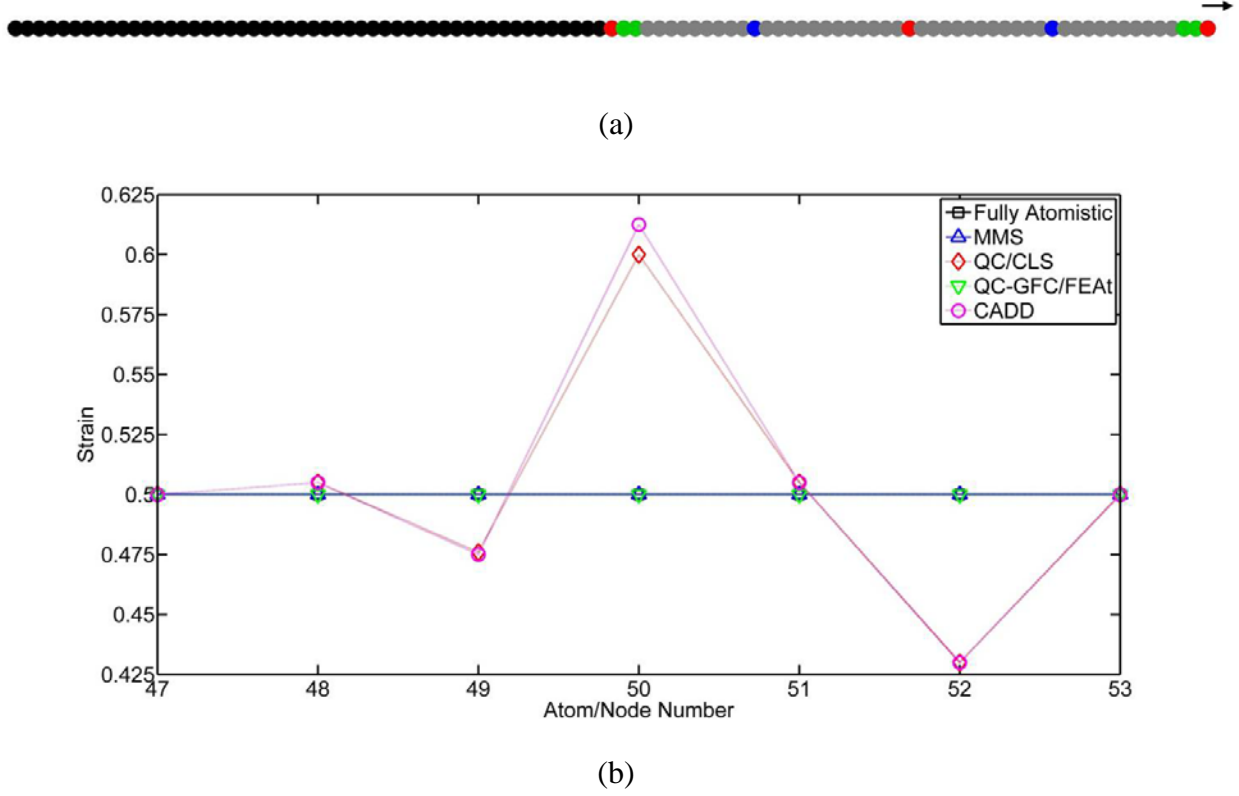


Figure 3.10: Comparison between full atomistics, MMM and several other multiscale methods for the 1D non-local spring model under uniform deformation: MMM model (a), strain distribution of different methods near the interface (b)

For inhomogeneous deformation, additional forces of magnitude $f = 0.1$ are applied to atoms/nodes $i-2, i-1, i, i+1, i+2$ with $i=50$ across the transition region while the unit force applied on the right end is maintained. Figure 3.11b shows the deformation of each method. In this loading condition, there is presence of inhomogeneous deformation. Thus, the basic uniform deformation does not hold, and none of the presented methods reproduce the exact results. However, the same trends in Figure 3.10b are also observed in Figure 3.11b. The QC-GFC, FEAt and MMM models still agree well with full atomistics.

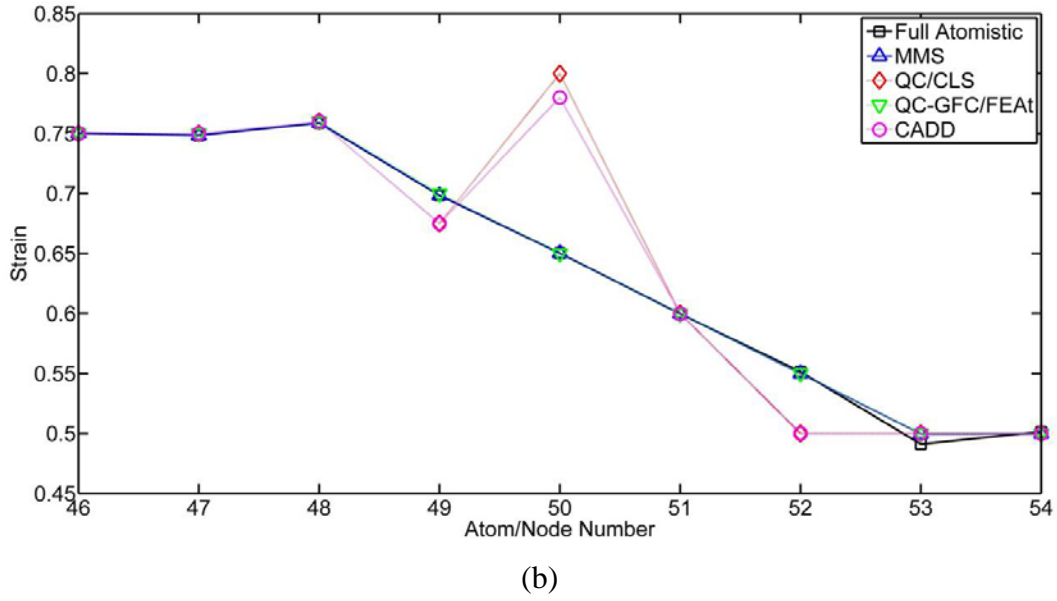
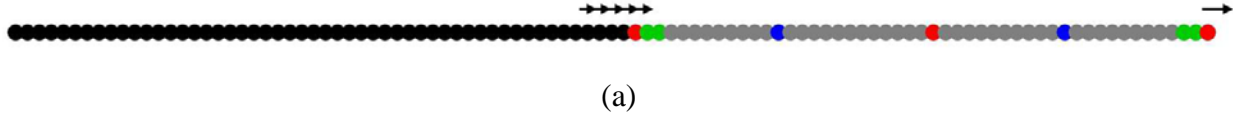


Figure 3.11: Comparison between full atomistics, MMM and several other multiscale methods for the 1D non-local spring model under inhomogeneous deformation: MMM model (a), strain distribution of different methods near the interface (b)

For the third loading condition, a single point force of magnitude $f = 1$ is applied to the atom or node at the interface while maintaining the overall applied unit force at the right end. The deformation distributions of each method are shown in Figure 3.12b. The QC-GFC and FEAt behaves differently from their performance in the former two loading cases. As mentioned in [54], because the errors caused by each of the individual point forces cancel each other, the QC-GFC and FEAt present reasonable results in the case of inhomogeneous deformation. However, a long-range error under the interface point force is introduced in QC-GFC and FEAt

because no strict requirement of self-equilibrium of the local forces in the QC-GFC and FEAt models. Their discontinuity in treatment of the atoms and nodes leads to unbalanced forces that are then balanced by long-range forces. In contrast, MMM still agrees quite well with full atomistics even with the coarse mesh employed in the continuum region.

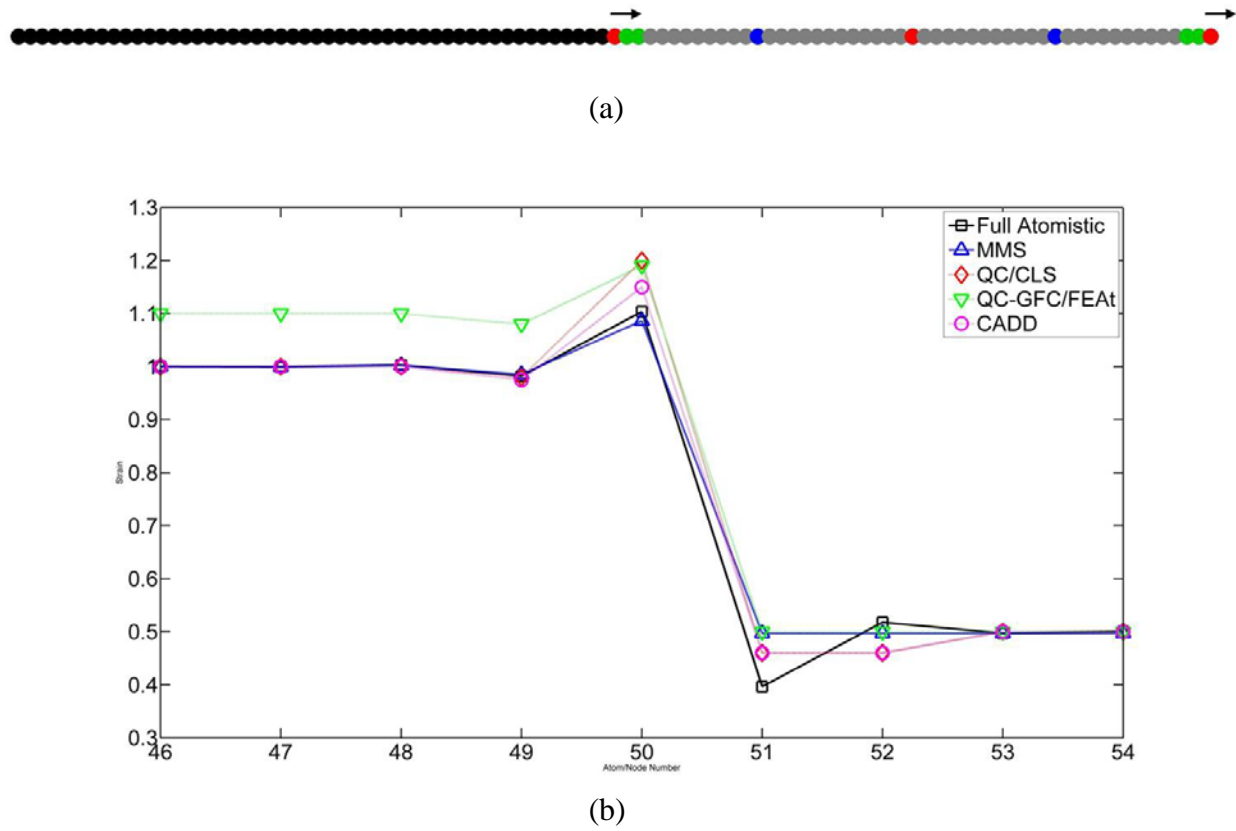


Figure 3.12: Comparison between full atomistics, MMM and several other multiscale methods for the 1D non-local spring model under point force at interface: MMM model (a), strain distribution of different methods near the interface (b)

In summary, the QC-GFC and FEAt approaches show excellent results under uniform deformation but introduce long-range errors under sharp deformation gradients. The QC, CLS and CADD methods do not cause errors in the long-range fields in the presence of deformation gradients but show a permanent distortion near the interface. In contrast, MMM demonstrates good agreement with full atomistics in all three loading cases.

3.7 SOME APPLICATIONS

In this section, 2D atomic LJ models undergoing high-order tensile, shear and bending deformations are employed to test the robustness of MMM by employing more element interfaces with SR^B only and with other numerical integration techniques. A crack propagation problem is also employed to show the ability of MMM to capture material defects locally.

3.7.1 2D atomic sheet tensile model

The 2D atomic LJ sheet employed in Section 3.5 is considered. The applied tensile deformation is given as follows:

$$u_x = \alpha[-(L - x)^2 + L^2] \quad (3.13a)$$

$$u_y = -\gamma\alpha y(L - x) \quad (3.14b)$$

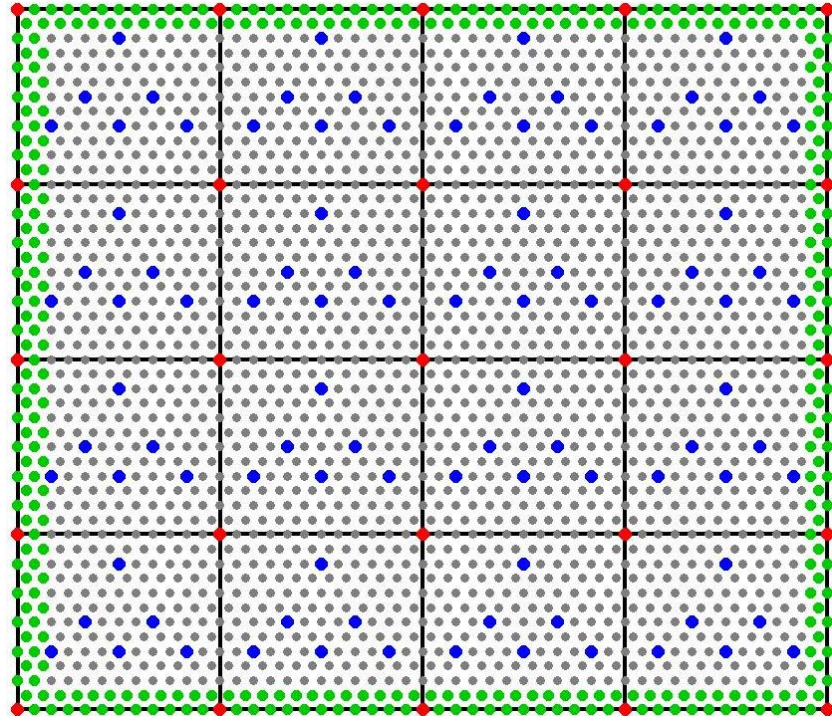
In the implementation, $\alpha = 5e^{-4}$ and $\gamma = 0.3$ are employed. The displacement field is motivated by a 2D continuum model which has a quadratic deformation in x direction under a tensile loading. The displacement in y direction is determined by Poisson effect with γ being the Poisson ratio. The atomic sheet is fixed at the middle point of the left end in x and y directions

and at the left bottom corner in x direction to eliminate rigid body motion. Bilinear element Q4 and quadratic triangle element T6 are employed with $h_x = 12r_0$ and $h_y = 6\sqrt{3} r_0$.

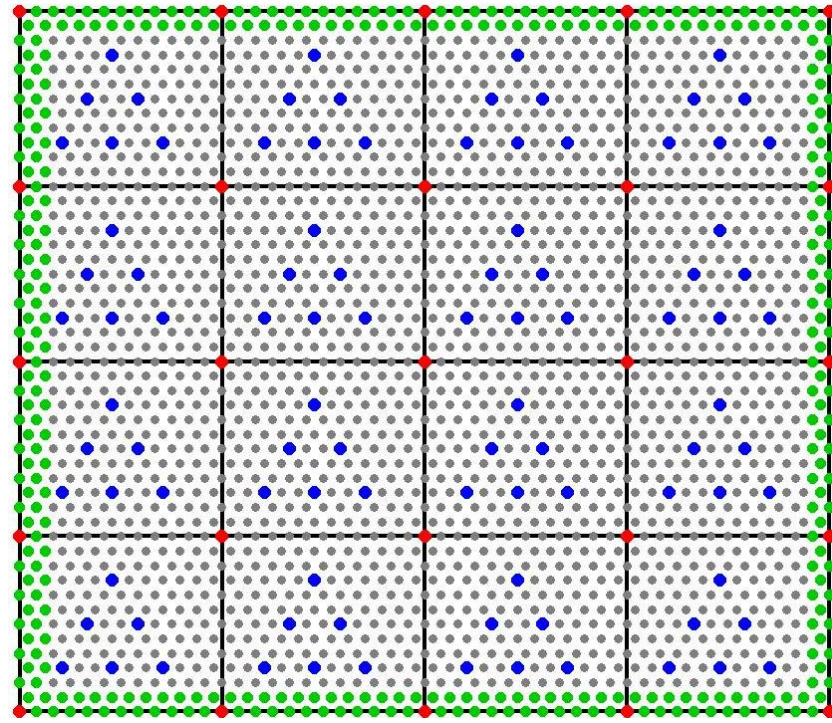
Seven different summation rules employed before are used here for bilinear element. Figure 3.13 shows the selection of *PSAs* for SR^B -1 and SR^B -2. As can be seen from Table 3.11, SR^B -1 and SR^B -2 outperforms the other summation rules. The results from SR^B -1 and SR^B -2 are identical up to the 6th decimal digit, which is similar to what has been observed in Section 3.5.

Table 3.11: Errors in the solution of the 2D LJ tensile problem obtained via different summation rules and different choices of positions of primary sampling atoms with bilinear element Q4.

Summation rules	Relative displacement errors			Relative energy errors		
	e_{disp}	e_{disp}^{sam}	e_{disp}^{disc}	e_E	e_E^{sam}	e_E^{disc}
Gauss1	8.79%	6.91%	2.45%	18.83%	14.24%	11.81%
Gauss2	8.48%	6.73%	2.45%	18.15%	12.94%	11.81%
Bisection	7.42%	5.68%	2.45%	16.90%	11.97%	11.81%
Gauss3	8.40%	6.58%	2.45%	17.82%	12.44%	11.81%
Trisection	8.44%	6.69%	2.45%	18.10%	12.90%	11.81%
SR^B -1	4.56%	2.25%	2.45%	13.07%	4.25%	11.81%
SR^B -2	4.56%	2.25%	2.45%	13.07%	4.25%	11.81%



(a)



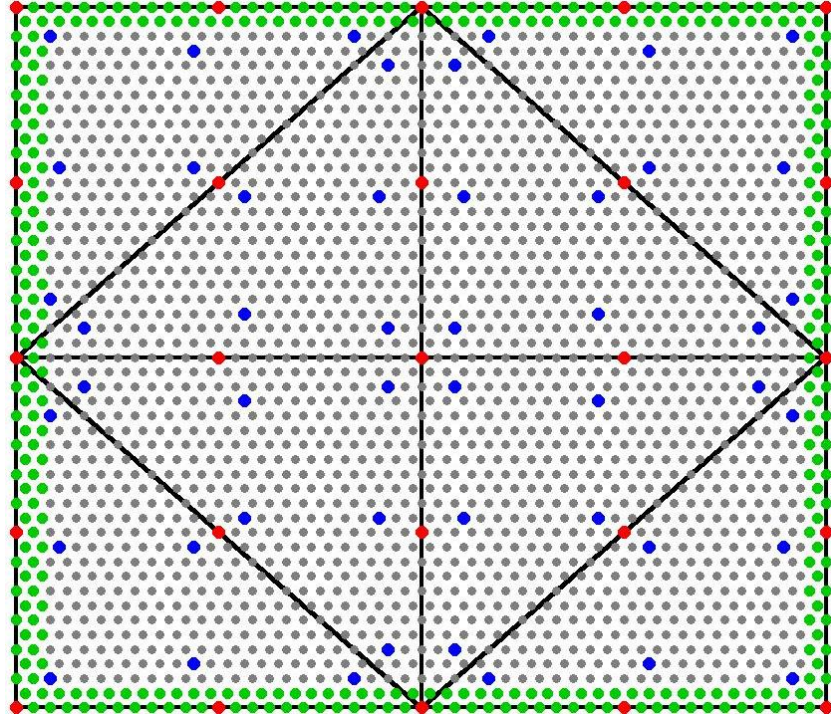
(b)

Figure 3.13: Schematic illustrations of primary sampling atom selections for the MMM models with bilinear element (Q4) and summation rules SR^B-1 (a) and SR^B-2 (b).

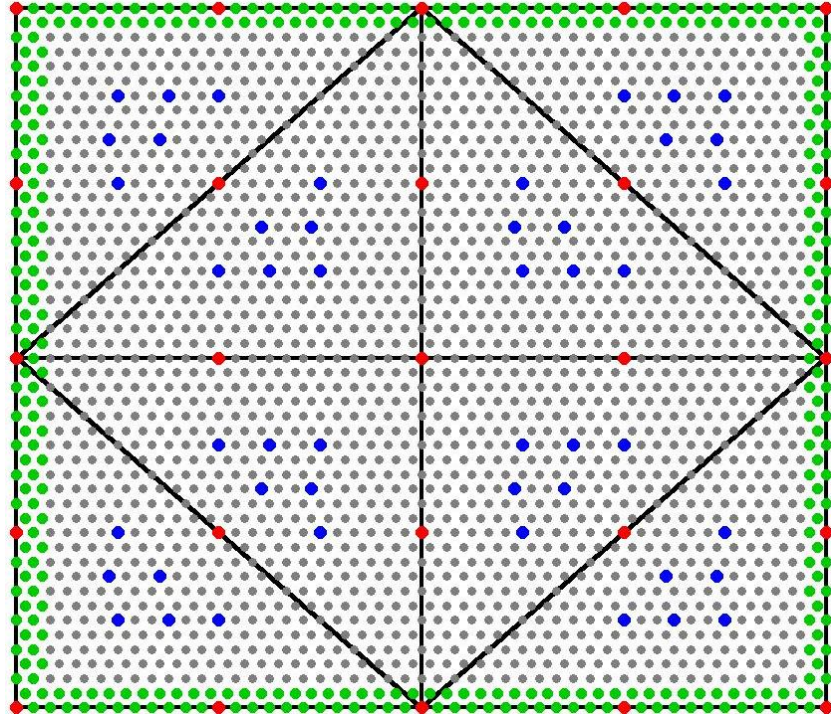
For quadratic triangle element T6, 5 different orders of Gauss quadrature rules are used and compared with SR^B . Figure 3.14 demonstrates the *PSAs* selections of the two SR^B rules employed. Note that “Gauss4” and SR^B -1 share the same *PSA* selection. As shown in Table 3.12, SR^B -1 and SR^B -2 produce much better accuracy than Gauss quadrature. The merit of employing the SR^B can be clearly observed from the distribution of errors in energy error norm. As expected, the difference between SR^B -1 and SR^B -2 is observed due to the different selection of *PSAs*. Again, the difference is relatively small (1.39% in displacement error norm and 0.8% in energy error norm).

Table 3.12: Errors in the solution of the 2D LJ tensile problem obtained via different summation rules and different choices of positions of primary sampling atoms with quadratic triangle element T6.

Summation rules	Relative displacement errors			Relative energy errors		
	e_{disp}	e_{disp}^{sam}	e_{disp}^{disc}	e_E	e_E^{sam}	e_E^{disc}
Gauss1	37.25%	37.25%	2.09e-10	107.56%	107.56%	4.26e-10
Gauss2	8.77%	8.77%	2.09e-10	23.30%	23.30%	4.26e-10
Gauss3	8.80%	8.80%	2.09e-10	23.23%	23.23%	4.26e-10
Gauss4	8.34%	8.34%	2.09e-10	21.88%	21.88%	4.26e-10
Gauss5	6.89%	6.89%	2.09e-10	19.84%	19.84%	4.26e-10
SR^B -1	2.16%	2.16%	2.09e-10	6.28%	6.28%	4.26e-10
SR^B -2	2.13%	2.13%	2.09e-10	6.33%	6.33%	4.26e-10



(a)



(b)

Figure 3.14: Schematic illustrations of primary sampling atom selections for the MMM models with quadratic triangle element (T6) and summation rules $\text{SR}^{\text{B}}\text{-1}$ (a) and $\text{SR}^{\text{B}}\text{-2}$ (b).

3.7.2 2D atomic sheet shear model

The shear deformation considered in Section 3.5 employs a bilinear deformation term such that the bilinear element Q4 and quadratic triangle element T6 both can exactly reproduce the bilinear shear. The shear deformation considered here employs a biquadratic term such that none of Q4 and T6 can regenerate it, and hence there will be discretization errors for both Q4 and T6. The shear deformation is given as:

$$\begin{bmatrix} x \\ y \end{bmatrix} = \begin{bmatrix} X + AX^2Y^2 \\ Y \end{bmatrix}$$

where A is taken to be $1e-7$ in the numerical implementation. The same atomic sheet with the same boundary conditions as used in the case of bilinear shear deformation is also employed here. Different summation rules used in the above tensile deformation case are also taken here for both bilinear element and quadratic element.

The selection of *PSAs* for SR^B -1 and SR^B -2 are shown in Figure 3.13 and Figure 3.14 for bilinear and triangle elements, respectively. As shown in Table 3.13 and Table 3.14, similar trends observed previously are shown again here for both bilinear element and quadratic triangle element. Again, SR^B produces the best accuracy.

Table 3.13: Errors in the solution of the 2D LJ shear problem obtained via different summation rules and different choices of positions of primary sampling atoms with bilinear element Q4.

Summation rules	Relative displacement errors			Relative energy errors		
	e_{disp}	e_{disp}^{sam}	e_{disp}^{disc}	e_E	e_E^{sam}	e_E^{disc}
Gauss1	27.99%	23.49%	6.74%	23.61%	20.52%	12.81%
Gauss2	23.38%	18.86%	6.74%	18.38%	13.14%	12.81%
Bisection	41.69%	36.19%	6.74%	21.77%	16.17%	12.81%
Gauss3	19.51%	15.03%	6.74%	16.76%	10.75%	12.81%
Trisection	23.61%	19.09%	6.74%	18.43%	13.20%	12.81%
SR ^B -1	3.84%	3.66%	6.74%	13.89%	6.07%	12.81%
SR ^B -2	3.84%	3.67%	6.74%	13.90%	6.08%	12.81%

Table 3.14: Errors in the solution of the 2D LJ shear problem obtained via different summation rules and different choices of positions of primary sampling atoms with quadratic triangle element T6.

Summation rules	Relative displacement errors			Relative energy errors		
	e_{disp}	e_{disp}^{sam}	e_{disp}^{disc}	e_E	e_E^{sam}	e_E^{disc}
Gauss1	80.47%	79.97%	2.61%	174.16%	173.87%	7.65%
Gauss2	15.86%	14.75%	2.61%	22.61%	21.60%	7.65%
Gauss3	15.16%	14.01%	2.61%	22.40%	20.87%	7.65%
Gauss4	14.31%	13.31%	2.61%	19.86%	18.35%	7.65%
Gauss5	14.93%	13.87%	2.61%	21.99%	20.36%	7.65%
SR ^B -1	3.75%	2.87%	2.61%	12.03%	9.39%	7.65%
SR ^B -2	3.77%	2.79%	2.61%	12.09%	9.56%	7.65%

3.7.3 2D atomic beam bending model

The 2D atomic beam model consists of 97 by 25 atoms (2,413 atoms in total), placed on a triangular lattice as used in Ref. [61]. The displacement field is as follows:

$$u(X, Y) = -\frac{P}{6EI} \left[(6L - 3X)Y + (2 + \nu) \left(Y^2 - \frac{D^2}{4} \right) \right] \quad (3.15a)$$

$$v(X, Y) = -\frac{P}{6EI} \left[3vY^2(L - X) + (4 + 5v) \frac{D^2X}{4} + (3L - X)X^2 \right] \quad (3.16b)$$

where L and D are the length and height of the beam, respectively. The motivation of employing such a deformation field is from the commonly used continuum beam bending problem in Refs. [123, 124] to study the behavior of FEM and meshfree methods. In this study, with the parameters $P=1000$, $E=3 \times 10^5$, $\nu=0.3$ and $I=\frac{D^3}{12}$, the atomic beam is fixed at the left lower and upper corners in x direction and at the middle of the left edge in y direction. Linear triangle element T3 and quadratic element T6 are employed here with SR^B and other summation rules. The primary sampling atom selections for SR^B -1 and SR^B -2 are the same as used in Section 3.5.

Table 3.15 and Table 3.16 show the results of different summation rules employed for both T3 and T6 elements, respectively. Again, SR^B-1 and SR^B-2 generate almost the same results for linear element T3 and the difference is clearer for quadratic element T6. As expected, SR^B gives better accuracy compared to other summation rules and the advantage is significant in the energy error norm. Since the energy error norm defined in Eq. (3.5) actually measures the accuracy of the relative positions of the atoms in the final configuration and thus reflects the performance of representing the final microstructure, the merit of utilizing SR^B in energy error norm may be significant.

Table 3.15: Errors in the solution of the 2D LJ beam bending problem obtained via different summation rules and different choices of positions of primary sampling atoms with linear element T3

Summation rules	Relative displacement errors			Relative energy errors		
	e_{disp}	e_{disp}^{sam}	e_{disp}^{disc}	e_E	e_E^{sam}	e_E^{disc}
Gauss1(SR ^B -1)	7.80%	0.87%	7.05%	17.32%	5.90%	14.99%
SR ^B -2	7.80%	0.87%	7.05%	17.32%	5.90%	14.99%

Table 3.16: Errors in the solution of the 2D LJ beam bending problem obtained via different summation rules and different choices of positions of primary sampling atoms with quadratic triangle element T6

Summation rules	Relative displacement errors			Relative energy errors		
	e_{disp}	e_{disp}^{sam}	e_{disp}^{disc}	e_E	e_E^{sam}	e_E^{disc}
Gauss1	14.24%	14.54%	0.80%	83.92%	84.00%	2.63%
Gauss2	3.22%	3.75%	0.80%	17.31%	17.33%	2.63%
Gauss3	3.32%	2.76%	0.80%	12.37%	12.09%	2.63%
Gauss4	1.96%	2.40%	0.80%	12.35%	12.27%	2.63%
Gauss5	4.15%	4.71%	0.80%	21.05%	21.10%	2.63%
SR ^B -1	1.03%	0.41%	0.80%	3.66%	2.54%	2.63%
SR ^B -2	0.92%	0.37%	0.80%	3.68%	2.60%	2.63%

3.7.4 2D crack propagation

A 2D crack problem is solved by full atomistics and two MMM models shown in Figure 3.15b and Figure 3.16b. In the simulation, LJ potential with parameters equal to unity and a cutoff distance of 2.3 in LJ units is employed. The model consists of 1057 atoms with an initial spacing $r_0=2^{1/6}\sigma$ and has a notch placed in the middle of the rectangular model and oriented perpendicular to the applied displacement loading on the ends (Figure 3.15a and Figure 3.16a). Two layers of

atoms located on the left and right ends of the model are initially fixed for static relaxation, followed by displacement load application.

The simulation is composed of several steps. Prior to each step, incremental tensile displacement loading of 0.002 distance units is applied to the ends in opposite directions. Stress is then calculated at the end of each step by taking the average of the forces of the boundary atoms. The simulation is run successively until the models fracture into two distinct parts along the middle. Collecting data from each step, the stress-strain curve is obtained.

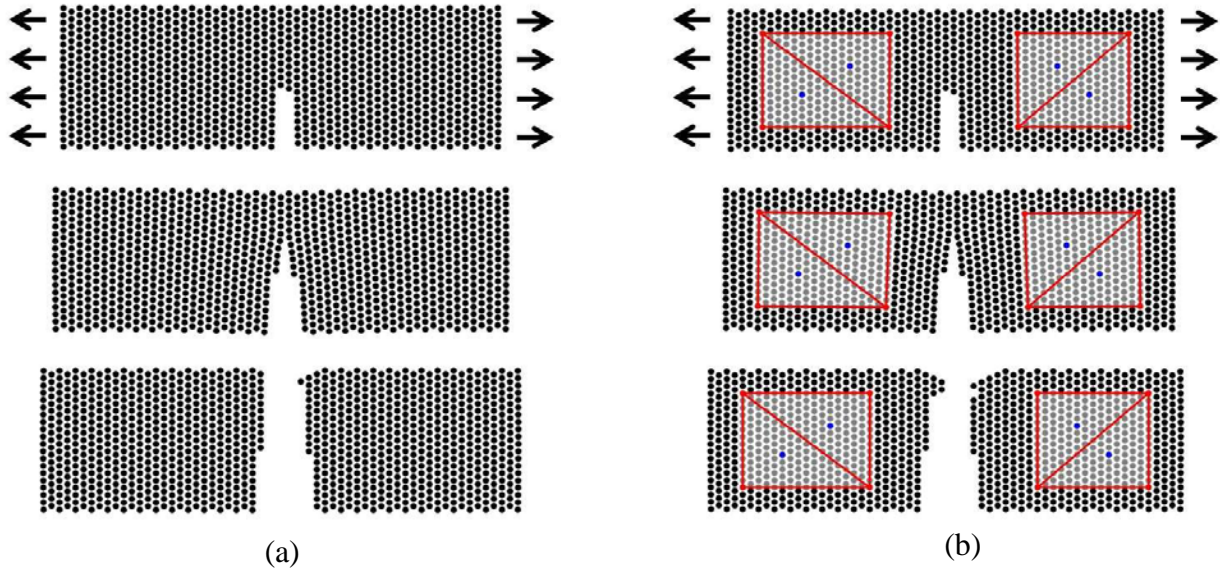


Figure 3.15: Snapshots from crack propagation of full atomistic (left) and MMM model I (right) simulations

In both models employed in the MMM simulations (Figure 3.15b and Figure 3.16b), 4 interpolating rep-atoms (0.75% of the total number of atoms) arranged in the shape of a rectangle are selected on each side of the notch. A triangular mesh with 4 elements is created using these

rep-atoms and its size is $14r_0$ in x direction and $13r_0$ in y direction. The atoms in the middle of each element are set to be primary sampling atoms (0.38%). 4 layers of atoms from the surfaces, 6 layers of atoms from the notch are modeled as non-interpolating rep atoms (63%). Rest of the atoms is designated as non-sampling atoms (28% in Figure 3.15b and 23% in Figure 3.16b). The difference between the MMM models in Figure 3.15b and Figure 3.16b is that additional secondary sampling atoms (5%) within the cutoff distance of interpolating rep-atoms are considered in Figure 3.16b. The MMM model in Figure 3.16b is expected to more accurate since it employs more secondary sampling atoms. See the initial state at the top of the right panels of Figure 3.15 and Figure 3.16.

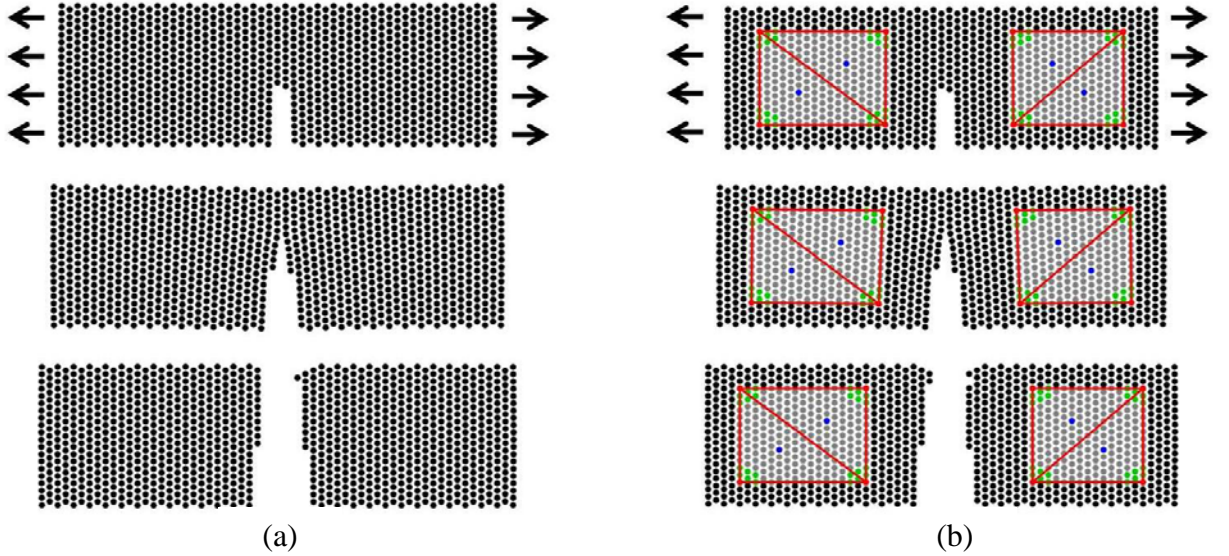


Figure 3.16: Snapshots from crack propagation of full atomistic (left) and MMM model II (right) simulations

Three snapshots from the simulations of full atomistics and the respective MMM model are shown in Figure 3.15 and Figure 3.16. The top and bottom parts of both panels show the initial and final configurations of each model, respectively. In the middle, snapshots from the crack propagation are shown. It is clear that the crack propagation path is captured by both MMM simulations very well. The stress-strain curves (Figure 3.17 and Figure 3.18) prove the ability of MMM to reasonably capture the crack propagation together with surface effects. In comparison, the model in Figure 3.16b gives better agreement with full atomistics in terms of capturing the stress-strain curve, as expected.

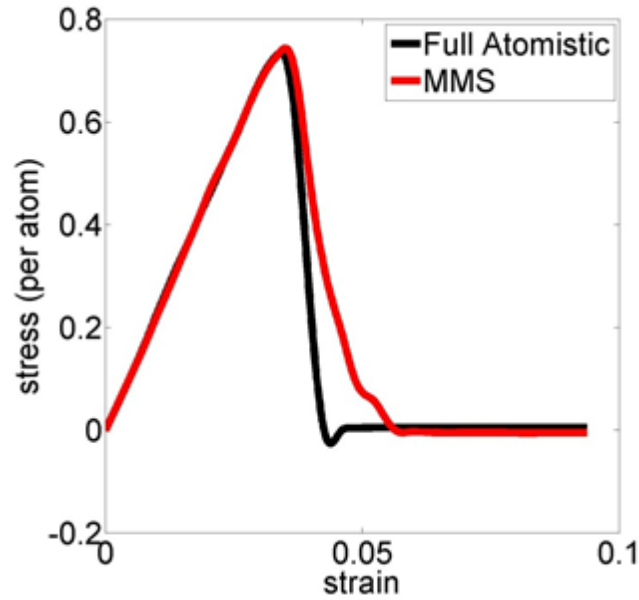


Figure 3.17: Stress-strain curves of full atomistic and MMM model I simulations of crack propagation

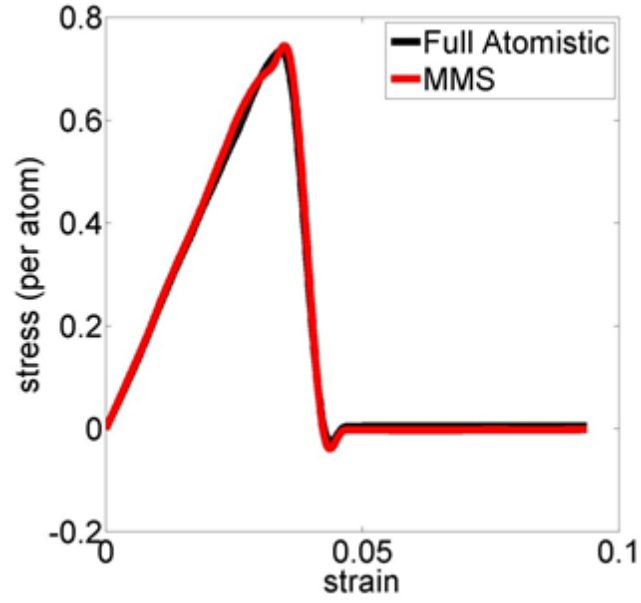


Figure 3.18: Stress-strain curves of full atomistic and MMS model II simulations of crack propagation

3.8 IRREGULAR ELEMENTS

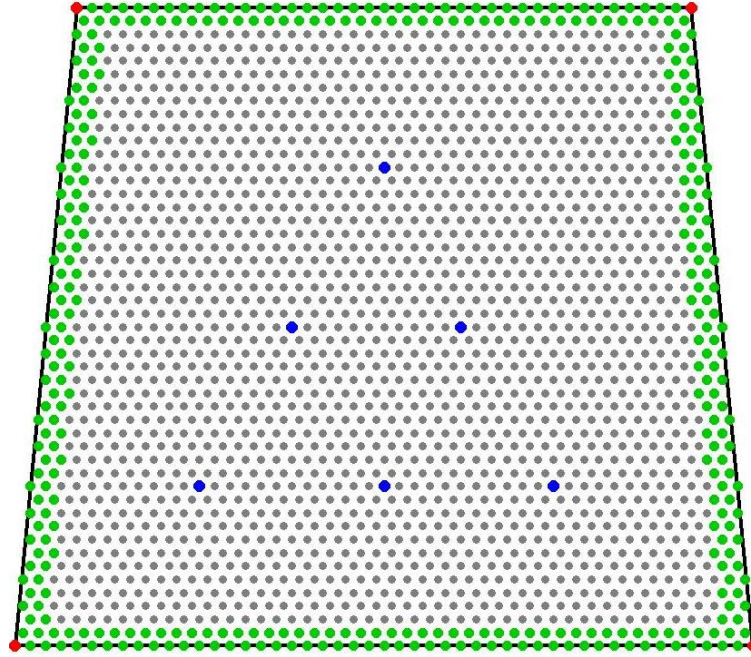
To this end, all the elements employed in numerical examples have regular shapes (rectangles and right-angled triangles). In this section, the proposed summation rule SR^B will be applied with irregular bilinear elements. Note that the shape functions of these irregular elements are built directly from the global coordinate such that iso-parametric analysis for mapped elements is not considered.

3.8.1 2D irregular atomic sheet shear model

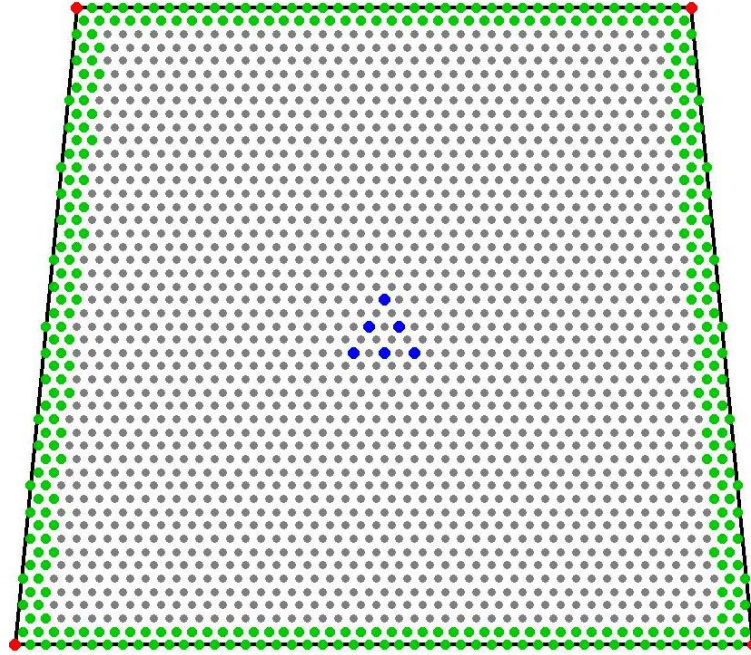
A 2D Lennard-Jones sheet with a shape of trapezoid undergoing the biquadratic shear deformation with the same boundary condition, as employed in Section 3.7, is considered.

To verify the proposed summation rule SR^B for irregular element, the trapezoidal element with SR^B -1 (Figure 3.19a) and SR^B -2 (Figure 3.19b) is used. As shown in Table 3.17, both SR^B -1 and SR^B -2 introduce little sampling errors and the difference between the two summation rules is small (i.e. less than 1%).

To reduce the discretization errors, the element size is decreased. Four irregular bilinear elements with SR^B -1 (Figure 3.20a) and SR^B -2 (Figure 3.20b) are used. As can be seen from Table 3.18, again, SR^B -1 and SR^B -2 produce similar accuracy. As expected, the discretization errors are reduced significantly. Even though the sampling errors increase by a certain amount, the discretization errors still dominate.



(a)



(b)

Figure 3.19: Schematic illustrations of primary sampling atom selections for the MMM models using irregular bilinear element (Q4) with relatively large element size and summation rules $\text{SR}^{\text{B}}\text{-1}$ and $\text{SR}^{\text{B}}\text{-2}$ employed in Section 5: $\text{SR}^{\text{B}}\text{-1}$ (a) and $\text{SR}^{\text{B}}\text{-2}$ (b).

It is worthwhile to note that the total edge sizes for irregular elements may be larger compared to that of regular elements. Thus, the number of atoms within a potential cut-off distance from the edges may increase. This may cause the increase of sampling errors and an edge summation rule SR^{edge} may be needed and employed to reduce the sampling errors. The formulation of SR^{edge} to handle irregular elements is our ongoing work and will be reported in the near future.

Table 3.17: Errors in the solution of the 2D LJ biquadratic shear problem obtained via the proposed summation rules SR^B with different choices of positions of primary sampling atoms using irregular bilinear element Q4 with relatively large element size

Summation rules	Relative displacement errors			Relative energy errors		
	e_{disp}	e_{disp}^{sam}	e_{disp}^{disc}	e_E	e_E^{sam}	e_E^{disc}
SR^B -1	61.90%	0.78%	62.52%	54.32%	0.31%	54.40%
SR^B -2	62.51%	0.03%	62.52%	54.40%	0.04%	54.40%

Table 3.18: Errors in the solution of the 2D LJ biquadratic shear problem obtained via the proposed summation rules SR^B with different choices of positions of primary sampling atoms using irregular bilinear element Q4 with relatively small element size

Summation rules	Relative displacement errors			Relative energy errors		
	e_{disp}	e_{disp}^{sam}	e_{disp}^{disc}	e_E	e_E^{sam}	e_E^{disc}
SR^B -1	21.64%	7.95%	20.50%	27.01%	7.00%	25.86%
SR^B -2	21.61%	7.95%	20.50%	26.99%	7.00%	25.86%

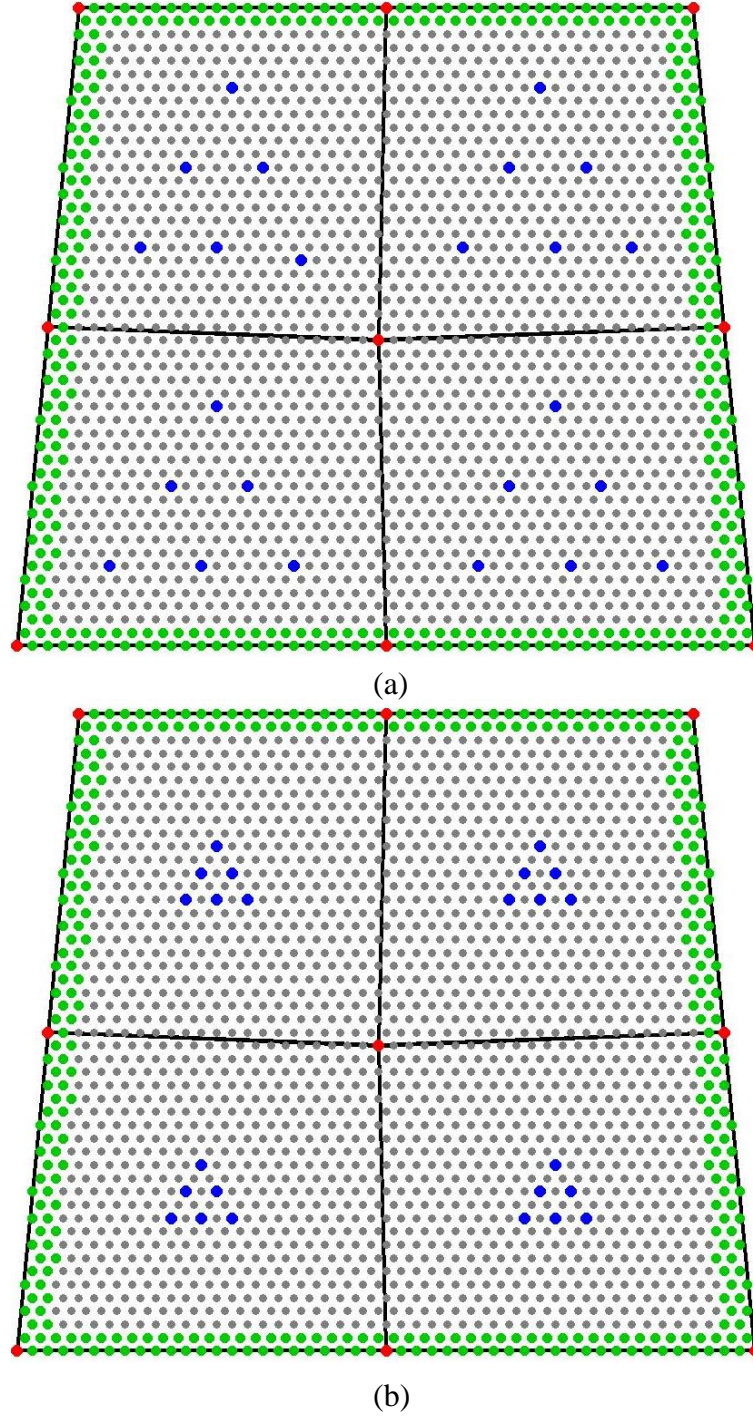


Figure 3.20: Schematic illustrations of primary sampling atom selections for the MMM models using irregular bilinear element (Q4) with relatively small element size and summation rules SR^B-1 and SR^B-2 employed in Section 5: (a) SR^B-1 and (b) SR^B-2

3.8.2 Mapped elements

Note that in sub-Section 3.8.1, the irregular quadrilateral elements used are not the mapped bilinear element as generally employed in FEM. An important reason that mapped elements in FEM are widely used is that numerical integration is difficult to be performed with respect to distorted or curved elements [125]. However, since there is no integral but only summation in MMM, the above difficulty does not exist. The proposed summation rule SR^B can be directly conducted with respect to global coordinates, as has been used in the above simulation.

Another reason that mapped elements is popular in FEM is to overcome the difficulty that the direct construction of shape functions that satisfy consistency requirements for high-order elements with curved boundaries becomes increasingly complicated [125]. The consistency across element boundaries is often required in FEM due to the better convergence and accuracy since integration over discontinuity is invalid. However, as mentioned earlier, since no integration is involved in MMM and when the element size is reduced to interatomic spacing, MMM can automatically converge to full atomistics, the consistency requirement may be “unnecessary” or relatively “weaker” in MMM as compared to FEM. In addition, non-conformity is employed in many cases even in FEM [125]. In fact, the shape functions for the irregular bilinear elements in sub-Section 3.8.1 are constructed directly from the global coordinate system.

In the future, mapped elements will be formulated for MMM and compared to cases where they are not used in MMM. A key question to be answered is whether N_{PSA} is still optimal for mapped elements. It is worthwhile to note that the order of numerical integration is often determined by the order of shape functions in local coordinates [125] in FEM. Analogously, the proposed summation rule SR^B can still be determined based on the shape functions defined via

the “parent” elements such that the calculation performed in Section 2.3 may still be valid when it is performed with respect to local coordinates. Thus, the proposed summation rule may be reasonably expected to have good performance for mapped elements.

3.9 SUMMARY

In summary, this chapter primarily presents the validation of the proposed bulk summation rule SR^B in Chapter 2.0 by employing numerical examples with respect to harmonic (spring) and non-harmonic (Lennard-Jones) potentials. To analyze the performance of any summation rule, different error sources are identified and the total error is decomposed into discretization and sampling errors. Discretization error is related to the element size and shape function order employed, as in FEM. Sampling error depends only on the summation rule, analogous to the numerical integration error with a quadrature rule in FEM. Since discretization error is fixed for a given mesh, sampling error is a good indicator of the performance of any proposed summation rule.

Rigorous error norms, as inspired by the L_2 and H_1 norms to quantify FEM accuracy in continuum mechanics, are defined to quantify the defined discretization and sampling errors in displacement and energy fields, respectively. The effectiveness of the proposed summation rule is demonstrated by employing linear, bilinear and quadratic elements to tensile, shear, bending and crack propagation problems. Compared to other summation rules, such as Gauss-quadrature rule, SR^B shows better performance in terms of accuracy and computational cost.

In addition, the interface compatibility of MMM and several other existing approaches are compared against each other. MMM shows a better interface compatibility under all tested loading conditions. The employment of MMM with irregular elements also introduces small sampling errors.

4.0 NUMERICAL VALIDATION OF SURFACE SUMMATION RULE SR^S

In this Chapter, the proposed surface summation rule SR^S in Section 2.3 will be specifically employed to capture surface effects in 2D triangular lattice and 3D face-centered cubic lattice (FCC) by using the respective 4-node quadrilateral and 8-node hexahedral finite elements. Note that SR^B will be additionally employed for the bulk region of considered lattices, as in Chapter 3.0 , such that both SR^S and SR^B are utilized to complete SR^{MMM} . The performance of SR^{MMM} will be quantified by the error norms in Chapter 3.0 .

4.1 2D SURFACE RELAXATION

In the following numerical example, the employed 2D triangle lattice (Figure 4.1) consists of 97 by 97 atoms (9361 atoms in total) interacting via the standard Lennard-Jones (LJ) potential, i.e., $U_{LJ}=4\epsilon[(\sigma/r)^{12}-(\sigma/r)^6]$ where r is the interatomic distance with the initial nearest interatomic spacing $r_0=2^{1/6}$ and potential parameters $\sigma = \epsilon =1$. The interatomic interaction is modelled up to the second nearest neighbor interaction. For boundary conditions, the lower-left corner atom is fixed in both x and y directions and the upper-left corner atom is fixed in x direction to eliminate rigid body motion. The lattice model is coarse-grained by a regular quadrilateral mesh (dashed lines) with 16 4-node quadrilateral elements. The mesh has 25 nodes or nodal atoms and takes only 0.27% over the original full atomistic (FA) degrees of freedom (DOFs), corresponding to an

element size $h_x = 24 r_0$ in x direction and $h_y = 12\sqrt{3}r_0$ in y direction. The 2D lattice model is relaxed using a non-linear Newton solver.

Since the second nearest neighbor interaction is considered, there are one surface edge and one non-bulk layer in the direction perpendicular to the bottom and top of the lattice, respectively. And there are one surface edge and three non-bulk layers in the direction perpendicular to the left and right of the lattice. As such, the surface summation rule SR^S is employed for each edge and non-bulk layer and the bulk summation rule SR^B is taken for the bulk region, as schematically shown in Figure 4.1.

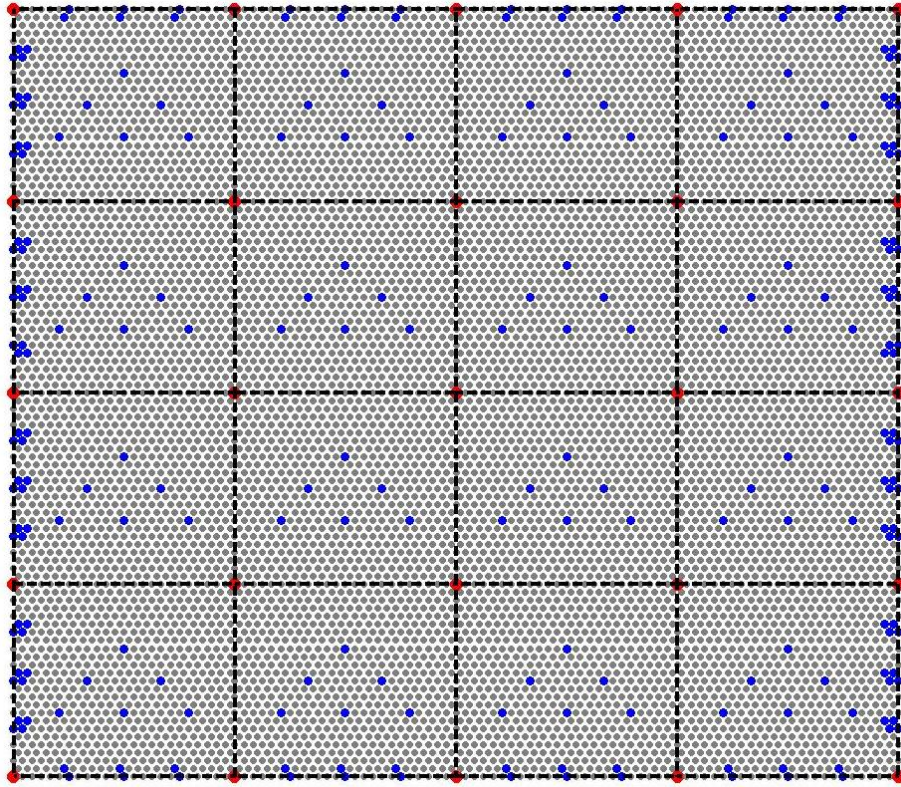


Figure 4.1: The employed 4-node quadrilateral mesh (dashed line) and summation rule SR^{MMM} for the 2D surface relaxation problem: SR^B for the bulk region and SR^S for the surface and non-bulk region

A comparison of displace field distributions from FA model and from the proposed MMM calculation is shown in Figure 4.2. The figure clearly illustrates that the proposed MMM with SR^{MMM} captures the displacement tendencies in x (Figure 4.2a and Figure 4.2b) and y (Figure 4.2c and Figure 4.2d) directions exhibited from atomistic simulation, both qualitatively and quantitatively. In order to show the capability of MMM to capture corner and edge effect, the displace fields of the upper-right corner and the middle of the edge on the right hand side, from the respective FA and MMM models, are tabulated in Table 4.1, where the accuracy of MMM is demonstrated.

Table 4.1: Normalized displacement comparison between full atomistic (FA) simulation and MMM calculation at the upper right corner and the middle of the edge at the right hand side

Method	Corner		Middle of edge	
	u_x	u_y	u_x	u_y
FA	1	1	1	1
MMM	1.04	0.94	1.02	0.94

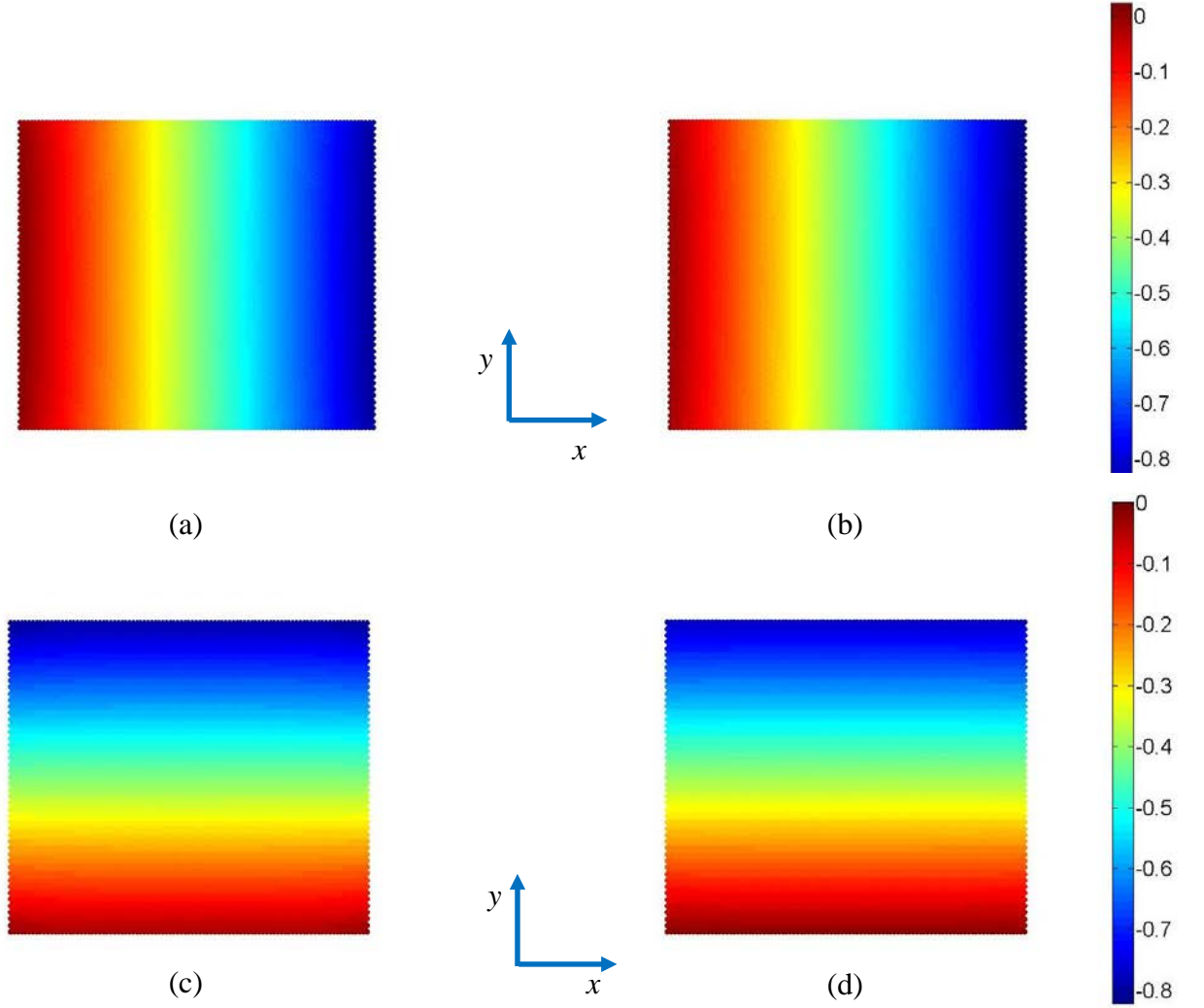


Figure 4.2: Comparison of displacement distributions from full atomistic (FA) calculation and MMM: the x -displacement distributions from FA (a) and MMM (b); the y -displacement distributions from FA (c) and MMM (d)

In addition, the different error types defined in Section 3.2 are presented in Table 4.2. As mentioned in Section 3.2, the discretization error is determined for a given mesh. Thus the sampling error is a good (if not best) indicator about the performance of a proposed summation rule. In general, to minimize the total error e_U^{total} , the sampling error e_U^{sam} has to be minimized.

As can be seen from Table 4.2, the introduced e_U^{sam} and e_E^{sam} are 0.04% and 0.0006% in displacement and energy field, respectively, with the proposed SR^{MMM}. The small sampling errors quantify the good performance of MMM.

Table 4.2: Different types of errors in displacement and energy field in the 2D example

Summation rule	e_U^{total}	e_U^{disc}	e_U^{sam}	e_E^{sam}
SR ^{MMM} (SR ^B +SR ^S)	4.85%	4.82%	0.04%	0.0006%

4.2 3D SURFACE RELAXATION

The numerical example considered next is the free surface relaxation of an FCC crystal lattice. The FCC lattice consists of 24 by 24 by 24 unit cells in the x , y and z directions, corresponding to 58825 atoms as shown in Figure 4.3. The same interatomic potential employed in 2D surface relaxation example is also used here. The atomic interaction is truncated after the third shell of the nearest neighbors. To eliminate rigid body motions, the boundary conditions in $[100]$ are employed. Let the cubic center be the origin and L be the length of the cube edge. The corner at $(-L/2, -L/2, -L/2)$ is fixed in all directions, the corner at $(L/2, -L/2, -L/2)$ is fixed in y and z directions and the corner at $(-L/2, L/2, -L/2)$ is fixed in the z direction.

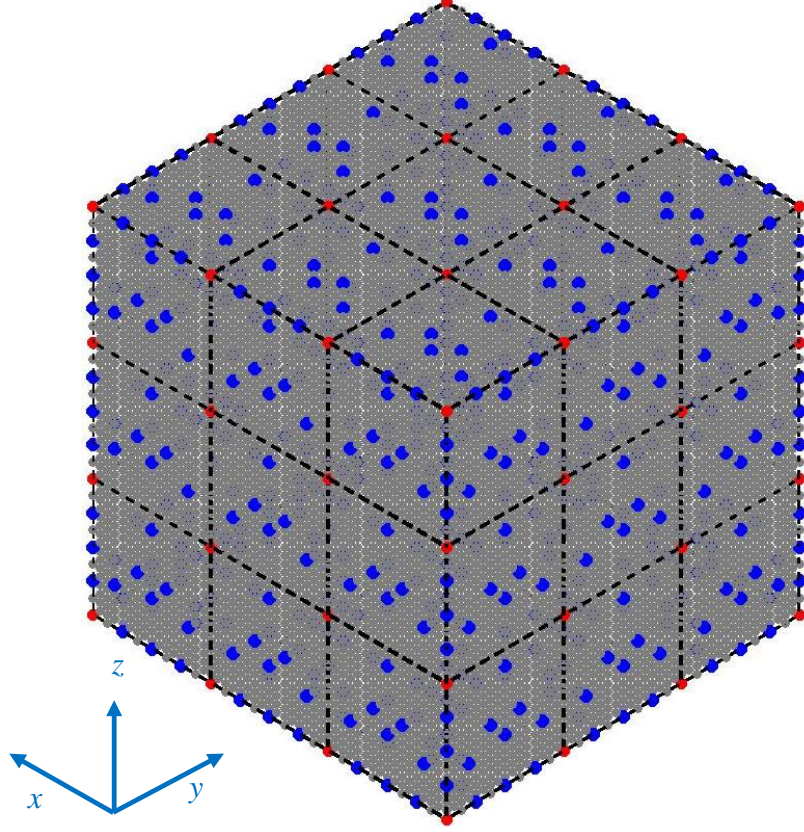


Figure 4.3: The employed 8-node quadrilateral mesh (dashed line) for the 3D problem: the blue dots on the free surfaces and edges shows the applied SR^S ; SR^S and SR^B are also utilized for the non-bulk layers and bulk layers, respectively, and are invisible

To coarse grain the FCC lattice, a regular hexahedral mesh (dashed lines) with 27 8-node hexahedral elements is introduced, as shown in Figure 4.3. The mesh has 64 nodal atoms with an element size $h = 8\sqrt{2}r_0$ in each direction, which takes only 0.11% of the original FA DOFs. Since the atomic interaction is modelled up to the third shell of nearest neighbors, there is one free surface and one non-bulk layer in the direction perpendicular to each cubic side surface, as shown in Figure 4.4. Then SR^S is applied to both the free surface and the non-bulk layer, as

illustrated in Figure 4.3. Note that SR^S applied to the non-bulk layer is invisible in Figure 4.3. The employed SR^B is schematically shown in Figure 4.5, as mentioned in Section 2.3.

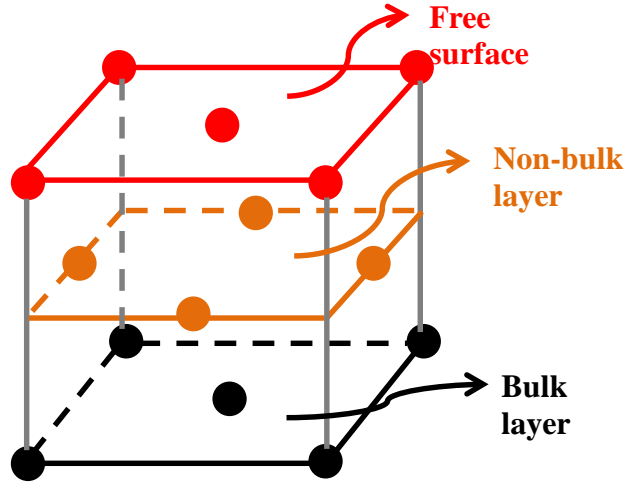


Figure 4.4: The respective free surface, non-bulk and bulk layers of the 3D example: SR^S is applied to both free surface and non-bulk layers and SR^B is employed for bulk layers

Figure 4.6-Figure 4.8 show the displacement distribution comparison between FA modeling and MMM simulation. As can be seen, MMM accurately captures the distribution trend in each (positive or negative) direction, as what has been observed in 2D. The expansion or contraction of a surface is clearly matched in x , y and z directions. In order to compare the distribution inside the cube, the models in Figure 4.6-Figure 4.8 are cut through by $x=0$, $y=0$ and $z=0$ planes, respectively. As shown in Figure 4.9-Figure 4.11, very good agreement has been achieved. The purpose of showing the distribution pattern in each direction is to demonstrate that MMM has uniform accuracy in each direction and no direction preference is observed, as will be shown in Table 4.3.

The displacement fields for the corner at $(L/2, L/2, L/2)$, the atom at the middle of the edge connecting corners at $(L/2, -L/2, L/2)$ and $(L/2, L/2, L/2)$, and the atom at the center of $+x$ free surface are presented in Table 4.3 to show the capability of MMM to capture corner, edge and surface effects in 3D. The uniform accuracy of MMM in each direction is clearly demonstrated in Table 4.3.

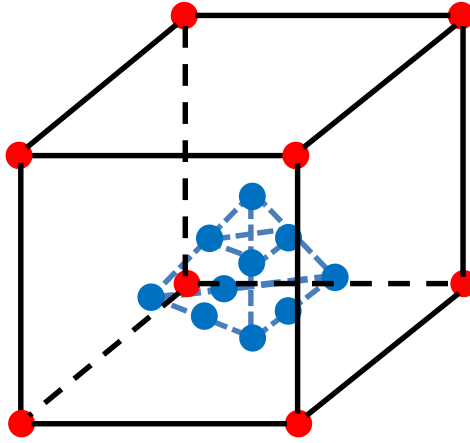


Figure 4.5: Schematically demonstration of the employed SR^B with 8-node hexahedral element for bulk layers: red dots are the nodal atoms and blue dots represent the selected primary sampling atoms (*PSAs*)

Table 4.3: Normalized displacement comparison between full atomistic (FA) simulation and MMM calculation at corner, middle of edge and face center in the 3D example

Method	Corner			Middle of edge			Face center		
	u_x	u_y	u_z	u_x	u_y	u_z	u_x	u_y	u_z
FA	1	1	1	1	1	1	1	1	1
MMM	0.89	0.90	0.89	0.92	0.91	0.92	0.95	0.91	0.90

To more rigorously understand the performance of MMM in 3D, e_U^{total} , e_U^{disc} , e_U^{sam} and e_E^{sam} are presented in Table 4.4. The introduced e_U^{sam} and e_E^{sam} are 0.71% and 0.086%, respectively. As what has been observed in 2D, the good performance of MMM lies in that SR^{MMM} accurately represents and reproduces the energy distribution of coarse-grained atomistic model with solid mathematical foundation.

Table 4.4: Different types of errors in displacement and energy field in the 3D example

Summation rule	e_U^{total}	e_U^{disc}	e_U^{sam}	e_E^{sam}
$SR^{MMM}(SR^B + SR^S)$	9.92%	10.30%	0.71%	0.086%

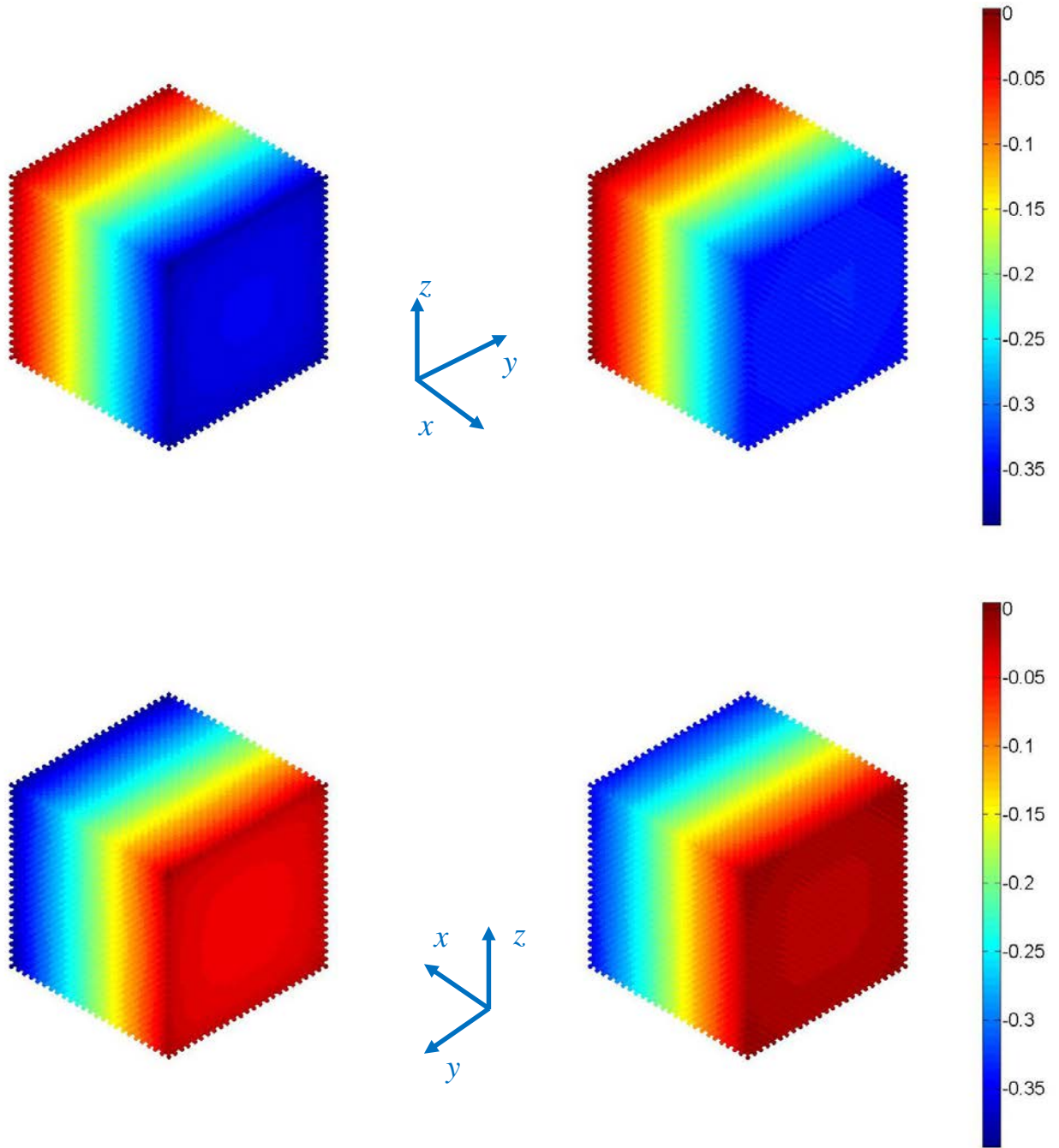


Figure 4.6: Comparison of x -displacement distributions on surfaces from full atomistics (FA) and MMM: $+x$ -displacement from FA (a) and MMM (b); $-x$ -displacement from FA (c) and MMM (d)

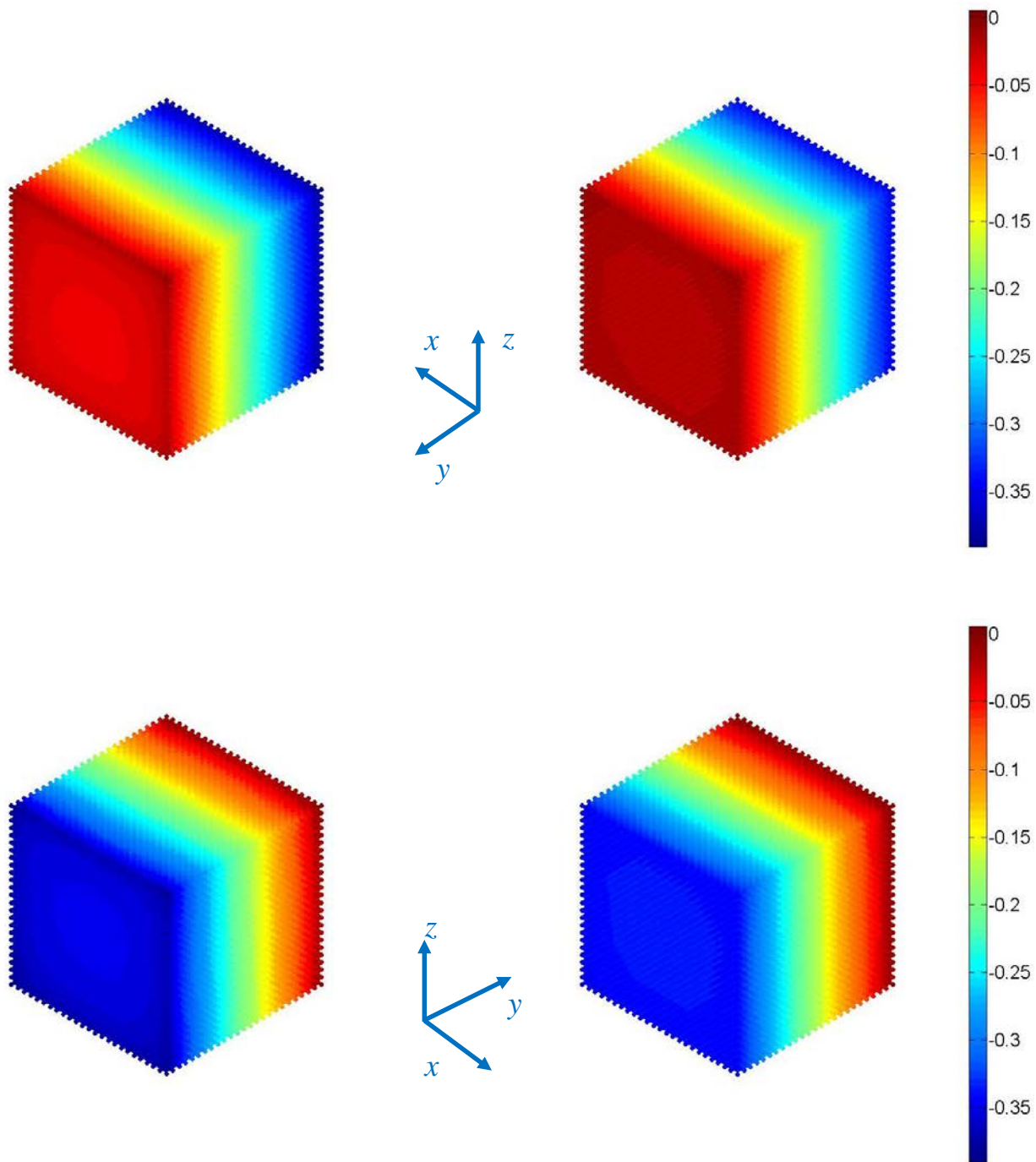


Figure 4.7: Comparison of y -displacement distributions on surfaces from full atomistics (FA) and MMM: $+y$ -displacement from FA (a) and MMM (b); $-y$ -displacement from FA (c) and MMM (d)

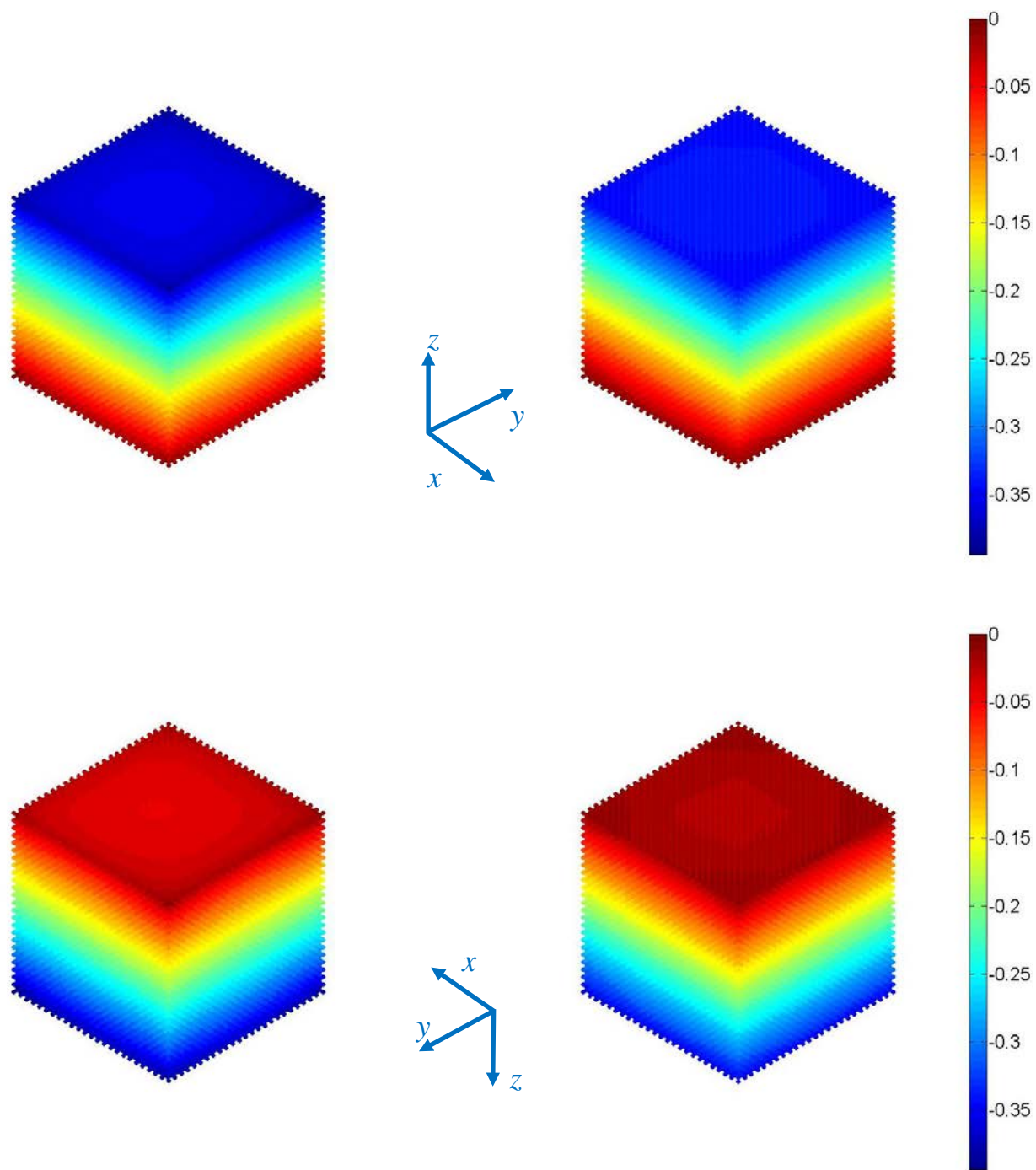


Figure 4.8: Comparison of z -displacement distributions on surfaces from full atomistics (FA) and MMM: $+z$ -displacement from FA (a) and MMM (b); $-z$ -displacement from FA (c) and MMM (d)

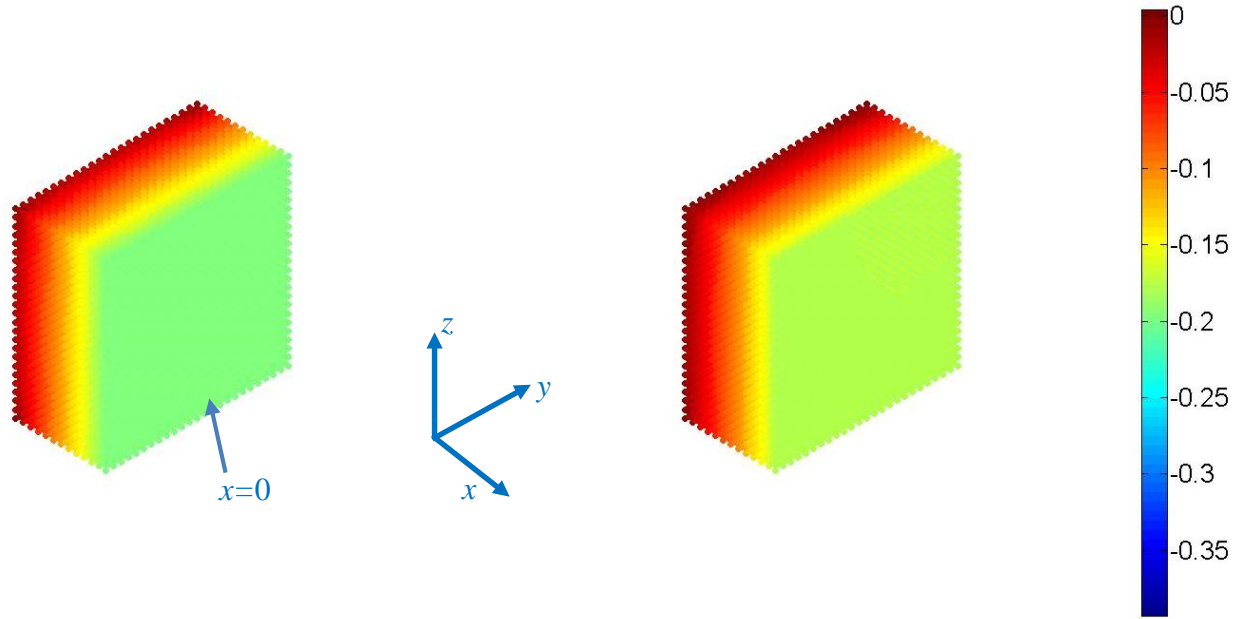


Figure 4.9: Comparison of x -displacement distributions from bulk along the plane $x = 0$ from full atomistics (FA) (a) and MMM (b)

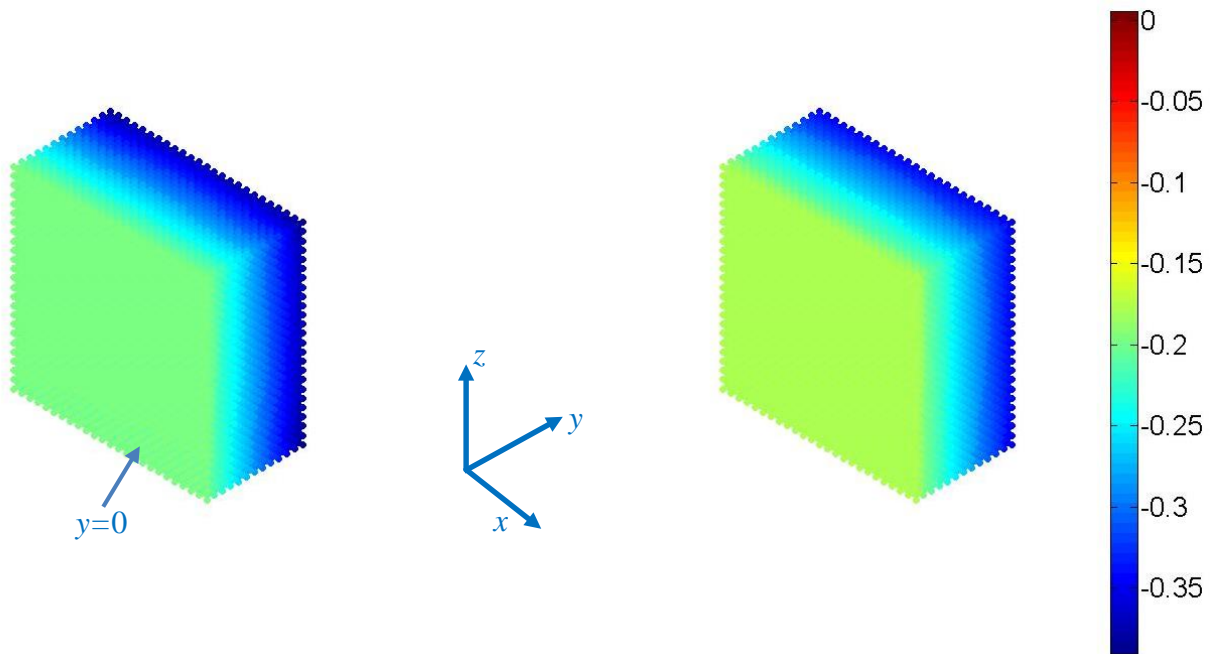


Figure 4.10: Comparison of y -displacement distributions from bulk along the plane $y = 0$ from full atomistics (FA) (a) and MMM (b)

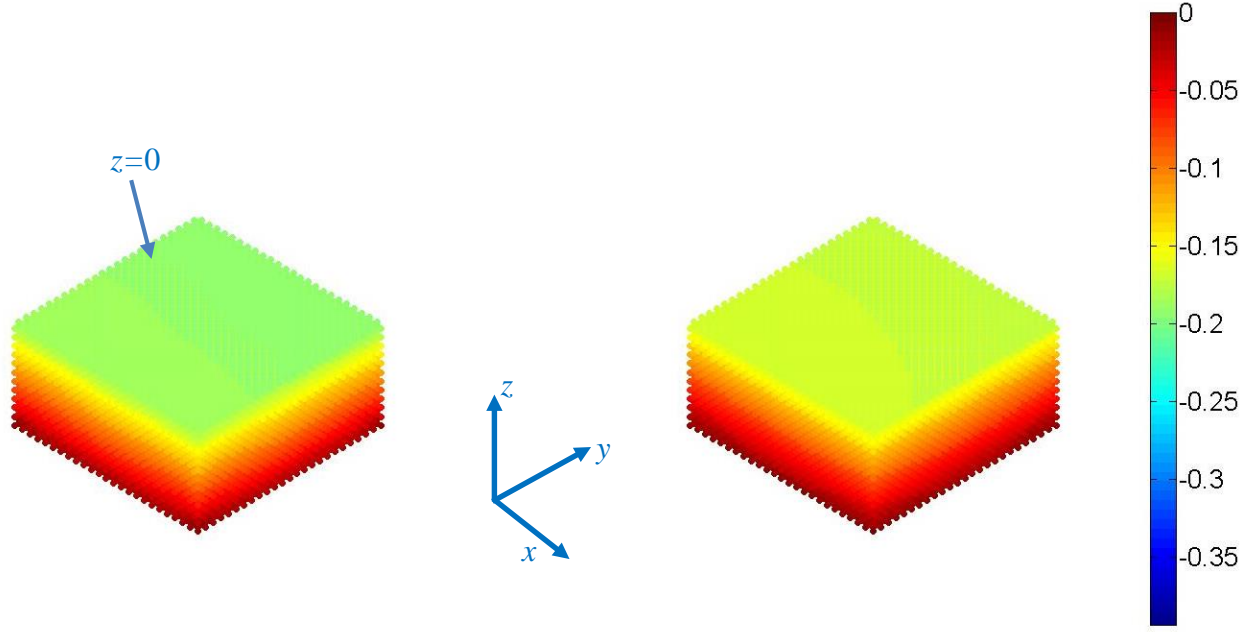


Figure 4.11: Comparison of z -displacement distributions from bulk along the plane $z = 0$ from full atomistics (FA) (a) and MMM (b)

4.3 SUMMARY

This chapter specifically applies the surface summation rule SR^S proposed in Chapter 2.0 to capture surface effects in nanosized structures.

For both the 2D triangle lattice and 3D FCC model, the proposed SR^S qualitatively and quantitatively captures the mechanical response as demonstrated in the two surface relaxation examples, using the respective 4-node quadrilateral and 8-node hexahedral meshes. The contraction or expansion of a surface clearly matches with the FA simulation results. A comprehensive comparison between displacement results from FA simulation and MMM shows similar and uniform accuracy of MMM in x , y and z directions. Corner and edge effects are also accurately captured. Furthermore, the proposed SR^{MMM} introduces very small sampling errors as

quantified by the error norms defined in both the displacement and energy fields. As such, full FA results can be accurately reproduced by MMM with 0.3% less in the number of degrees of freedom of the original atomistic system. The good performance of SR^S is expected and is easy to understand since SR^S in 3D is, in fact, SR^B in 2D and SR^S in 2D is actually in SR^B 1D. Physically, this is because that for cubes, the boundary of 3D model is two-dimensional surface and the edge of a 2D surface is one-dimensional line.

5.0 NUMERICAL CONVERGENCE AND ERROR STRUCTURE ANALYSIS

In this Chapter, the convergence behavior of MMM will be numerically studied with respect to linear element using the norms defined in Section 3.2. To explain the observed convergence behavior of MMM, the discretization and sampling errors defined in Section 3.1 are numerically analyzed with respect to different element size. The effect of exact solution smoothness and regularity and the nonlinearity of interatomic potential are also considered. It is observed that MMM demonstrates FEM-like behavior under certain circumstance.

5.1 CONVERGENCE STUDY

Four different MMM models (Figure 5.1) with different sampling schemes, as demonstrated in [43], are employed here to perform the convergence study. Note that SR^B is employed for all the MMM models such that N_{PSA} is 1 for linear element. The difference among different sampling schemes is how the secondary sampling atoms (SSAs) (green dots) are employed. For the purpose of standardization and convenience of referencing, the four schemes will be denoted as follows. In scheme I, only one primary sampling atom (PSA) and no secondary sampling atoms (SSA) are employed in each element, and thus scheme I will be denoted as 1p0s (Figure 5.1a) with “p” meaning PSAs and “s” SSAs. In scheme II, one PSA in each element is considered with surface ghost atoms taken as SSAs, and this scheme is named 1p~s (Figure 5.1b) with “~”

representing surface, as mentioned in Chapter 3.0 . In scheme III, one *PSA* in each element is employed with the neighbors of rep-atoms treated as *SSAs*, and scheme III is named 1p@s (Figure 5.1c) with “@” representing neighbors of nodal atoms. In scheme IV, all ghost atoms are taken as *SSAs* and no *PSAs* is used, and this scheme is denoted as 0p*s (Figure 5.1d). In summary, these schemes are denoted based on how to choose *SSAs* (green dots). In fact, the freedom of choosing *SSAs* gives much flexibility using MMM in optimizing between efficiency and accuracy. As mentioned in Section 3.1, MMM model with Scheme 0p*s is, in general, the most accurate and, of course, the most computationally intensive model. The purpose of employing scheme 0p*s is for comparison with the other three schemes and for error structure analysis.

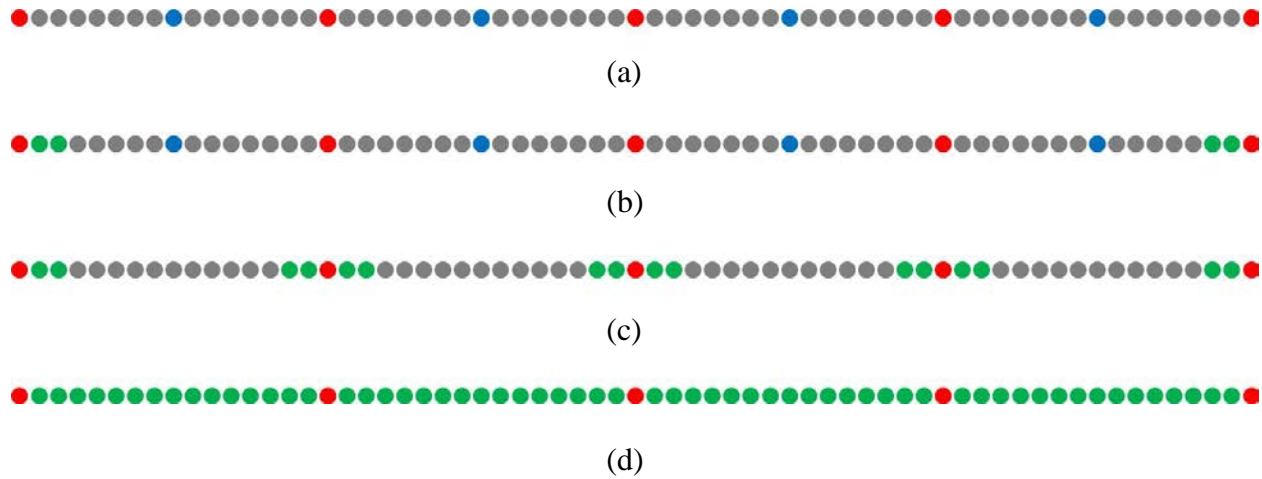


Figure 5.1: Four different MMM models with the corresponding sampling schemes with an element size of $16r_0$ (r_0 is the initial atomic spacing): scheme 1p0s (a); scheme 1p~s (b); scheme 1p@s (c) and scheme 0p*s (d)

It is well-known in continuum mechanics that the regularity and smoothness of the exact solution have a significant effect on the convergence of FEM and that the optimal convergence order is reached only if the exact solution has enough smoothness [126]. To study the effect of the exact solution smoothness of atomistic models on MMM convergence, three different types of external force loadings are applied to the atomic models, respectively. The external force loadings are: (1) the quadratic-deformation force loading; (2) the uniformly distributed force loading and (3) the random force loading of uniform distribution. Note that the exact displacement solutions of atomistic models are given by discrete points instead of a function, because of finite degrees of freedom. We say the exact solution of an atomistic model is smooth only if the discrete points fall exactly on a smooth function and is less smooth if not. The quadratic-deformation force loading is employed to generate quadratic displacement fields, as motivated by commonly used 1D string model and 2D beam model in solid mechanics to test the convergence of FEM and meshfree method [123, 127]. Then the exact solutions under quadratic-deformation loadings are smooth. With the second and third force loadings mentioned above to atomic models, the true displacement field generated, in general, is less smooth.

The error norms defined in Eq. (3.4) and (3.5) are employed to quantify the convergence rate in displacement and energy field, respectively.

5.1.1 1D convergence test

The 1D nonlocal spring model consists of 67 atoms with a harmonic potential of interaction forces for both the first and second nearest neighbors. These atoms are positioned as $r_i = ir_0$, $i = 1-67$, where r_0 is the zero-force spring length for the first neighbor springs. The consideration of second-neighbor interaction gives the non-locality of typical atomistic models. The spring

constant for the nearest-neighbor interaction is represented by k_1 and that for the second-neighbor interaction by k_2 . A zero-force spring length of r_0 is assumed for the first neighbor springs and of $2r_0$ for the next-nearest neighbor springs. In the numerical implementation, 1.0, 0.25, and 1.0 are assigned to be the values of k_1 , k_2 , r_0 , respectively. For MMM spring models, different element sizes are tested and normalized by r_0 . The normalized element sizes h are 64, 32, 16, 8, 4, 2, and 1, respectively.

To study the effect of nonlinearity of interatomic interaction on the convergence of MMM models in 1D, the same 1D atomic chain above is employed except that the Lennard-Jones (LJ) potential (i.e. $U_{LJ}=4\epsilon[(\sigma/r)^{12}-(\sigma/r)^6]$ where r is the interatomic distance) with potential parameters $\sigma=\epsilon=1$ and the second nearest neighbor interactions is taken to describe the interaction between atoms. The atoms are placed initially with interatomic distance $r_0=2^{1/6}\sigma$. As in the harmonic case, the MMM LJ models with the normalized element size h equal to 64, 32, 16, 8, 4, 2, 1, are employed, respectively. Three different force loadings mentioned are applied to both the spring and LJ models. The exact solutions from full atomistics (FA) of the respective force loading conditions for 1D for spring and LJ models are shown in Figure 5.2 and Figure 5.3, respectively. The displacements are normalized by the respective r_0 .

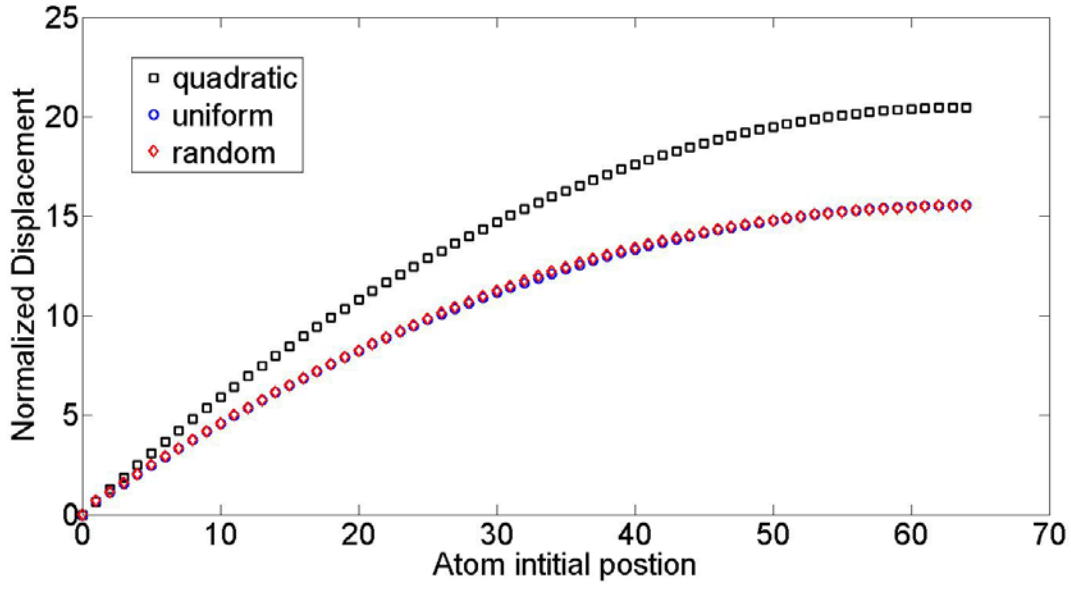


Figure 5.2: Exact solutions from atomistics for the 1D spring model for the quadratic-deformation loading (black), the uniform force loading (blue) and the random force loading of uniform distribution (red)

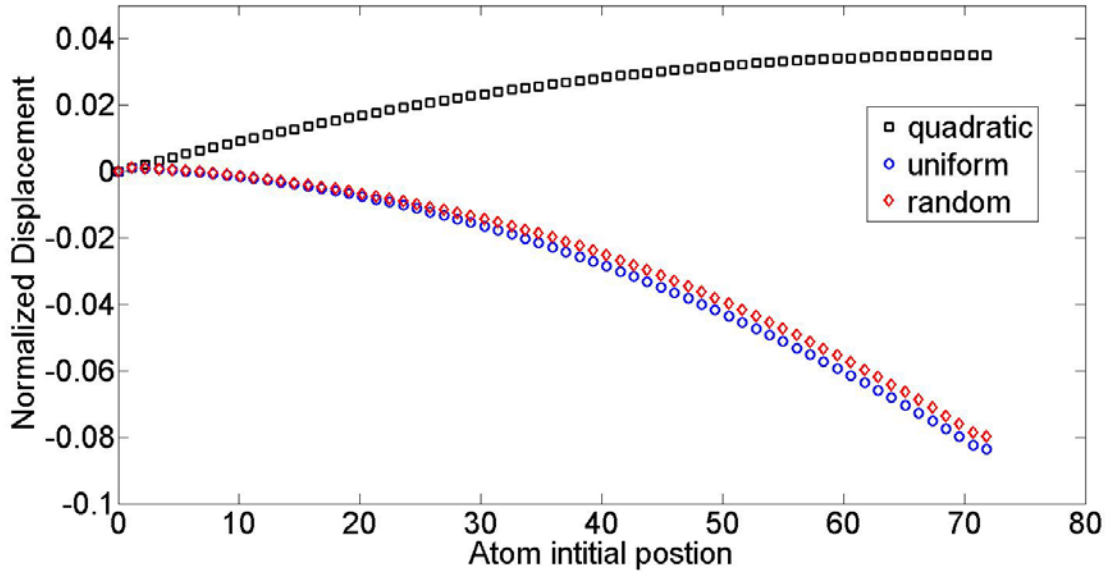


Figure 5.3: Exact solutions from atomistics for the 1D LJ model for the quadratic-deformation loading (black), the uniform force loading (blue) and the random force loading of uniform distribution (red)

5.1.1.1 Quadratic-deformation force loading: harmonic potential

The quadratic-deformation force loading generates a quadratic displacement field as motivated by a commonly used 1D loaded string model with a length of l_0 to test the convergence of FEM and mesh-free methods [123]:

$$\mathbf{E}\mathbf{u}_{,xx} + \mathbf{f}(x) = 0, x \in (0, l_0) \quad (5.1a)$$

$$\mathbf{u}(0) = 0 \quad (5.1b)$$

$$\mathbf{u}_{,x}(l_0) = 0 \quad (5.1c)$$

The quadratic displacement field takes the following form with $\mathbf{E} = 1$ and $\mathbf{f}(x) = x$:

$$\mathbf{u} = -\frac{1}{2}x^2 + l_0x \quad (5.2)$$

where \mathbf{u} represents the displacement and x is the coordinate. To generate a quadratic deformation field for the 1D nonlocal atomic spring model, besides the same boundary conditions are employed as in the 1D continuum case, three more steps are taken: (I) the quadratic-deformation field given by Eq. (5.2) scaled by a factor of 100 is employed to generate the final deformation for each atom by substituting in the original coordinate of each atom; (II) having the final deformation of each atom, the force needed to equilibrate each atom can be calculated; (III) applying the forces calculated from step II as the external forces to the 1D spring model to generate the quadratic-deformation field given in step I. The extension to the 1D LJ potential follows the same three steps except that the quadratic-deformation field given by Eq. (5.3) is employed. The main purpose to employ such a quadratic displacement field for the discrete atomic model in this loading case is to investigate the effect of displacement smoothness on the performance of MMM.

Figure 5.4a and Figure 5.4b show the convergence in the error norms defined above for all the four MMM schemes for the atomic spring chain. MMM models converge to molecular

statics monotonically when the element size decreases to atomic spacing and the zero-error point is not shown in the log-log plots. As expected, scheme 0p*s gives the most accurate results and it shows a linear convergence with a slope of 2.007 ($R^2=1.0000$) in the displacement error norm and with a slope of 1.034 ($R^2=0.9993$) in the energy error norm. Note that scheme 1p@s demonstrates similar accuracy and linear convergence. Thus MMM with scheme 0p*s and 1p@s shows FEM-like behavior in this convergence test with respect to the convergence order. Schemes 1p0s and 1p~s show similar performance as Schemes 0p*s and 1p@s for large element size. However, for some small element sizes, discrepancy between the schemes is observed. We will explain the performance of each scheme and the discrepancy between them from a point of view of error structure analysis in next section.

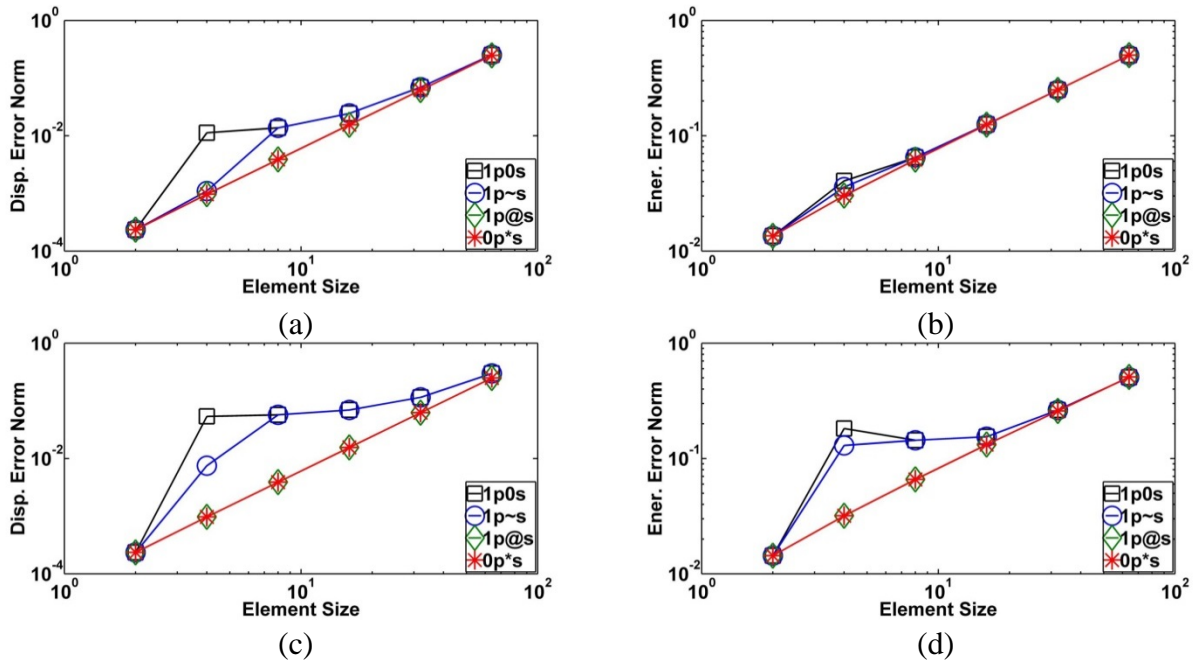


Figure 5.4: Convergence of the 1D spring model subject to the corresponding quadratic-deformation force loading in the relative displacement error norm (a) and the relative energy

error norm (b); convergence of the 1D LJ model subject to the corresponding quadratic-deformation force loading in the relative displacement error norm (c) and the relative energy error norm (d)

5.1.1.2 Quadratic-deformation force loading: Lennard-Jones potential

As mentioned in [13, 128], if the interatomic distances of some pairs of nearest neighbors are located outside the convex region of the LJ potential, where the second derivative of the potential is negative, the convergence analysis may be problematic since the solution may not be unique. Thus for the non-harmonic LJ potential, we constrain the deformation field such that all nearest pairs are in the convex region. This is achieved in two steps: (I) find the inflection point of LJ potential, i.e., the critical interatomic distance r_c ; (II) multiply Eq. (5.2) by some constant α less than unity such that the corresponding maximum strain is $\varepsilon_{max} \leq r_c/r_0$. In this study, α is chosen to be 1.52×10^{-4} and the constrained displacement field is given as:

$$\mathbf{u} = \alpha \left(-\frac{1}{2}x^2 + l_0x \right) \quad (5.3)$$

The above quadratic displacement field is employed for the atomic LJ chain.

Figure 5.4c and Figure 5.4d show the convergence in the error norms defined above for all the four MMM schemes for the atomic LJ chain. As observed in the corresponding harmonic spring case, scheme 0p*s gives the most accurate results and it shows a linear convergence with a slope of 2.007 ($R^2=1.0000$) in the displacement error norm and with a slope of 1.023 ($R^2=0.9990$) in the energy error norm with scheme 1p@s demonstrating similar accuracy and linear convergence. Thus MMM with scheme 0p*s and 1p@s still shows FEM-like behavior with nonlinearity of interatomic interaction from the point of view of convergence order in this

convergence test. The comparison between the four schemes is similar to what is seen in the spring case.

In Figure 5.4, for both the 1D spring and LJ models, it can be seen that the convergence trend and the magnitude of relative errors of each MMM scheme are similar. The discrepancy between schemes for the LJ model may be slightly larger than that for the spring model for small element size in this loading case.

5.1.1.3 Uniformly distributed force loading: harmonic potential

A uniformly distributed loading $f_x = 0.0148$ is applied to the atomic spring chain with the same boundary conditions used in the corresponding quadratic-deformation force loading case. The sum of f_x is equal to the sum of external forces that generate the corresponding quadratic-deformation field in the previous spring case. Note that the resulting displacement field is not as smooth as that for the quadratic loading.

Figure 5.5a and Figure 5.5b demonstrate the convergence of MMM models in displacement error norm and energy error norm with uniformly distributed loading for the spring model. All the four MMM models converge to molecular statics monotonically as the element size approaches the atomic spacing. Compared with Figure 5.4a and Figure 5.4b, convergence is less linear for any of the schemes. In Figure 5.5a and Figure 5.5b, the last three data points from scheme 0p*s form a linear curve with a slope of 0.7092 ($R^2=0.9978$) and 0.2788 ($R^2=0.9962$) in the displacement error and energy error norm plot, respectively, which are smaller than the values from the quadratic loading study. The observation here is consistent with what has been proved and observed in continuum mechanics to study the convergence of FEM in the sense that the convergence order is reduced if the exact solution is not smooth enough [126]. The discrepancy between different schemes is relatively smaller in this case.

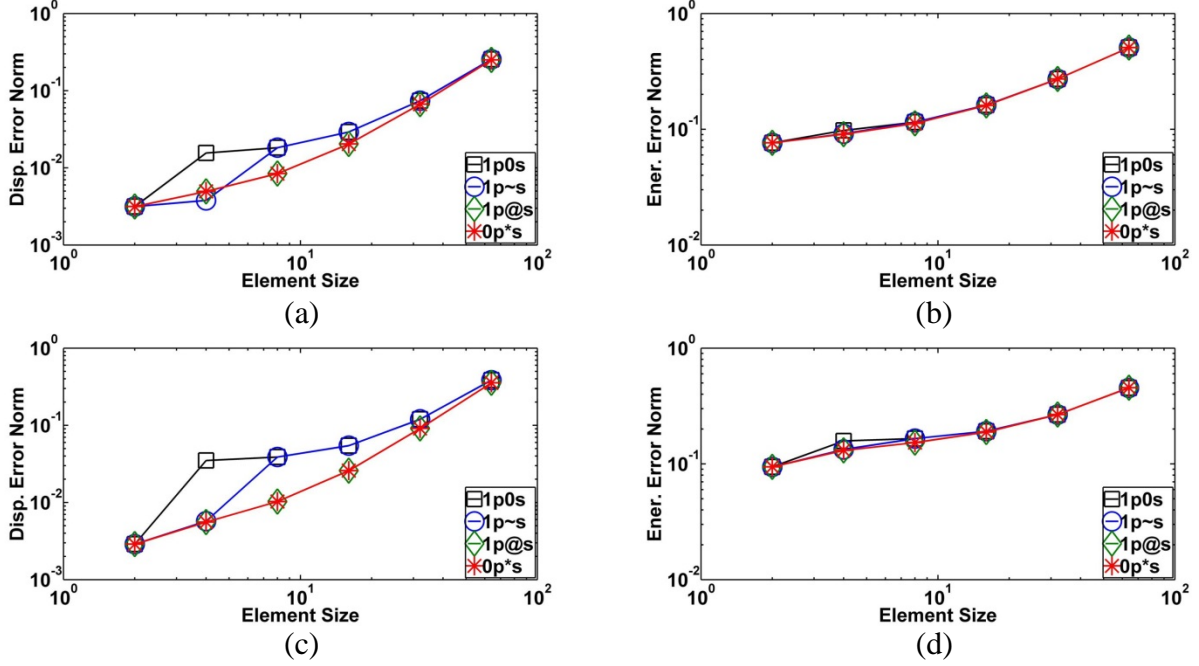


Figure 5.5: Convergence of the 1D spring model subject to the corresponding uniformly distributed force loading in the relative displacement error norm (a) and the relative energy error norm (b); convergence of 1D LJ model subject to the corresponding uniformly distributed force loading in the relative displacement error norm (c) and the relative energy error norm (d)

5.1.1.4 Uniformly distributed force loading: Lennard-Jones potential

A uniformly distributed loading $f_x = 0.0024$ is applied to the LJ atomic chain with the same boundary conditions used in the corresponding quadratic-deformation loading case. The sum of f_x is equal to the sum of external forces that generate the quadratic-deformation field in the previous LJ case.

Figure 5.5c and Figure 5.5d demonstrate the convergence of MMM models in displacement error and energy error norms with the uniformly distributed loading for the LJ model. As in Figure 5.5a and Figure 5.5b in the corresponding spring models, all four MMM models converge to molecular statics monotonically as the element size approaches the atomic

spacing and less linear convergence rate is observed for any of the schemes. In Figure 5.5c and Figure 5.5d, the last three data points for scheme 0p*s form a linear curve with a slope of 0.9168 ($R^2=0.9995$) and 0.3481 ($R^2=0.9590$) in the displacement error and energy error norm plot, respectively, which is consistent with the observation in continuum mechanics to study of effect of displacement smoothness on the convergence of FEM. The discrepancy between different schemes is relatively smaller in this loading case, compared to the previous one.

In Figure 5.5, as what is observed in Figure 5.4 in the quadratic-deformation loading case, for both models, MMM shows similar convergence trend. Scheme 1p@s shows the same order of accuracy as scheme 0p*s gives, which demonstrates the effectiveness of MMM sampling framework. Note that the convergence rate will decrease or increase depending on different element size and scheme, which will be explained in the next section from analyzing the error structure.

5.1.1.5 Random force loadings of uniform distribution: harmonic and LJ potentials

A random loading with uniform distribution is applied to the atomic spring chain with the same boundary conditions used in the previous two cases. The mean value of the random load f_x is equal to the one in the corresponding uniformly distributed loading case. The main purpose in employing such a loading is to investigate the convergence behavior of MMM in a more general case.

A random force loading with uniform distribution is applied to the atomic LJ chain with the same boundary conditions used in the previous two cases. The mean value of the random load f_x is equal to the one in the corresponding uniformly distributed loading case for the LJ model.

Figure 5.6 shows the convergence of MMM schemes for the respective 1D spring and LJ model. The convergence curves look similar to those in Figure 5.5, and thus the analysis in the uniformly distributed loading case holds here. Note that from Figure 5.2 and Figure 5.3 we can see that the resulted displacement fields for the uniformly distributed loading and the random loading of uniform distribution are similar, though not the same. This may suggest that MMM shows similar performance when the displacement fields have similar smoothness.

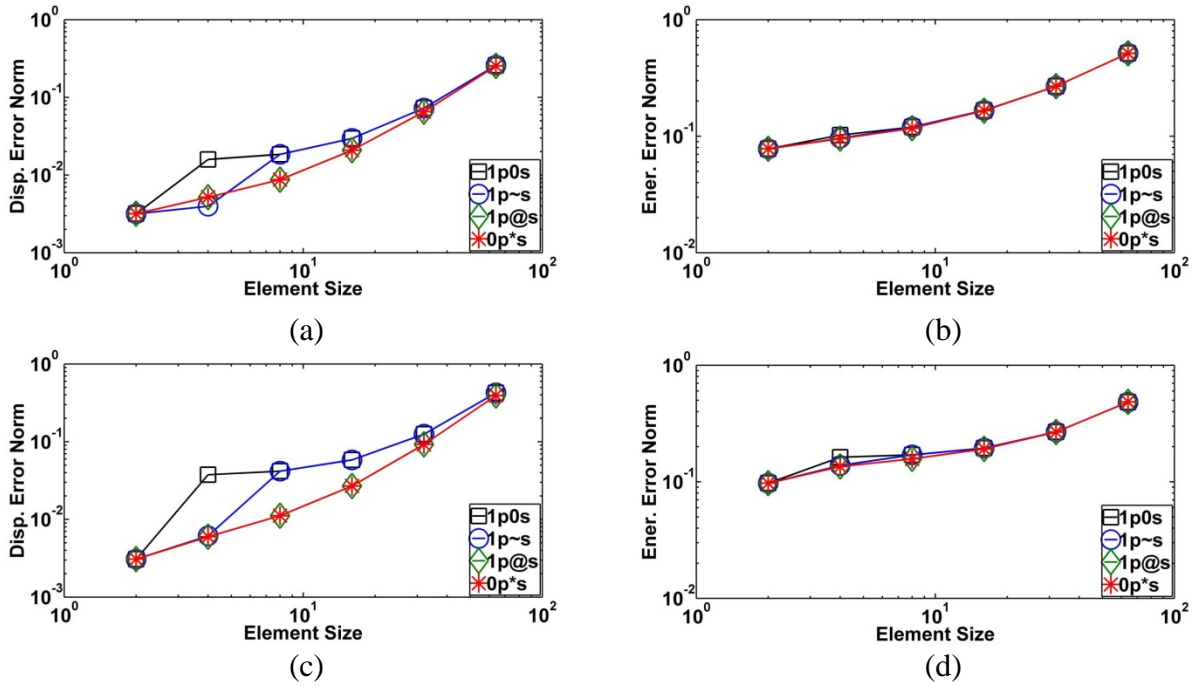


Figure 5.6: Convergence of the 1D spring model subject to the corresponding random force loading of uniform distribution in the relative displacement error norm (a) and the relative energy error norm (b); convergence of the 1D LJ model subject to the corresponding random force loading of uniform distribution in the relative displacement error norm (c) and the relative energy error norm (d)

5.1.2 2D convergence test

The 2D non-local beam model consists of 97 by 25 atoms, (2,413 atoms in total) placed on a triangular lattice with nearest neighbor interatomic distance r_0 as shown in Figure 5.7. Three different potentials are introduced to describe the interactions between atoms, for purpose that will become clear later. The definitions of the two different harmonic potentials (i.e. spring models) are given below by Eq. (5.4) and (5.5), respectively:

$$U_{s1} = \sum_i^N \frac{1}{2} k_i [(r_x - r_{x0})^2 + (r_y - r_{y0})^2] \quad (5.4)$$

$$U_{s2} = \sum_i^N \frac{1}{2} k_i (r - r_0)^2 \quad (5.5)$$

where N is the number of spring pairs considered; k_i is the stiffness constant associated with the i th spring pair; r_x and r_y denote the projection of the current pair distance r in x and y directions, respectively; r_{x0} and r_{y0} represent the projection of the initial pair distance r_0 in x and y directions, respectively. The difference between the two spring potentials is that the global stiffness matrix for the system is constant for the first spring model but is a function of the displacements for the second spring model. This non-constant property of stiffness matrix can be easily verified by considering the second order derivatives of the spring potential. Note that this difference disappears in the 1D case where $U_{s1} = U_{s2}$ and that U_{s1} is actually a fictitious potential in that it does not exist in the way that atoms interact with each other in 2D and 3D problems. The main purpose to employ such a fictitious potential here is to study the possibly different effects of constant and non-constant stiffness matrices on the convergence behavior of MMM.

For both the spring models, N in Eq. (5.4) is chosen to be 2. A zero-force spring length of $r_0 = 1$ is assumed for the first-nearest neighbor springs and of $\sqrt{3}r_0$ for the second-nearest

neighbor springs. Three different external loads mentioned above are applied to the 2D spring models, respectively.

To study the effect of non-harmonic potentials on the convergence of MMM models in 2D, the Lennard-Jones model employed is the same as the 2D spring models except that the Lennard-Jones (LJ) potential (i.e. $U_{LJ}=4\epsilon[(\sigma/r)^{12}-(\sigma/r)^6]$, where r is the interatomic distance) with potential parameters $\sigma=\epsilon=1$ and the second nearest neighbor interaction is used. The atoms are placed initially with interatomic distance $r_0=2^{1/6}\sigma$. Three different types of external loads mentioned above are also applied to the 2D LJ model, respectively.

In all the tests below, the 2D atomic beams are fixed at the left upper and lower corner in x direction and in the middle of the left edge in y direction. Let h_x and h_y denote the element size in x and y direction, respectively, where the normalized element size is calculated by $h = \sqrt{h_x^2 + h_y^2}/r_0$. Ten different combinations of (h_x, h_y) are considered in the 2D convergence study. Figure 5.7 shows a model with the combination of $(24r_0, 6\sqrt{3}r_0)$ for scheme 1p0s.

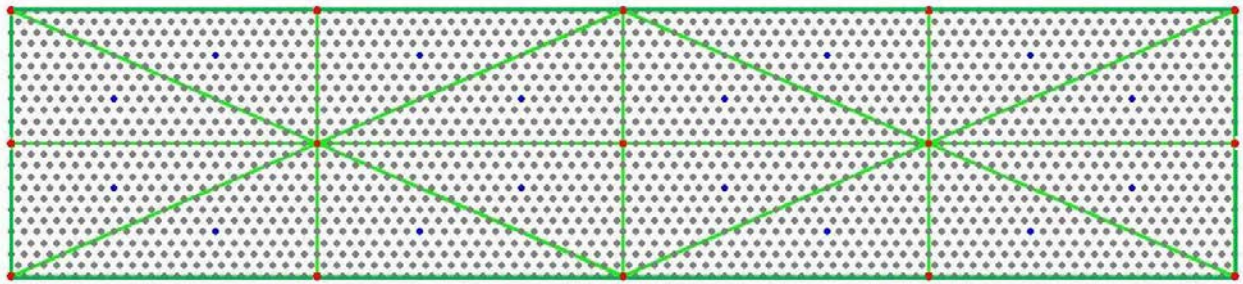


Figure 5.7: 2D mesh with uniform element size $h_x = 24r_0$ and $h_y = 6\sqrt{3}r_0$ for scheme 1p0s: interpolating rep-atoms, primary sampling atoms, non-sampling atoms are represented as red, blue and gray dots, respectively.

5.1.2.1 Atomic spring beam with the corresponding quadratic-deformation force loading

The quadratic-deformation loads will generate a quadratic displacement field for both the U_{s1} -spring and U_{s2} -spring model, respectively, motivated by a commonly used continuum beam model in 2D to test the convergence of FEM and meshfree methods. The continuum beam model (Figure 5.8) is fixed at the left upper and lower corners in x direction and at the middle of the left edge in y direction. The external force P is distributed as a parabola at the right end of the beam. In this study, with the parameters $P = 1000$, $E = 3 \times 10^5$, $\nu = 0.3$ and $I = \frac{D^3}{12}$, the analytical displacement solution is given by [124]:

$$u(x, y) = -\frac{P}{6EI} \left[(6L - 3x)x + (2 + \nu) \left(y^2 - \frac{D^2}{4} \right) \right] \quad (5.6)$$

$$v(x, y) = -\frac{P}{6EI} \left[3\nu y^2 (L - x) + (4 + 5\nu) \frac{D^2 x}{4} + (3L - x)x^2 \right] \quad (5.7)$$

where L and D are the length and height of the beam, respectively

To generate the deformation given by Eq. (5.6) and (5.7) for the 2D atomistic spring beams, the same three steps employed in the corresponding 1D case are also employed here with the same boundary conditions employed in the continuum beam bending model. The enforcement of quadratic deformation for the 2D atomistic LJ beam is achieved in the same manner.



Figure 5.8: A 2D beam commonly employed in solid mechanics to test the convergence of FEM

As can be seen from Figure 5.9a, Figure 5.9b, Figure 5.9c and Figure 5.9d, all four MMM models converge to molecular statics when the element size coincides with atomic spacing (the zero-error point is not shown in the log-log plot) for both spring models. As expected, scheme 0p*s gives the most accurate results. For the U_{s1} -spring model, the convergence in the energy error norm is more linear compared to that in the displacement error norm. If the curves are linearized with respect to all the points in Figure 5.9a and Figure 5.9b, respectively, scheme 0p*s gives a convergence order of 2.022 ($R^2 = 0.9602$) in the displacement error norm and an order of 1.136 ($R^2 = 0.9965$) in the energy error norm. For the U_{s2} -spring model, if the curves are linearized with respect to the last four points in Figure 5.9c and Figure 5.9d, respectively, it shows a linear convergence with a slope of 1.357 ($R^2=0.9979$) in the displacement error norm and with a slope of 1.164 ($R^2=0.9993$) in the energy error norm, which is different from what is observed in the corresponding 1D spring case. This shows the effect of non-constant stiffness matrix on the convergence of MMM. However, it is worth to note that the convergence curves (Figure 5.9a and Figure 5.9b) with MMM are still not the same as typical FEM convergences curves for linear problems in continuum mechanics. In fact the U_{s1} -spring model with the nearest neighbor interaction ($N=1$ in Eq. (5.4)) is also studied and it produces

similar convergence curves as with the $N = 2$ case. Note that even though only the first nearest neighbor interaction is considered, the constitutive description for atomistic models is still nonlocal. The difference between the convergence of MMM and FEM may be due to the fact that the interatomic interaction is nonlocal in nature; however, the constitutive laws for typical continuum problems are local.

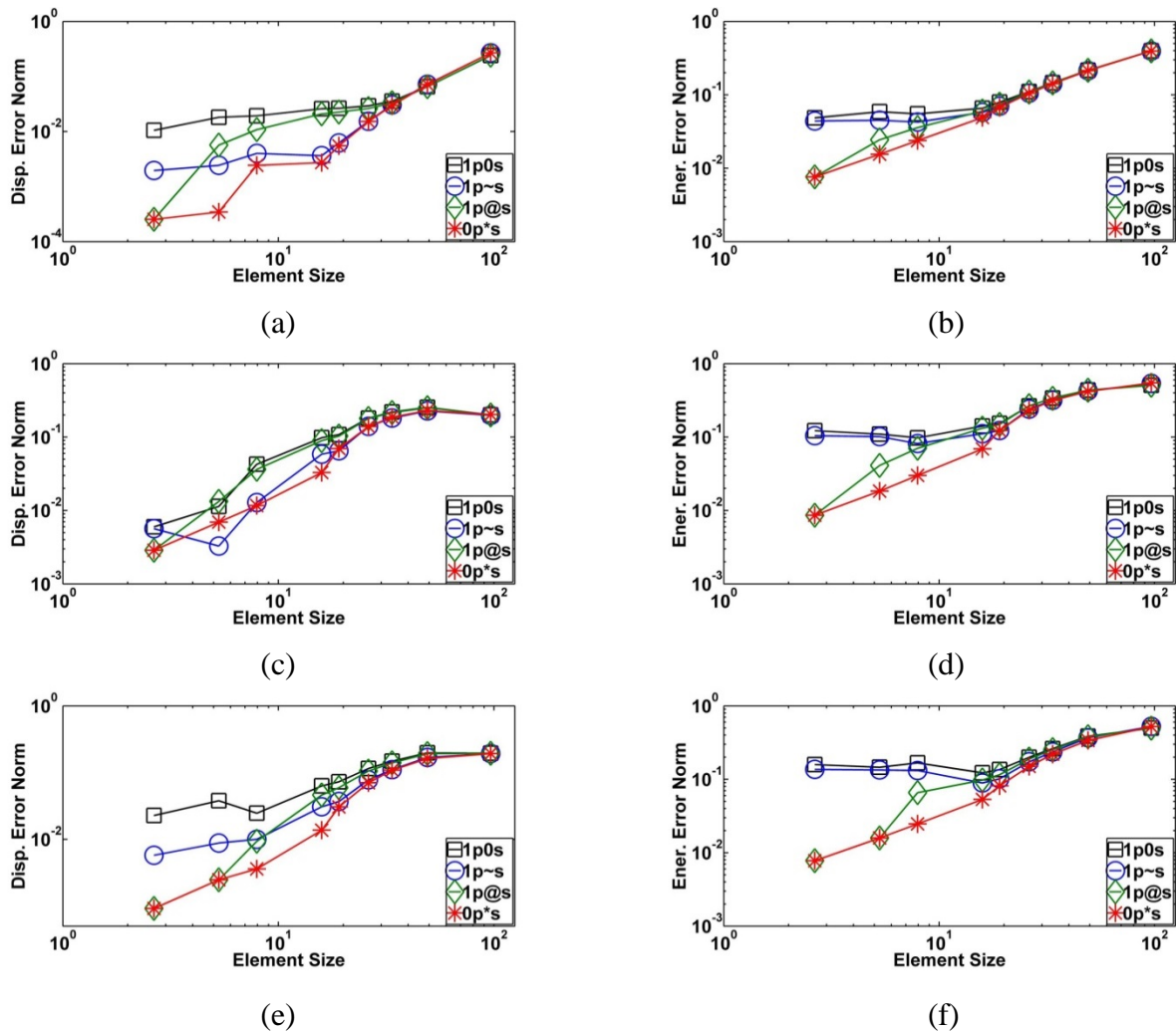


Figure 5.9: Convergence of the 2D U_{s1} -spring model subject to the corresponding quadratic-deformation force loading in the relative displacement error norm (a) and the relative energy

error norm (b); convergence of the 2D U_{s2} -spring model subject to the corresponding quadratic-deformation force loading in the relative displacement error norm (c) and the relative energy error norm (d); convergence of the 2D LJ model subject to the corresponding quadratic-deformation force loading in the relative displacement error norm (e) and the relative energy error norm (f)

5.1.2.2 Atomic LJ beam with the corresponding quadratic-deformation force loading

The same quadratic deformation field used in the 2D spring models is employed where all pair distances between nearest neighbors are within the convex region. Figure 5.9e and Figure 5.9f demonstrate convergence in displacement error norm and energy error norm defined above, respectively. When the element size decreases to certain point, it shows a linear convergence with a slope of 1.48 ($R^2=0.9849$) in the displacement error norm and with a slope of 1.074 ($R^2=0.9996$) in the energy error norm, which is different from what is observed in the corresponding 1D LJ case.

In Figure 5.9, as a whole, MMM shows similar convergence trend for both the U_{s2} -spring and LJ models, as is observed in the 1D case; however MMM with the U_{s1} -spring shows an overall more linear convergence curves. Note that the discrepancy between different schemes is small for elements of larger sizes and is larger for elements with some small sizes and that the errors may increase slightly with scheme 1p0s and 1p~s for certain element sizes. We will explain this observation in the next section from the point of view of error structure analysis.

In the following two different loadings cases and the error structure analysis in Section 5.2, it is found that both U_{s1} and U_{s2} springs show similar behaviors. Since U_{s1} is also fictitious, the results from the U_{s1} -spring model is not presented.

5.1.2.3 Atomic beams with uniformly distributed force loadings: spring and LJ potentials

A uniformly distributed force loading $f_x=0.00005$ and $f_y = -0.00005$ in x and y directions, respectively, are applied to the 2D atomic U_{s2} -spring beam.

A uniformly distributed force loading $f_x = 0.0001$ and $f_y = -0.0001$ in x and y directions, respectively, are applied to the 2D atomic LJ beam.

In Figure 5.10, compared with Figure 5.9, less linear convergence is observed for any of the schemes when the element size is small and the discrepancy between different schemes is relatively smaller. This shows the effect of displacement smoothness on the convergence of MMM models. As in Figure 5.9 in the quadratic-deformation loading case for both models, MMM shows similar convergence trend. Similar to the results shown in Figure 5.5 in the corresponding 1D case, for both the 2D U_{s2} -spring and LJ models, all the four MMM models converge to molecular statics as the element size approaches the atomic spacing, monotonically. What is different from Figure 5.5 is that the convergence rate increases as the element size decreases. We will explain this in Section 5.2.

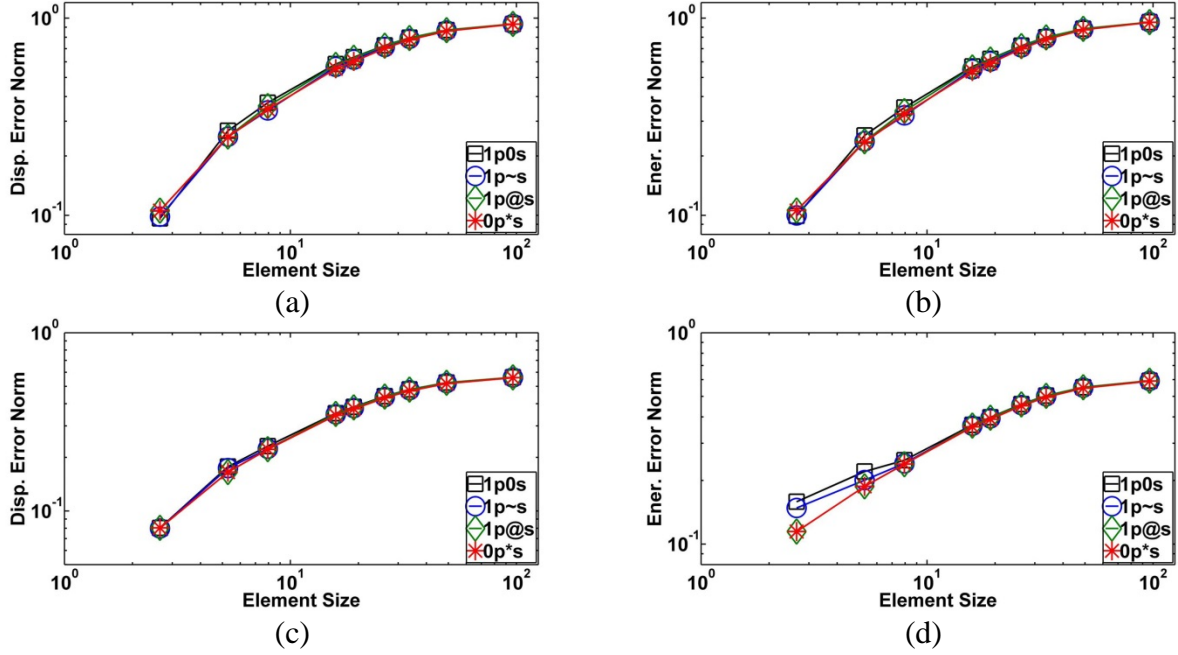


Figure 5.10: Convergence of 2D U_{s2} -spring model subject to the corresponding uniformly distributed force loading in the relative displacement error norm (a) and the relative energy error norm (b); convergence of 2D LJ model subject to the corresponding uniformly distributed force loading in the relative displacement error norm (c) and the relative energy error norm (d)

5.1.2.4 Atomic beams with random force loadings of uniform distribution: spring and LJ potentials

A random force loading with uniform distribution is applied to the atomic U_{s2} -spring beam. The mean value of the random load f_x and f_y are equal to the ones in the second loading to the U_{s2} -spring model in x and y directions, respectively.

A random force loading with uniform distribution is applied to the atomic LJ beam. The mean value of the random load f_x and f_y are equal to the ones in the second loading to the LJ model in x and y directions, respectively.

Figure 5.11 shows the convergence of MMM schemes for the respective 2D U_{s2} -spring and LJ models. Compared with Figure 5.10, MMM behaves similarly. Thus, the analysis in the uniformly distributed loading case holds here.

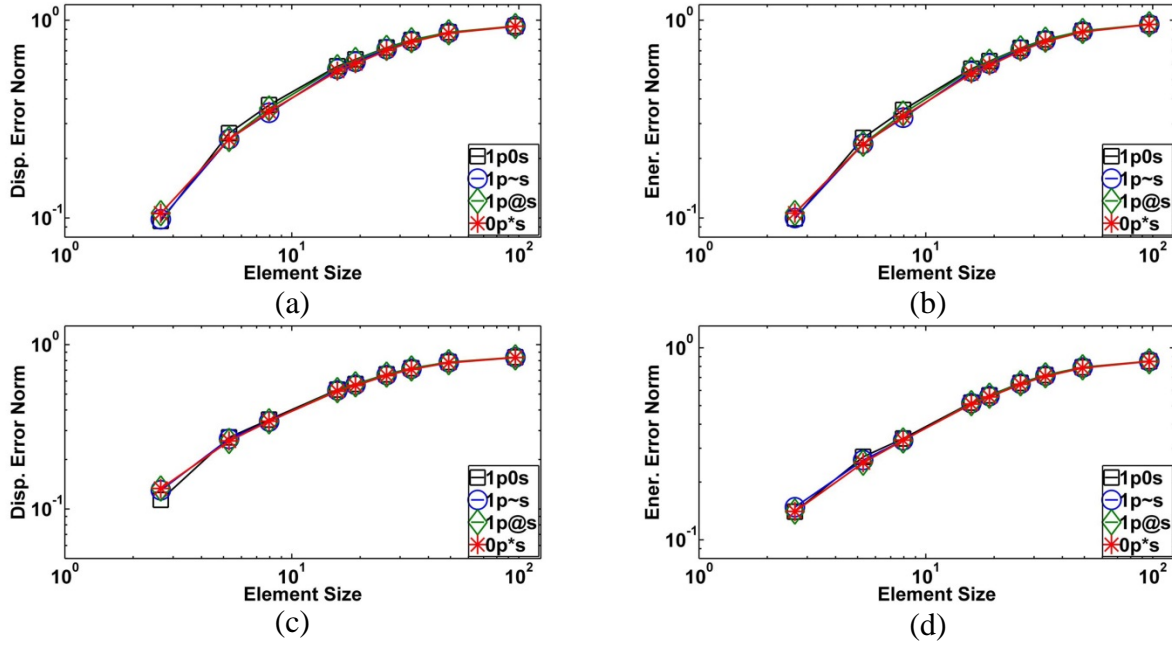


Figure 5.11: Convergence of 2D U_{s2} -spring model subject to the corresponding random force loading of uniform distribution in the relative displacement error norm (a) and the relative energy error norm (b); convergence of 2D LJ model subject to the corresponding random force loading of uniform distribution in the relative displacement error norm (c) and the relative energy error norm (d)

5.2 ERROR STRUCTURE ANALYSIS

In Section 5.1, we have observed that the smoothness of the solution has a larger effect on the convergence performance of MMM schemes than the nonlinearity of interatomic interaction, since MMM demonstrates similar performance for both U_{s2} -spring models and LJ models in general. We also have observed the discrepancy between different MMM schemes. In this section, we will explain the performance of scheme 1p0s, 1p~s and 1p@s for each case studied in Section 5.1 from the results of an error structure analysis.

The error structure analysis is performed based on the error decomposition defined in Section 3.1. The discretization and sampling errors for each tested case in Section 5.1 are quantified by the defined displacement and energy norms in Section 3.2. As mentioned earlier, the discretization error is determined by Scheme 0p*s and is fixed for a given discretization. The performance of a sampling scheme depends on the sampling error introduced. For Scheme 1p0s, 1p~s and 1p@s, the total errors, discretization errors and sampling errors will be presented in the same plot.

5.2.1 Error structure analysis of 1D atomic models

5.2.1.1 Quadratic-deformation loadings

Figure 5.12 and Figure 5.13 show the errors structures of scheme 1p0s ((a) and (b)), 1p~s ((c) and (d)) and scheme 1p@s ((e) and (f)) for the respective 1D spring and LJ models with the corresponding quadratic-deformation force loading. It can be seen that the respective discretization errors in displacement and energy error norms converge at a respective constant rate of 2 and 1 for each scheme. However, the sampling error for each scheme has different trends.

For scheme 1p@s, the sampling error stays almost constant and the discretization error is at least 5 orders larger in magnitude. In Figure 5.12e and Figure 5.12f, the sampling error is numerically zero for scheme 1p@s. This is why scheme 1p@s shows similar results with scheme 0p*s. This is consistent with our expectation since scheme 1p@s has more secondary sampling atoms around the interpolating rep-atoms and thus has less sampling error based on the error definition above. However, for scheme 1p0s and 1p~s, the sampling errors may increase. When the element size is large, the discretization error dominates the sampling error for all the schemes and that when the element size is reduced below certain point, the sampling error may be larger compared to the discretization error for scheme 1p0s and 1p~s. This is why the convergence rate changes and the discrepancy between different schemes occurs. Note that all the schemes converge to molecular statics where sampling error drops to zero (the zero-error points are not shown).

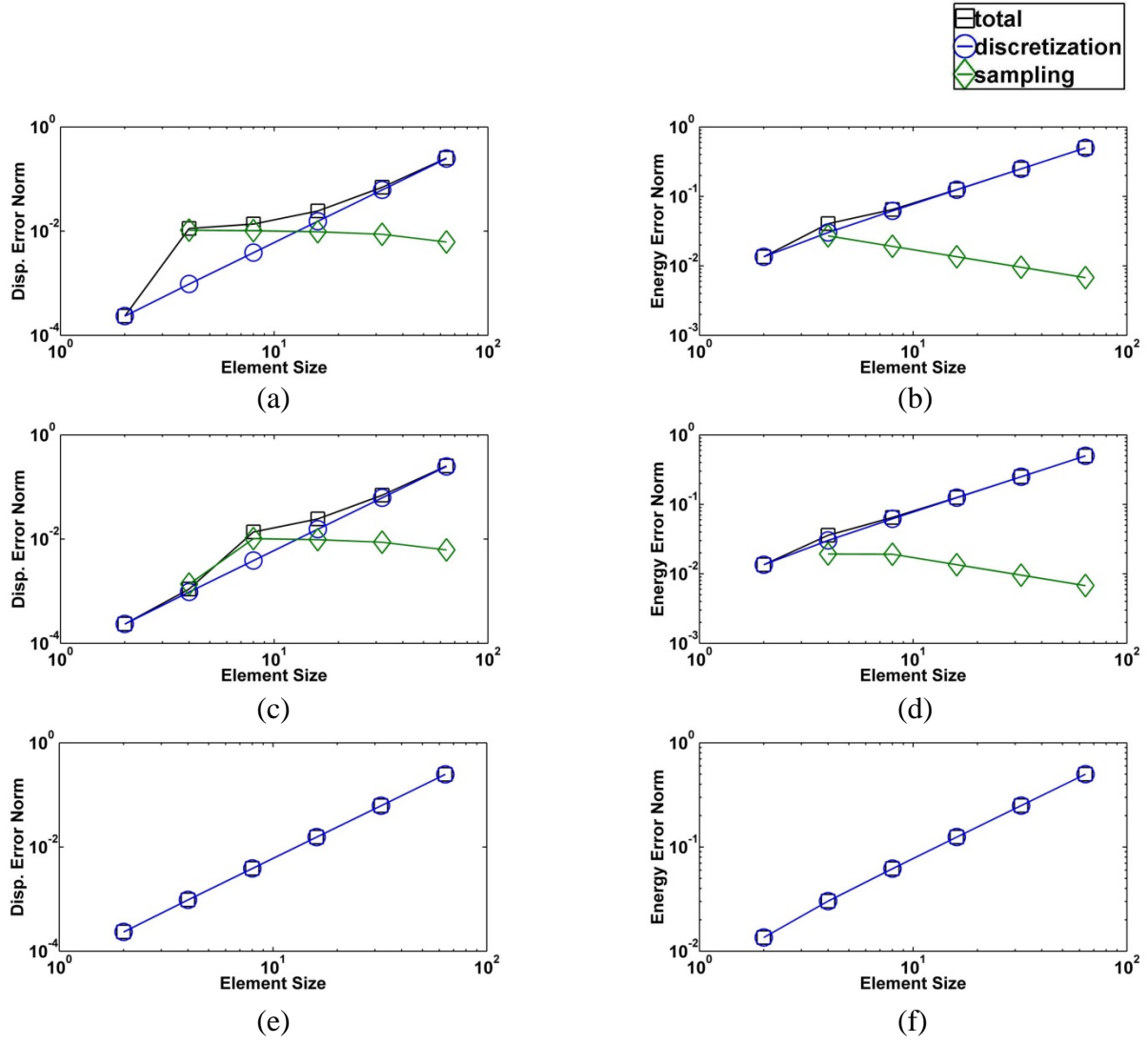


Figure 5.12: Error structure analysis of scheme 1p0s ((a) and (b)), 1p~s ((c) and (d)) and 1p@s ((e) and (f)) for the 1D spring model with the corresponding quadratic-deformation force loading

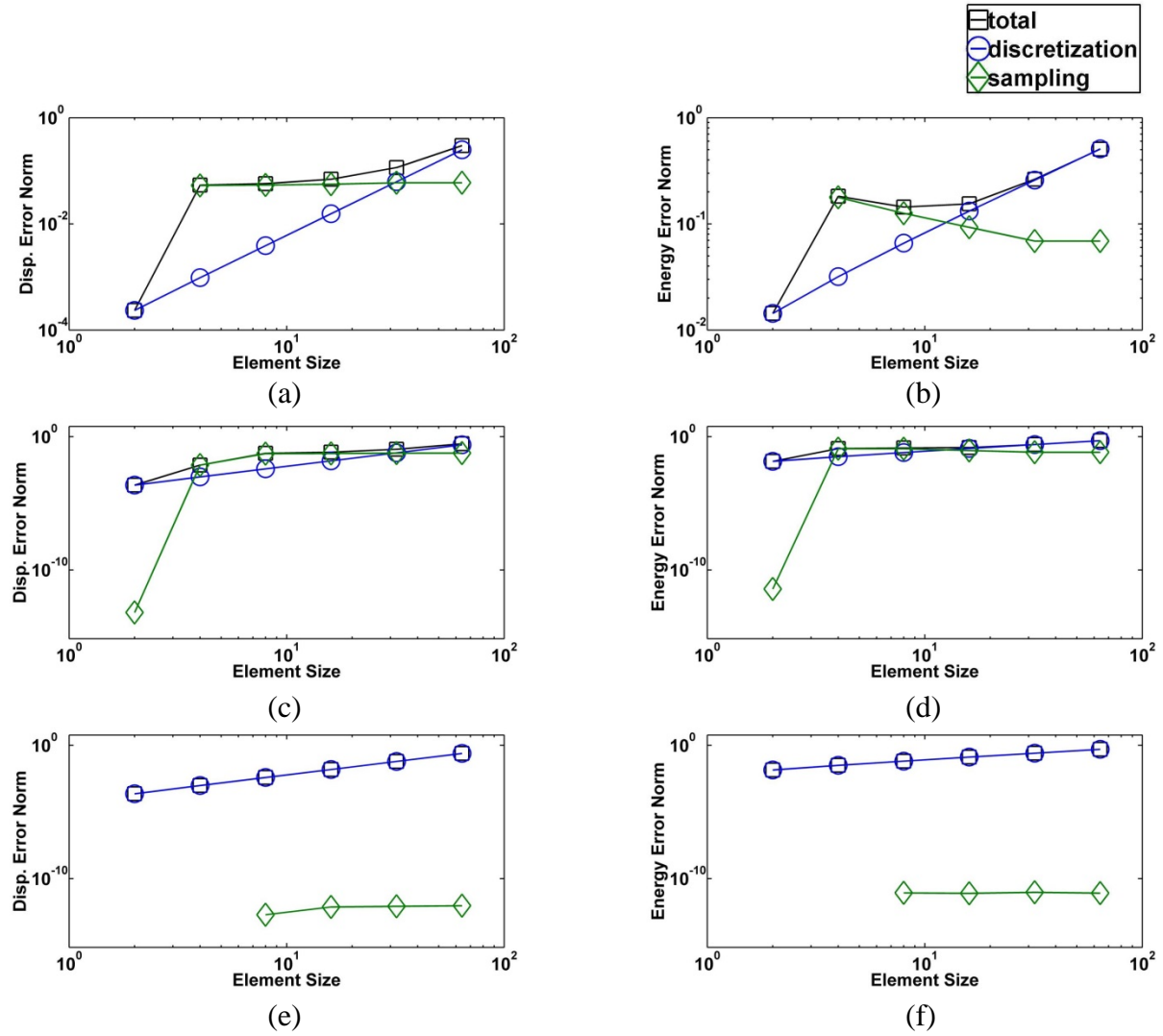


Figure 5.13: Error structure analysis of scheme 1p0s ((a) and (b)), 1p~s ((c) and (d)) and 1p@s ((e) and (f)) for the 1D LJ model with the corresponding quadratic-deformation force loading

5.2.1.2 Uniformly distributed force loadings

Figure 5.14 and Figure 5.15 show the error structure of scheme 1p0s ((a) and (b)), 1p~s ((c) and (d)) and scheme 1p@s ((e) and (f)) for the 1D spring and LJ models with the uniformly distributed force loadings, respectively. Note that the resulted displacement fields are less smooth.

The respective discretization errors in displacement and energy error norms converge at a decreasing order. For scheme 1p@s, as what has been observed in Figure 5.12 and Figure 5.13 in the 1D quadratic-deformation force loading case, the sampling error is, at least 5 orders smaller than the discretization error (LJ model) or even zero numerically (spring model) for the same element size. For scheme 1p0s and 1p~s, the discretization error dominates in the case of larger element sizes, but for elements of certain small sizes, the sampling error may be larger. However, since the decrease of discretization error is larger than the increase of sampling error, the total error still drops for these small element sizes. Thus, for elements of large sizes, discretization error is of main concern.

By comparing Figure 5.12 and Figure 5.14 as well as Figure 5.13 and Figure 5.15, the errors are relatively larger and decrease slower with the same element size for the less smooth displacement field, compared with the quadratic deformation field. The reason for this is because using interpolation to approximate smooth functions is more accurate than to approximate less smooth functions, with the same number of degrees of freedom and shape functions. This comparison shows the effects of smoothness of the displacements on the error structures of MMM schemes in 1D.

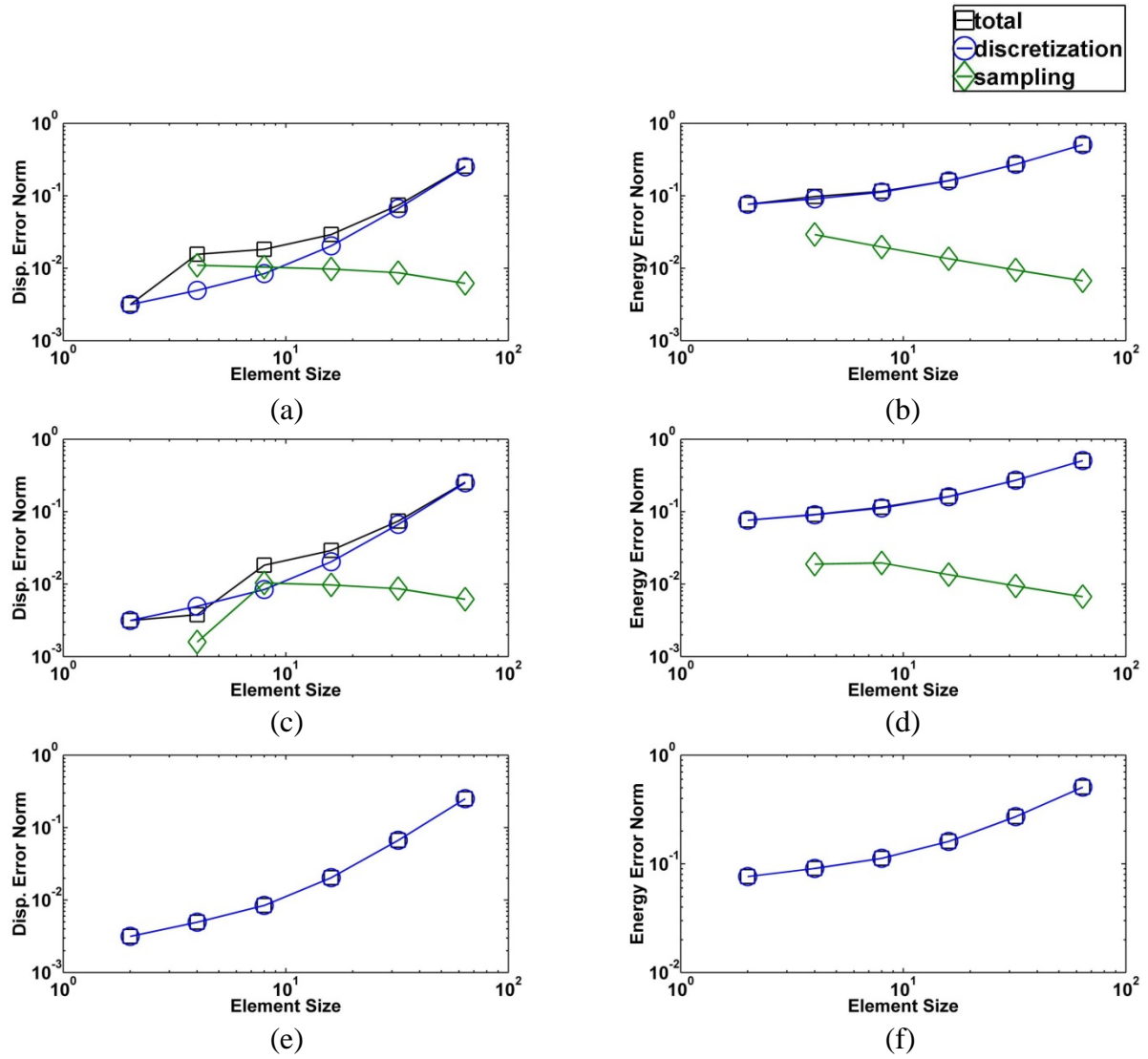


Figure 5.14: Error structure analysis of scheme 1p0s ((a) and (b)), 1p~s ((c) and (d)) and 1p@s ((e) and (f)) for the 1D spring model with the corresponding uniformly distributed force loading

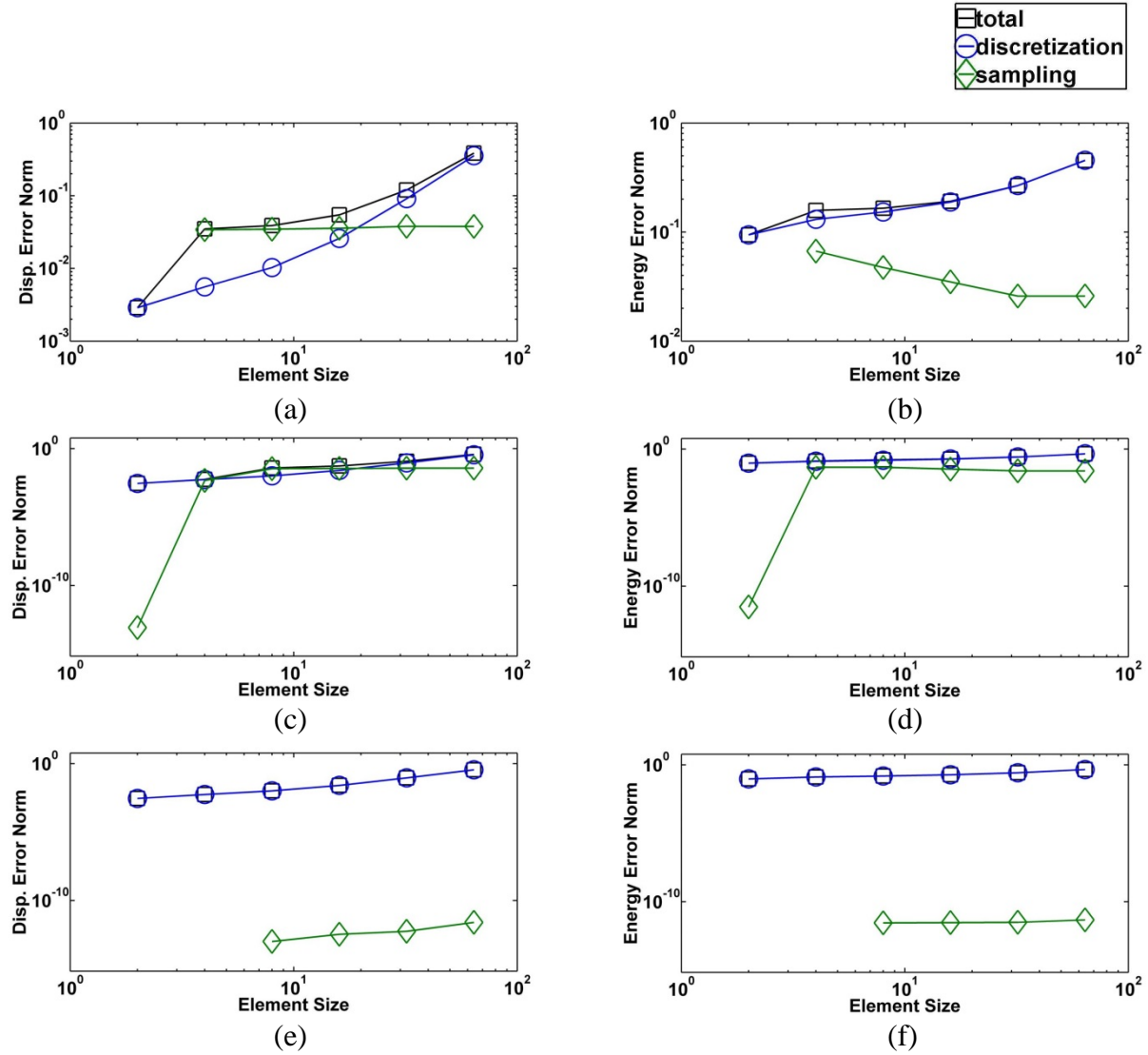


Figure 5.15: Error structure analysis of scheme 1p0s ((a) and (b)), 1p~s ((c) and (d)) and 1p@s ((e) and (f)) for the 1D LJ model with the corresponding uniformly distributed force loading

5.2.1.3 Random force loadings of uniform distribution

Figure 5.16 and Figure 5.17 show the error structures of scheme 1p0s ((a) and (b)), 1p~s ((c) and (d)) and scheme 1p@s ((e) and (f)) for the 1D spring and LJ models with the corresponding random force loadings of uniform distribution, respectively. It can be seen that similar performance of MMM is observed when compared to the one in Figure 5.14 and Figure

5.15 in uniformly distributed loading case. Thus, the analysis in sub-Section 5.2.1.2 is applicable. Note that the displacement fields have similar smoothness for the uniformly distributed loading and random loading of uniform distribution. This means that similar displacement smoothness will lead to similar error structure with MMM in 1D.

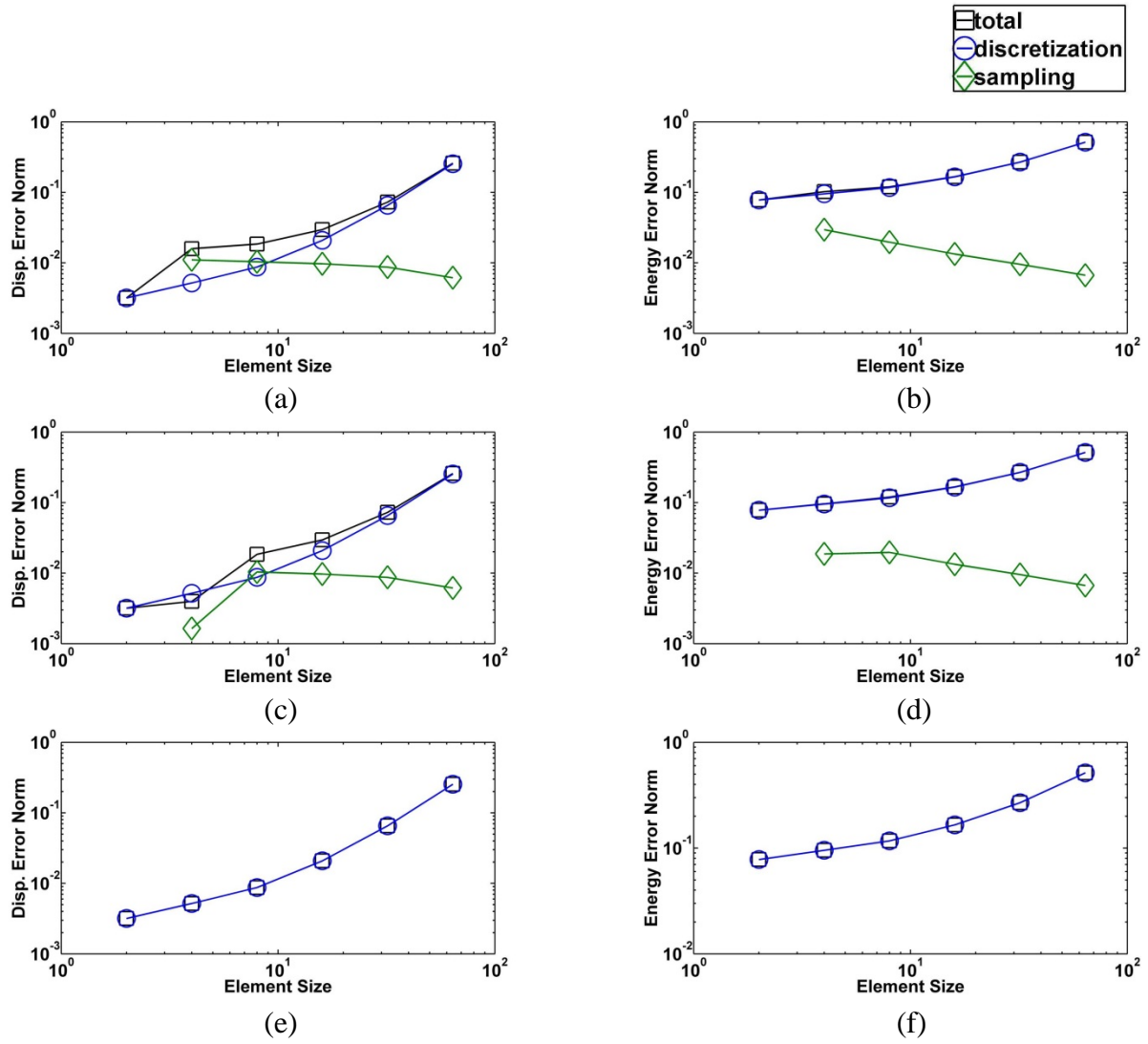


Figure 5.16: Error structure analysis of scheme 1p0s ((a) and (b)), 1p~s ((c) and (d)) and 1p@s ((e) and (f)) for the 1D spring model with the corresponding random force loading of uniform distribution

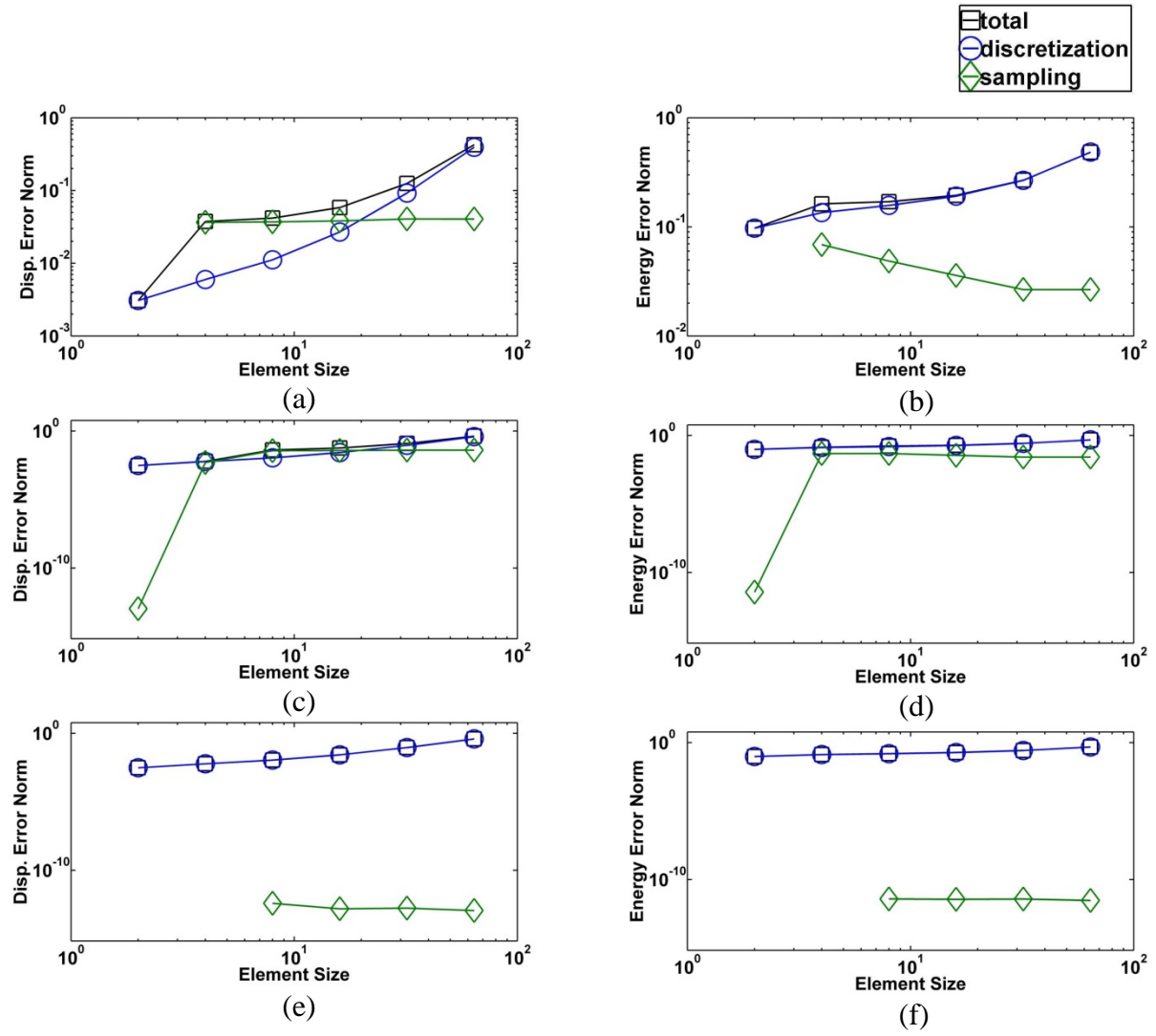


Figure 5.17: Error structure analysis of scheme 1p0s ((a) and (b)), 1p~s ((c) and (d)) and 1p@s ((e) and (f)) for the 1D LJ model with the corresponding random force loading of uniform distribution

5.2.2 Error structure analysis of 2D atomic models

5.2.2.1 Quadratic-deformation loadings

Figure 5.18 and Figure 5.19 show the error structures of scheme 1p0s ((a) and (b)), 1p~s ((c) and (d)) and scheme 1p@s ((e) and (f)) for the respective 2D U_{s2} -spring and LJ models with the corresponding quadratic-deformation force loadings.

It can be seen that the respective discretization errors in displacement and energy error norm converge at an increasing rate at first and then shows linear convergence when the element size reduces to some point.

The sampling errors for all the three schemes are similar and discretization error dominates for larger element sizes. For scheme 1p0s and 1p~s, when the element size decreases to certain point, the sampling error in energy error norm may increase and the sampling error in displacement error norm may go up or down slightly; however, for scheme 1p@s, the sampling error drops in both displacement and energy error norms. This is because scheme 1p@s is closer to scheme 0p*s for small element sizes, and hence secondary sampling atoms are around each interpolating repatoms to capture the non-local interaction between the elements more accurately. This sampling error distribution for each scheme explains the observation in Section 5.1.2 for the corresponding loading case.

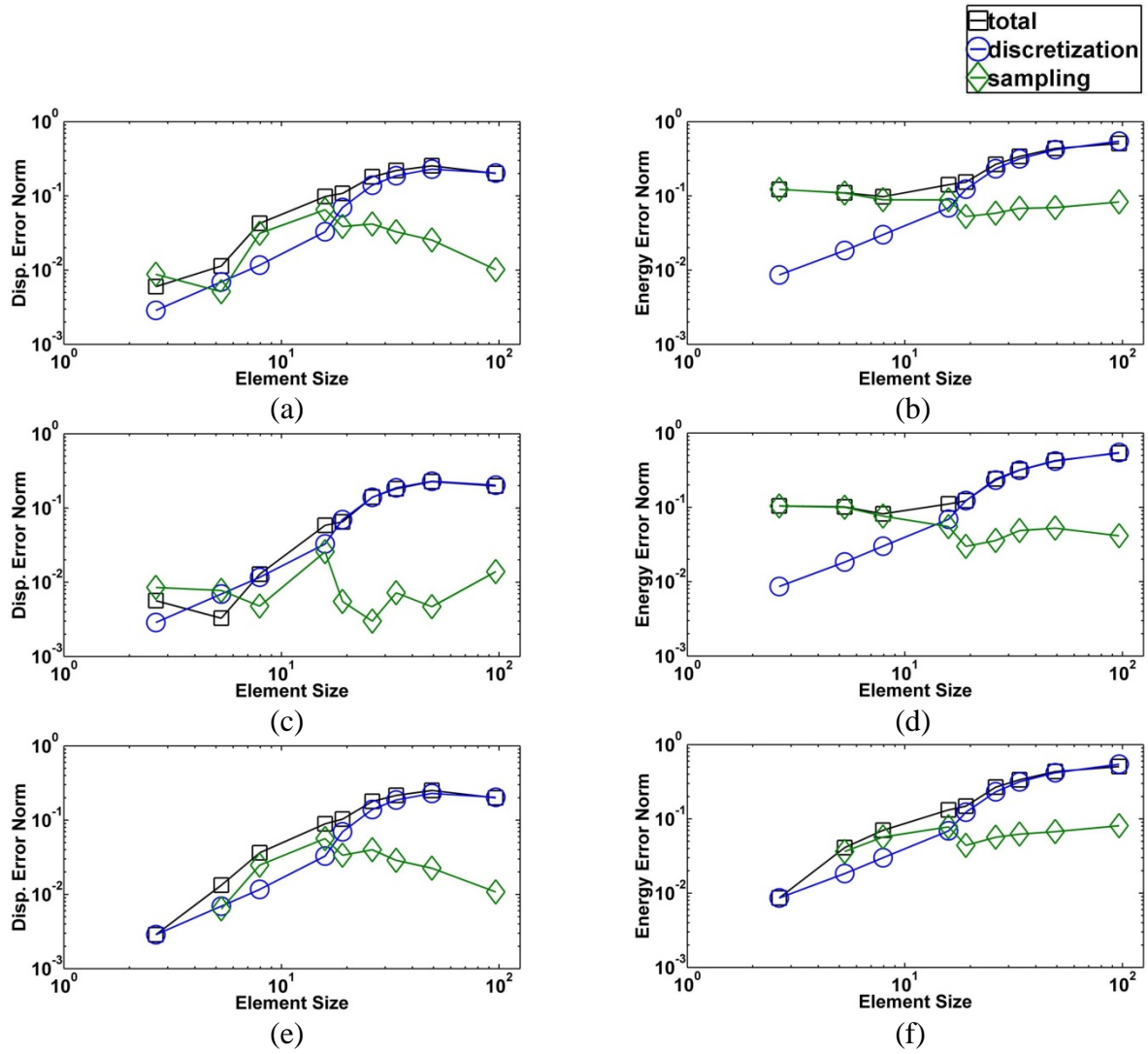


Figure 5.18: Error structure analysis of scheme 1p0s ((a) and (b)), 1p~s ((c) and (d)) and 1p@s ((e) and (f)) for the 2D U_{s2} -spring model with the corresponding quadratic-deformation force loading

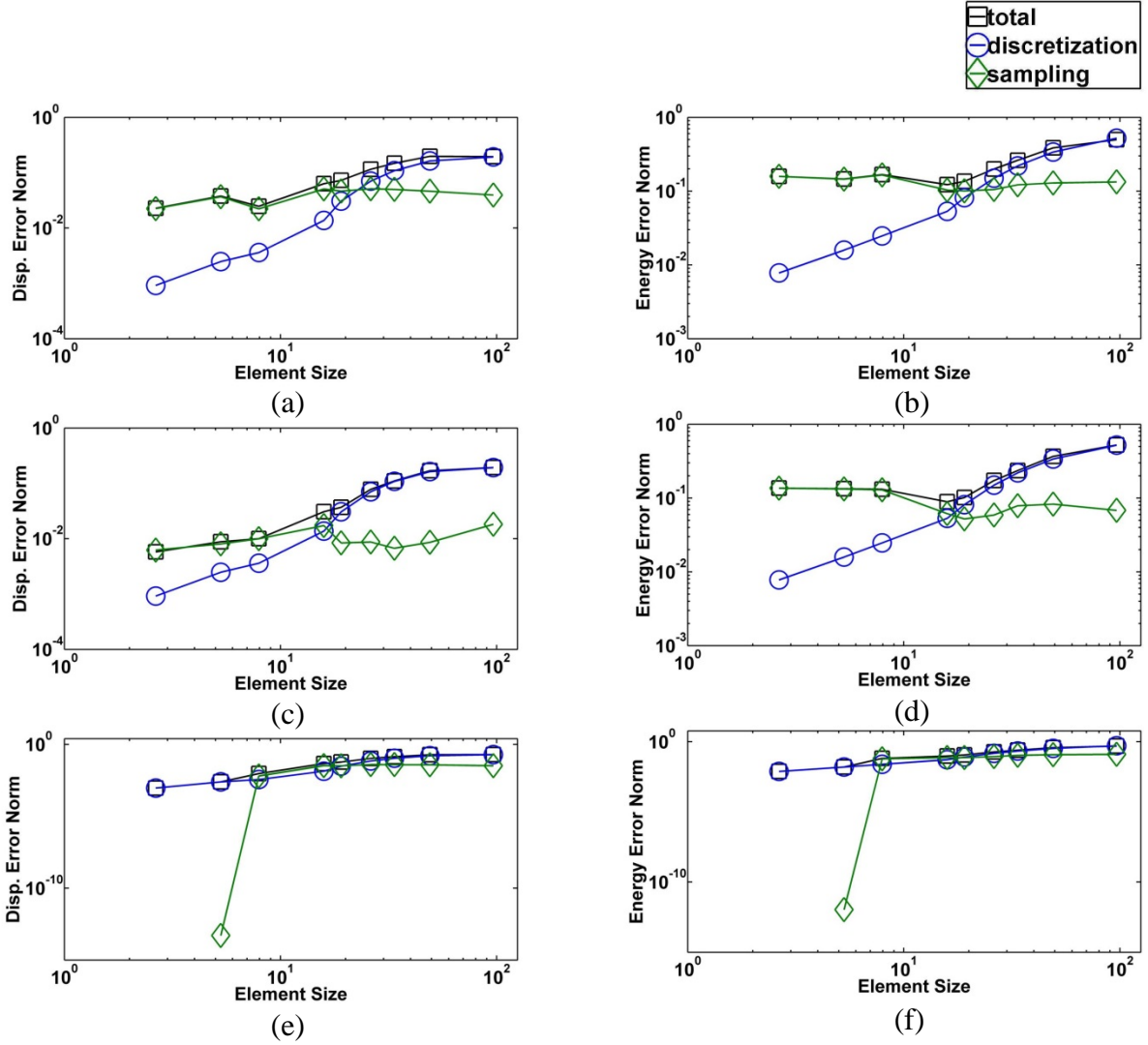


Figure 5.19: Error structure analysis of scheme 1p0s ((a) and (b)), 1p~s ((c) and (d)) and 1p@s ((e) and (f)) for the 2D LJ model with the corresponding quadratic-deformation force loading

5.2.2.2 Uniformly distributed force loadings

Figure 5.20 and Figure 5.21 show the error structures of scheme 1p0s ((a) and (b)), 1p~s ((c) and (d)) and scheme 1p@s ((e) and (f)) for the 2D U_{s2} -spring and LJ models with the uniformly distributed force loadings, respectively. Note that the resulted displacement fields are less smooth.

The respective discretization errors in displacement and energy error norms converge at a slightly increasing rate, which is different from the corresponding 1D case where the discretization errors converge at a slightly decreasing rate. It is clearly shown that the discretization error dominates sampling error for all the schemes over all element sizes. Thus, the sampling errors play a less important role and discretization error becomes the main concern. In fact, the sampling errors for all the three schemes are similar for larger element sizes and there is a slight difference when the element size is small. Thus, overall, the performance of each scheme is similar or the discrepancy between different schemes is small, which is consistent with the observation from the corresponding loading case in Section 5.1.2.

From the comparison of Figure 5.18 and Figure 5.20 and the comparison of Figure 5.19 and Figure 5.21, it can be seen that the sampling errors are relative smaller or at the same order and the discretization error are relatively larger with the same element size for the less smooth displacement field, compared with the quadratic deformation field. As explained in the corresponding 1D case, using interpolation to approximate functions of higher smoothness is more accurate with the same number of degrees of freedom and shape functions. This comparason shows the effect of displacement smoothness on the error structures of MMM schemes in 2D.

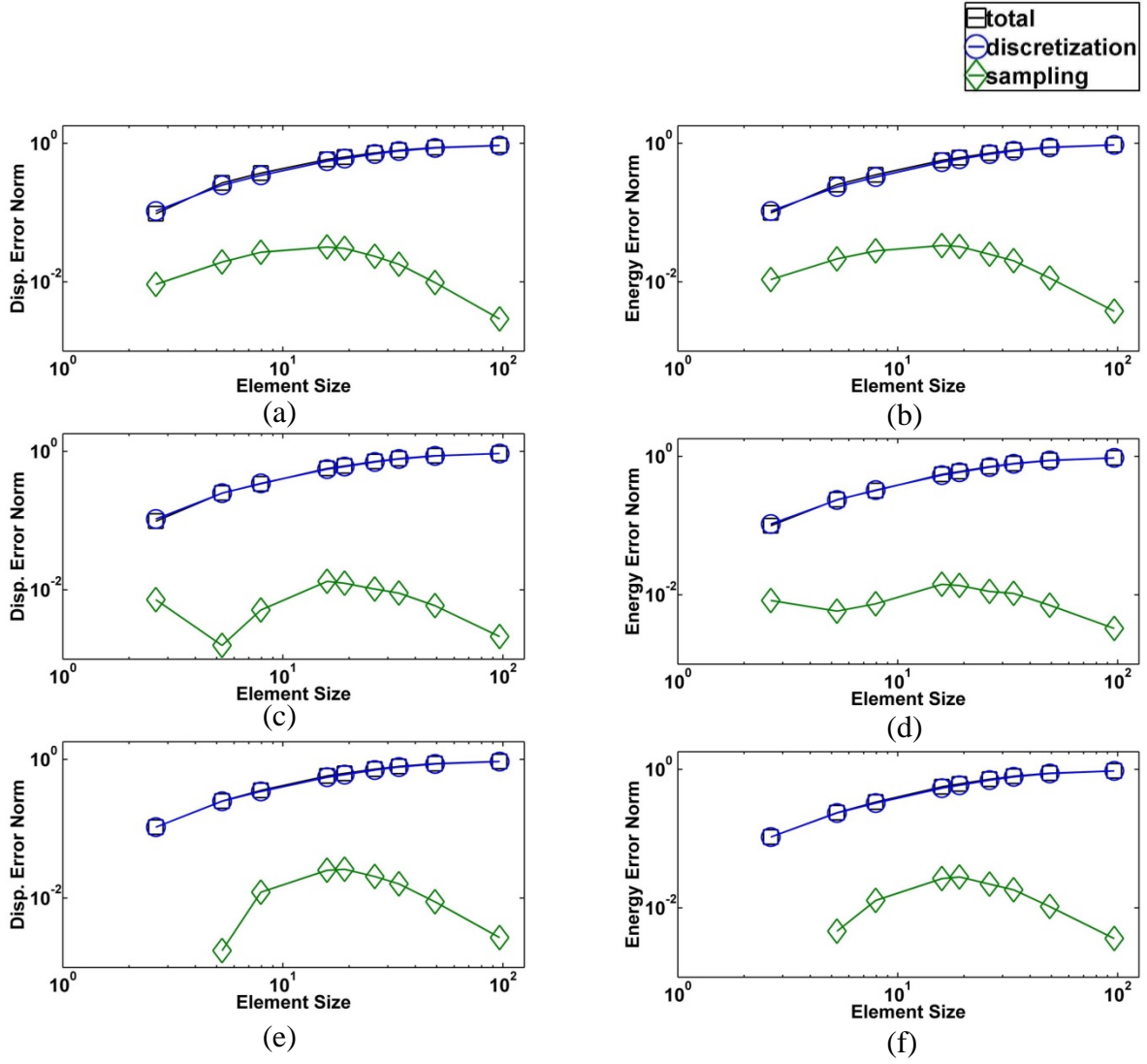


Figure 5.20: Error structure analysis of scheme 1p0s ((a) and (b)), 1p~s ((c) and (d)) and 1p@s ((e) and (f)) for the 2D U_{s2} -spring model with the corresponding uniformly distributed force loading

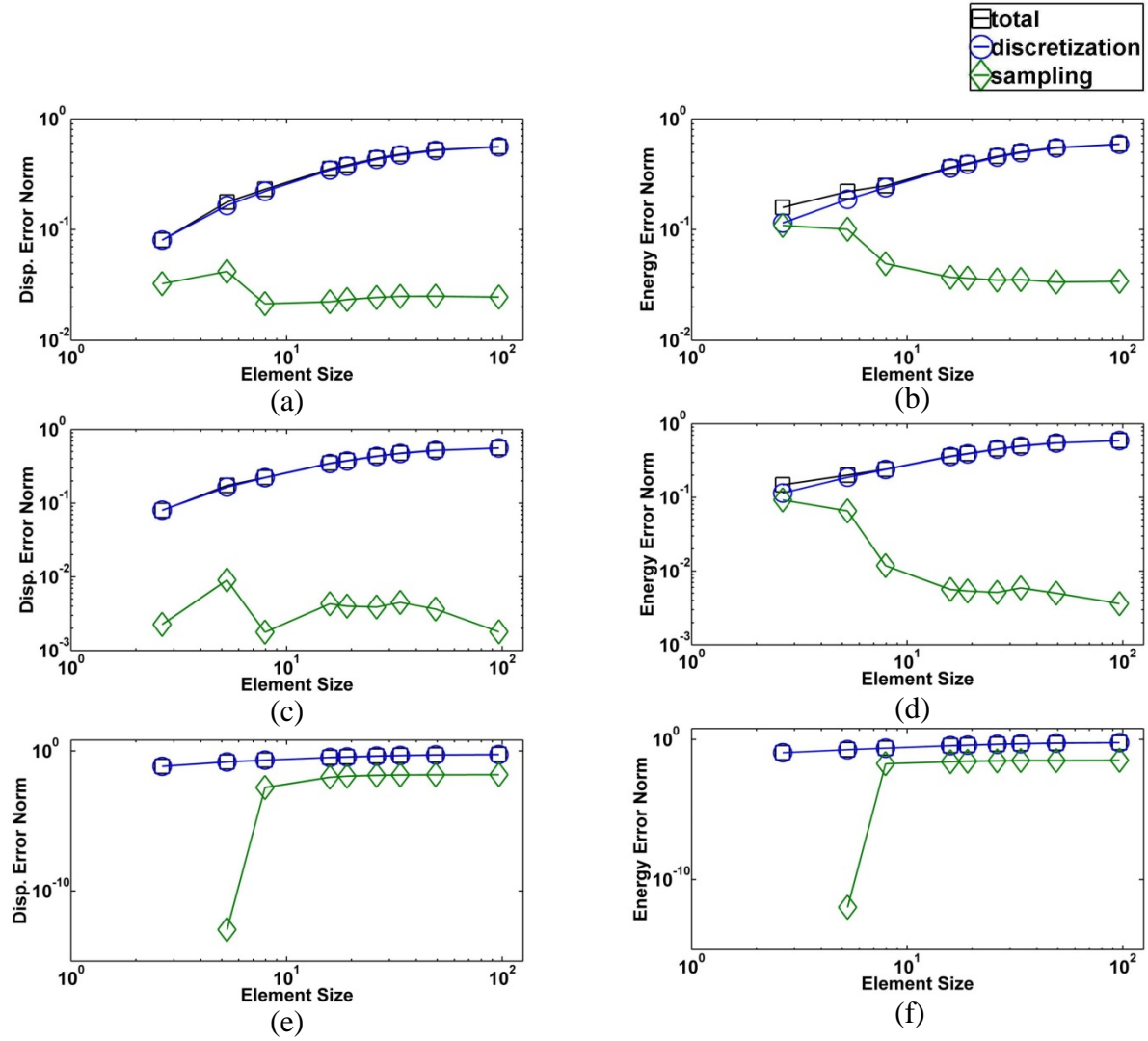


Figure 5.21: Error structure analysis of scheme 1p0s ((a) and (b)), 1p~s ((c) and (d)) and 1p@s ((e) and (f)) for the 2D LJ model with the corresponding uniformly distributed force loading

5.2.2.3 Random force loadings of uniform distribution

Figure 5.22 and Figure 5.23 show the error structures of scheme 1p0s ((a) and (b)), 1p~s ((c) and (d)) and scheme 1p@s ((e) and (f)) for the 2D U_{s2} -spring and LJ models with the corresponding random force loadings of uniform distribution, respectively. As in Figure 5.20

and Figure 5.21 for the uniformly distributed loading case, similar performance of MMM is shown. Thus, the analysis in sub-Section 5.2.2.2 is applicable.

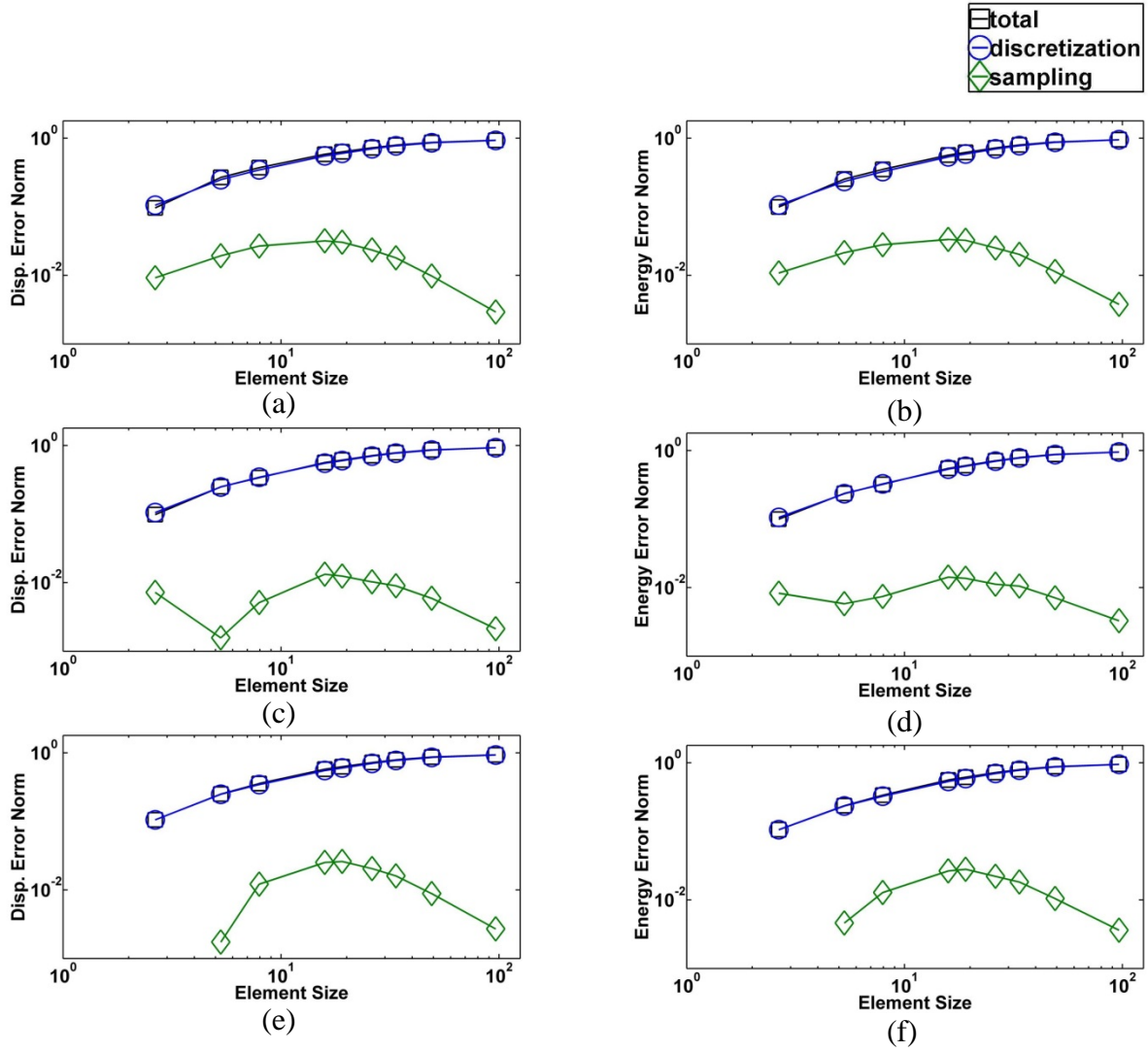


Figure 5.22: Error structure analysis of scheme 1p0s ((a) and (b)), 1p~s ((c) and (d)) and 1p@s ((e) and (f)) for the 2D U_{s2} -spring model with the corresponding random force loading of uniform distribution

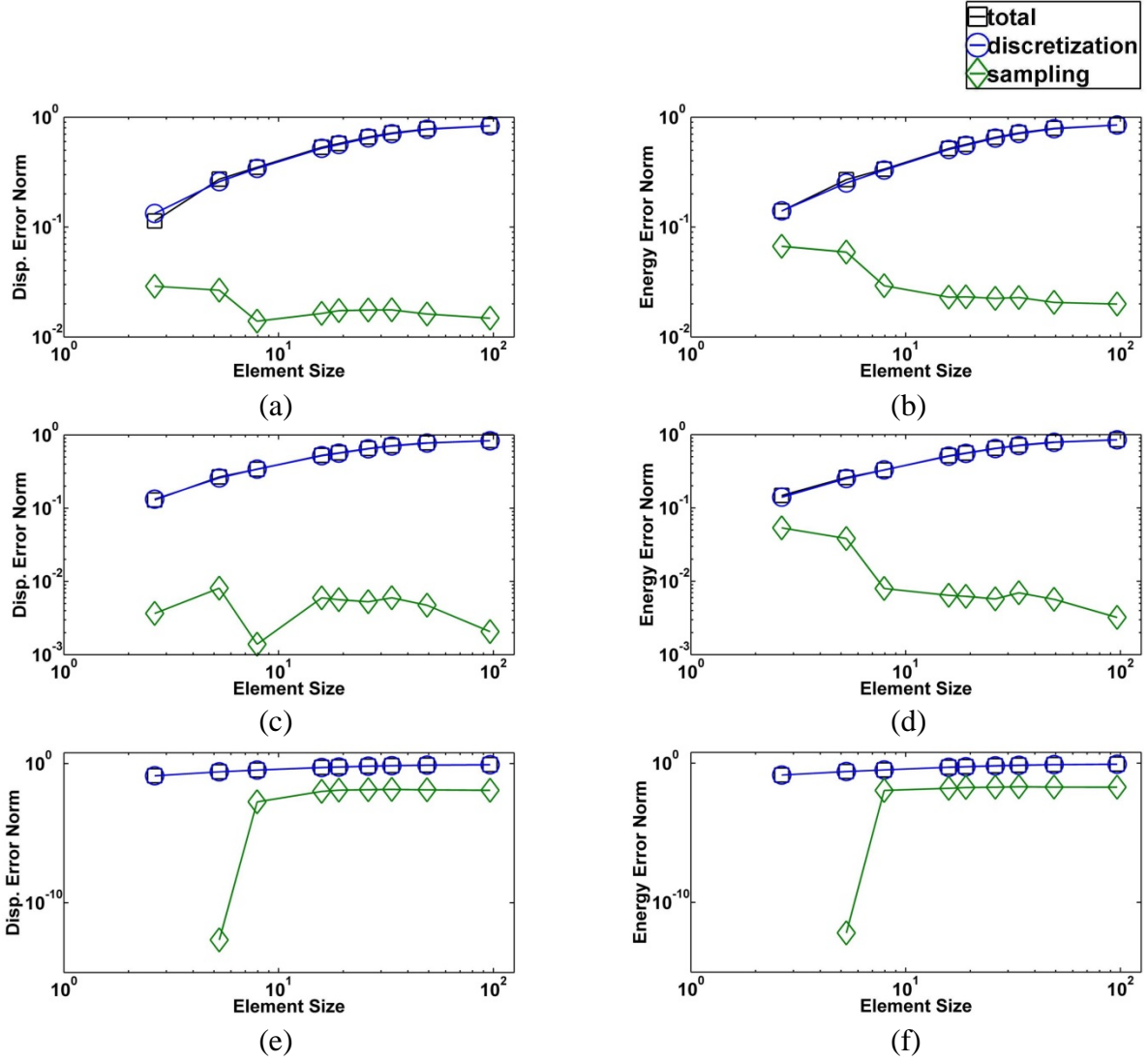


Figure 5.23: Error structure analysis of scheme 1p0s ((a) and (b)), 1p~s ((c) and (d)) and 1p@s ((e) and (f)) for the 2D LJ model with the corresponding random force loading of uniform distribution

5.2.3 An analysis of sampling errors

As can be seen from the 5.2.2, the discretization error decreases when the element size is reduced. This is because more interpolating atoms or more degrees of freedom are added with smaller

element size. Thus, the interpolation by shape functions is more accurate to determine the information of ghost atoms, which is similar to that using smaller element sizes give better accuracy for FEM to solve problems in continuum mechanics. However, the behavior of sampling error for each scheme is more complicated. It may decrease or increase for different element sizes. The sampling error for each scheme is affected in two opposite directions when shrinking element sizes: (1) the number of primary sampling atoms increases with the decrease of element size. Thus the energy of non-sampling atoms in an element that are at least one cutoff distance away from element edges (element bulk atoms) are better represented by the energy of the primary sampling atom within the same element, compared to coarser element sizes; this will increase the accuracy of sampling errors; (2) on the other hand, the number of non-sampling atoms that are within the cutoff distance from element edges (element edge atoms) increase with smaller element size. This introduces larger sampling errors since the assumption that the energy of edge atoms follows the energy distribution of bulk atoms is less valid, as explained in Section 2.3.2. Thus whether the sampling error decrease or increase depends which factor dominates. Note that the sampling error can be minimized or removed by making these non-sampling atoms that are within a cutoff distance away from element edges as secondary sampling atoms. In fact, the number and the distribution of secondary sampling atoms of each scheme determine the performance of that scheme.

It can be concluded from Section 5.1 and Section 5.2 that the sampling error plays a key role in the performance of MMM schemes for a given mesh. As such, the comparison of the sampling errors of MMM schemes for a given mesh will be informative to combine MMM schemes in practice to optimize accuracy and efficiency. Figure 5.24 shows the sampling error comparison of the four MMM schemes in displacement and energy error norm, respectively, for

the representative model and loading case chosen above. Note that the sampling error in scheme 0p*s is zero. In Figure 5.24, when the element size is large ($>10r_0$), the displacement sampling error norms for scheme 1p0s and 1p@s are almost the same and so is the energy sampling error norm. Scheme 1p~s shows better sampling errors with large element sizes because the surface energy is better represented, as the surface ghost atoms are made to be secondary sampling atoms. When the element size is small ($<10r_0$), scheme 1p@s shows good performance. Based on the observation above, for a given mesh, it is suggested that the MMM schemes should be combined in the following ways in optimizaing accuracy and efficiency: (1) scheme 1p0s is employed for elements with larger sizes ($>10r_0$). Since in a multiscale model, large elements dominate the coarse-grained region with small deformation and that only one primary sampling atom is employed in scheme 1p0s, the efficiency of MMM can be imagined; (2) scheme 1p@s is suggested for the elements with an element size that is small ($<10r_0$) in the coarse-grained region.

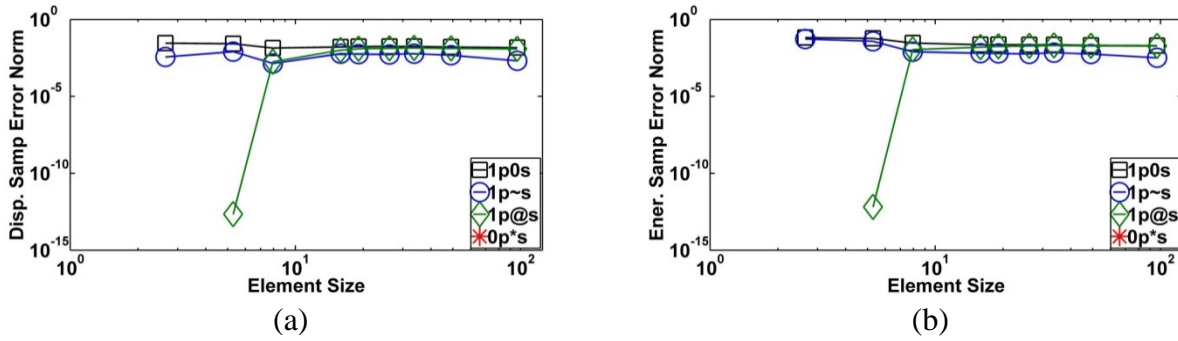


Figure 5.24: Sampling error norm comparasion of the four MMM schemes for the 2D LJ model with the corresponding random force loading of uniform distribution in displacement error norm (a) and energy error norm (b)

The above suggestion is drawn based on the study of the LJ beam model with special element sizes and shapes. Note that the cutoff distance of different potentials and element shapes will affect the two factors mentioned above and thus will affect the sampling error behavior. A more comprehensive study on how the cutoff distance of different potentials and element size and shape affect the sampling error behavior will be left for future research. In addition, the employment of both SR^B and SR^S will be considered for convergence study in 2D and 3D in the future.

5.3 SUMMARY

We have performed numerical convergence study and error structure analysis of four sampling schemes with respect to linear element in the proposed MMM framework. The effects of linearity of the interatomic interaction and smoothness of the displacement field on the convergence characteristics have been studied and analyzed. In particular, we have shown that:

(1) All four sampling schemes, in general, show similar convergence trend for both the spring and LJ models for all the loading conditions in 1D and 2D. The accuracy of each scheme for the spring models is slightly higher than that for the corresponding LJ models. All the MMM schemes tested show similar accuracy for large element sizes under all the loading cases, which demonstrates the effectiveness of the MMM method.

(2) The smoothness of displacement field has a significant impact on the convergence behavior of each sampling scheme, which is similar to past results obtained in convergence study of FEM. Only for the quadratic-deformation force loading case when the resulting displacement field is smooth, the schemes 1p@s and 0p*s demonstrate FEM-like behavior with convergence

orders of 1 and 2 in the displacement and energy error norms, respectively, in 1D and also shows linear convergence property with certain orders in 2D. The discrepancy between the four schemes is relatively larger for more smooth displacement field than that for less smooth deformation.

(3) Under the quadratic-deformation loading case in 2D, the U_{s1} -spring model where the stiffness matrix is constant behaves closer to FEM in terms of convergence behavior. The difference in the convergence property between MMM and FEM may be due to the fact that interatomic interaction is nonlocal in nature; however, the constitutive laws for typical continuum problems are local, which may not show up significantly in the corresponding 1D cases.

(4) The smoothness of displacement field has a significant impact on the error structure of each sampling scheme. For the quadratic-deformation loading when the resulting displacement field is smooth, the discretization errors dominate sampling errors for large element size for all four schemes. The sampling error may dominate discretization error for small element size only for scheme 1p0s and 1p~s. For the other two loading conditions when the deformation is less smooth, the discretization error dominates the sampling errors for each scheme over all the element sizes. For the uniformly distributed loading and the random loading of uniform distribution, the MMM schemes show similar performance when the resulting displacement fields have similar smoothness.

6.0 CONCLUSIONS AND OUTLOOK

6.1 CONTRIBUTIONS

The main achievements of this dissertation are summarized as follows:

(1) Proposed a novel energy-based coarse-grained molecular mechanics, named Multiresolution Molecular Mechanics (MMM), with a novel and general summation rule framework SR^{MMM} that is valid for general interpolation shape functions. The general idea of SR^{MMM} is to analytically derive the energy distribution of coarse-grain atomistic model for harmonical potential. Then the energy distribution is well represented by the energy of selected quadrature-type (sampling) atoms in a curve-fitting-like process. The optimal number, weight and position of sampling atoms are formulated and are shown to be shape-function dependent, similar to, for instance, which order of Gauss quadrature is employed for a given shape function.

(2) Consistently decomposed SR^{MMM} into the bulk summation rule SR^B and the surface summation rule SR^S . Mathematically, this decomposition is based on the observation that the energy distribution of the bulk region is different from that of the surface area. Physically, the energy distribution difference between the bulk and surface regions is caused by the fact that surface atoms are not fully-coordinated and are lack of bonding neighbors compared to their bulk counterpart. The optimal number, weight and position of sampling atoms for the

respective SR^B and SR^S are exactly same as proposed in the general framework SR^{MMM} . The only difference is that SR^B and SR^S are employed for bulk and surface regions, respectively.

(3) Clearly identified and rigorously quantified different error sources, i.e. discretization and sampling errors, by novel error norms inspired by the corresponding counterparts in continuum mechanics. The discretization error is related to the element size and the order of employed shape functions, as in FEM. The sampling error only depends on the summation rule employed, similar to the numerical integration error introduced with each quadrature rule. Since discretization is fixed for a given discretization, the sampling error has to be minimized in order to minimize the total error. As such, the defined sampling error norms can be selected as a key indicator to quantify the performance of a proposed summation rule.

(4) Numerically validated and compared the designed bulk summation rule SR^B and its extension to nonlinear (Lennard-Jones) potential with other summation rules such as Gauss-quadrature-like rule, where SR^B demonstrates its effectiveness in terms of accuracy and computational cost. The validation and comparison are firstly performed with respect to harmonic spring potential in 1D and 2D by employing linear, bilinear and quadratic elements to solve tensile, shear and bending deformations. Then the standard Lennard-Jones potential is employed to show the validity of SR^B for nonlinear potentials. The success of SR^B for nonlinear potential lies in the fact that any nonlinear potential can be well approximated within its convex region. Then SR^B with LJ potential is employed to solve problems such as high order tensile, shear, bending and crack propagation problems. In addition, MMM has been compared to several existing methods where MMM shows a better interface compatibility and performance through a benchmark example.

(5) Numerically demonstrated the effectiveness of the proposed surface summation rule SR^S by capturing surface effect in nanosized structures in 2D and 3D using quadrilateral and hexahedral elements. It is observed that the results of full atomistic (FA) simulation can be reasonably reproduced with MMM with less than 0.3% degrees of freedom of the original FA system. The good performance of SR^S is expected and is easy to understand since SR^S in 3D is, in fact, SR^B in 2D and SR^S in 2D is actually in SR^B 1D. Physically, this is because that for cubes, the boundary of 3D model is two-dimensional surface and the edge of a 2D surface is one-dimensional line.

(6) Discovered that MMM shows similar behavior to FEM under certain circumstances in its numerical convergence and error structure analysis with respect to linear element in 1D and 2D. The effect of the regularity and smoothness of the exact solution on the convergence behavior have been considered by applying different loading conditions. It is observed that MMM converges in an order of 2 and an order of 1 in the respective displacement (L_2) and energy (H_1) fields in 1D under the condition that the exact solution is C_0 smooth. In addition, the nonlinearity of interatomic potential on the convergence behavior is also studied. To explain the observed convergence phenomena, the respective discretization and sampling errors are analyzed for each tested element size.

6.2 FUTURE OUTLOOK

The proposed Multiresolution Molecular Mechanics with the novel summation rule SR^{MMM} are innovative and has been demonstrated to have advantages over existing approaches. However, there is room to improve the current work to better its performance and applicability to large-

scale systems of scientific interest. The improvement can be developed under the following directions:

(1) Iso-parametric analysis: the finite elements employed in this work mostly have regular shapes, i.e. rectangles and right-angled triangles. However, in general, element shapes are curved and irregular. In Section 3.8, we have employed irregular quadrilateral elements as an example to employ SR^{MMM} with irregular element. Even though SR^{MMM} can be directly performed, the shape function constructed is not consistent across element boundaries. Numerically, this may introduce extra errors. As in conventional FEM, isoparametric elements are proposed to overcome this technical difficulty, especially for high order element with curved boundaries. As such, the same idea can be adopted in MMM to not only have consistent shape functions but also standardize the calculation of SR^{MMM} . In addition, since the shape functions for the mapped element are, in general, rational not polynomial, numerical quadrature such as Gauss quadrature may not be exact in FEM. Similarly, SR^{MMM} is also not exact for rational shape function. The performance of SR^{MMM} for mapped elements needs to be tested. It is worthwhile to note that the order of numerical integration is often determined by the order of shape functions in local coordinates [125] in FEM. Analogously, the proposed summation rule SR^{MMM} can still be determined based on the shape functions defined via the “parent” elements such that the derivation in Chapter 2.0 may still be valid when it is performed with respect to local coordinates. Thus, the proposed summation rule may be reasonably expected to have good performance for mapped elements.

(2) Edge summation rule: As mentioned in Section 2.3, the energy of the atoms near element edges (called element edge atoms) within a potential cut-off distance does not follow the energy distribution of atoms in the bulk region (called element bulk atoms) (at least a potential

cut-off distance away for the edges) of each element. In this work, we have assumed that both element edge and bulk atoms have the same energy distribution. This assumption may not introduce large sampling errors for regular element shapes, as demonstrated in the work. However, it may introduce relatively large sampling error for elements with irregular shapes. As such, an edge summation rule SR^E may be designed to further reduce introduced sampling error. For instance, the energy of the atom at the middle of each element edge may be selected to sample and represent the energy of element edge atoms. Or, the proposed surface summation rule SR^S for surfaces can be directly employed for element edges since element edges are “surfaces” for each element.

(3) Many-body potentials: the potentials employed in this dissertation to test the theory of MMM are harmonic spring and the standard Lennard-Jones potentials. For more realistic applications, for instance, metals, many-body potentials such as embedded atom model (EAM) have to be employed. As discussed in Section 2.4, in principle, the proposed summation rule SR^{MMM} is independent of the interatomic potentials employed, similar to that quadrature rules employed do not depend on the constitutive relationships in FEM. Since any nonlinear interatomic potential can be well-approximated by a harmonic spring within its convex region, SR^{MMM} may be expected to be effective for many-body potentials. For cases where large deformation occurs, a relatively higher order of Gauss quadrature may be required for nonlinear constitutive relationships in FEM. Similarly, a higher order of SR^{MMM} may be employed for nonlinear interatomic potentials when large deformation is involved.

(4) Time scale and finite temperature: the proposed SR^{MMM} only coarse-grain the spatial scale and temporal scale is not considered. The numerical examples considered are at zero temperature. The time scale may be coarse-grained by incorporating techniques, for instance,

hyperdynamics – an approach for accelerating time in Molecular Dynamics (MD), into MMM. The acceleration in temporal space may be achieved by modifying MMM potential energy to reduce the energy barriers between metastable states in a way that reserves the characteristic dynamics of the system. Finite temperature may be considered by using the different thermostat such as Andersen Thermostat employed in MD simulation to maintain a system at constant temperature. Or, temperature-dependent interatomic potential may be utilized to consider thermal effect.

(5) Adaptive analysis: Adaptive mesh refinement is a key requirement for MMM to be accurate and efficient throughout the whole simulation process. Adaptive analysis has to be achieved in two directions: (I) keep molecular or atomistic description locally to track material defects movement and (II) coarse-grain the regions that was modelled by atomistic description and now are behind or not important to capture material defects. To achieve this, an efficient and accurate error estimator is definitely needed. The error indicators employed in adaptive FEM analysis may be borrowed and modified. Or, some quantity defined for solid state system may be employed. For instance, the centro-symmetry parameter is a useful measure of the local lattice disorder around an atom and can be used to characterize whether the atom is part of a perfect lattice, a local defect, or at a surface.

(6) Implementation and Parallelization: The implementation and parallelization is the final key step to enable MMM to solve large-scale problems of scientific and engineering interests. The ideas in implementing and parallelizing full MD to handle problems such loading balancing and effective communication may be borrowed and modified. This is possible since no continuum element is introduced and the framework of MMM is consistent with MD. One merit

of this framework consistency is that no differentiation between regions (such as local/nonlocal) is required.

To summarize, we have proposed the Multiresolution Molecular Mechanics with a novel summation rule SR^{MMM} to contribute the spatial length scale coarse-graining for general shape functions in coarse-grained molecular mechanics simulation. The validity and effectiveness of MMM have been demonstrated by numerical experiments. There remain improvements to be achieved, but the present work has laid down and contributed to the foundation of enabling coarse-grained molecular simulation to become a useful tool to firstly understand material deformation mechanism, then to discover new materials and as such to design materials by need.

BIBLIOGRAPHY

- [1] N. Hansen, "Hall–Petch relation and boundary strengthening," *Scripta Materialia*, vol. 51, pp. 801-806, 2004.
- [2] D. Wu, J. Zhang, J. Huang, H. Bei, and T.-G. Nieh, "Grain-boundary strengthening in nanocrystalline chromium and the Hall–Petch coefficient of body-centered cubic metals," *Scripta Materialia*, vol. 68, pp. 118-121, 2013.
- [3] B. Liu, D. Raabe, P. Eisenlohr, F. Roters, A. Arsenlis, and G. Hommes, "Dislocation interactions and low-angle grain boundary strengthening," *Acta Materialia*, vol. 59, pp. 7125-7134, 2011.
- [4] P. Sanders, C. Youngdahl, and J. Weertman, "The strength of nanocrystalline metals with and without flaws," *Materials Science and Engineering: A*, vol. 234, pp. 77-82, 1997.
- [5] F. F. Abraham, R. Walkup, H. Gao, M. Duchaineau, T. Diaz De La Rubia, and M. Seager, "Simulating materials failure by using up to one billion atoms and the world's fastest computer: Work-hardening," *Proceedings of the National Academy of Sciences*, vol. 99, p. 5783, 2002.
- [6] F. F. Abraham, R. Walkup, H. Gao, M. Duchaineau, T. Diaz De La Rubia, and M. Seager, "Simulating materials failure by using up to one billion atoms and the world's fastest computer: Brittle Fracture," *Proceedings of the National Academy of Sciences*, vol. 99, p. 5777, 2002.
- [7] M. J. Buehler, A. Hartmaier, H. Gao, M. Duchaineau, and F. F. Abraham, "Atomic plasticity: description and analysis of a one-billion atom simulation of ductile materials failure," *Computer methods in applied mechanics and engineering*, vol. 193, pp. 5257-5282, 2004.

- [8] S. Kohlhoff, P. Gumbsch, and H. Fischmeister, "Crack propagation in bcc crystals studied with a combined finite-element and atomistic model," *Philosophical Magazine A*, vol. 64, pp. 851-878, 1991.
- [9] E. B. Tadmor, M. Ortiz, and R. Phillips, "Quasicontinuum analysis of defects in solids," *Philosophical Magazine A*, vol. 73, pp. 1529-1563, 1996.
- [10] V. Shenoy, R. Miller, E. Tadmor, R. Phillips, and M. Ortiz, "Quasicontinuum models of interfacial structure and deformation," *Physical review letters*, vol. 80, pp. 742-745, 1998.
- [11] V. Shenoy, R. Miller, D. Rodney, R. Phillips, and M. Ortiz, "An adaptive finite element approach to atomic-scale mechanics--the quasicontinuum method," *Journal of the Mechanics and Physics of Solids*, vol. 47, pp. 611-642, 1999.
- [12] R. E. Rudd and J. Q. Broughton, "Concurrent coupling of length scales in solid state systems," *Computer Simulation of Materials at Atomic Level*, pp. 251-291, 2000.
- [13] J. Knap and M. Ortiz, "An analysis of the quasicontinuum method," *Journal of the Mechanics and Physics of Solids*, vol. 49, pp. 1899-1923, 2001.
- [14] L. Shilkrot, R. Miller, and W. Curtin, "Coupled atomistic and discrete dislocation plasticity," *Physical review letters*, vol. 89, p. 25501, 2002.
- [15] T. Belytschko and S. Xiao, "Coupling Methods for Continuum Model with Molecular Model," *International Journal for multiscale computational engineering*, vol. 1, 2003.
- [16] G. J. Wagner and W. K. Liu, "Coupling of atomistic and continuum simulations using a bridging scale decomposition," *Journal of Computational Physics*, vol. 190, pp. 249-274, 2003.
- [17] E. Weinan, B. Engquist, and Z. Huang, "Heterogeneous multiscale method: a general methodology for multiscale modeling," *Physical Review B*, vol. 67, p. 092101, 2003.
- [18] D. Qian, G. J. Wagner, and W. K. Liu, "A multiscale projection method for the analysis of carbon nanotubes," *Computer methods in applied mechanics and engineering*, vol. 193, pp. 1603-1632, 2004.

- [19] D. Qian and R. H. Gondhalekar, "A virtual atom cluster approach to the mechanics of nanostructures," *International Journal for multiscale computational engineering*, vol. 2, 2004.
- [20] L. Shilkrot, R. E. Miller, and W. A. Curtin, "Multiscale plasticity modeling: coupled atomistics and discrete dislocation mechanics," *Journal of the Mechanics and Physics of Solids*, vol. 52, pp. 755-787, 2004.
- [21] S. Xiao and T. Belytschko, "A bridging domain method for coupling continua with molecular dynamics," *Computer methods in applied mechanics and engineering*, vol. 193, pp. 1645-1669, 2004.
- [22] X. Li, "Multiscale modeling of the dynamics of solids at finite temperature," *Journal of the Mechanics and Physics of Solids*, vol. 53, pp. 1650-1685, 2005.
- [23] H. S. Park, E. G. Karpov, P. A. Klein, and W. K. Liu, "Three-dimensional bridging scale analysis of dynamic fracture," *Journal of Computational Physics*, vol. 207, pp. 588-609, 2005.
- [24] H. S. Park, E. G. Karpov, W. K. Liu[†], and P. A. Klein, "The bridging scale for two-dimensional atomistic/continuum coupling," *Philosophical Magazine*, vol. 85, pp. 79-113, 2005.
- [25] A. C. To and S. Li, "Perfectly matched multiscale simulations," *Physical Review B*, vol. 72, p. 035414, 2005.
- [26] S. Li, X. Liu, A. Agrawal, and A. C. To, "Perfectly matched multiscale simulations for discrete lattice systems: Extension to multiple dimensions," *Physical Review B*, vol. 74, p. 045418, 2006.
- [27] S. Tang, T. Y. Hou, and W. K. Liu, "A mathematical framework of the bridging scale method," *International Journal for Numerical Methods in Engineering*, vol. 65, pp. 1688-1713, 2006.
- [28] S. Badia, P. Bochev, J. Fish, M. Gunzburger, R. Lehoucq, M. Nuggehally, *et al.*, "A force-based blending model for atomistic-to-continuum coupling," *International Journal for multiscale computational engineering*, vol. 5, pp. 387-406, 2007.

- [29] J. Fish, M. A. Nuggehally, M. S. Shephard, C. R. Picu, S. Badia, M. L. Parks, *et al.*, "Concurrent AtC coupling based on a blend of the continuum stress and the atomistic force," *Computer methods in applied mechanics and engineering*, vol. 196, pp. 4548-4560, 2007.
- [30] R. E. Miller and E. B. Tadmor, "Hybrid continuum mechanics and atomistic methods for simulating materials deformation and failure," *MRS bulletin*, vol. 32, pp. 920-926, 2007.
- [31] P. T. Bauman, H. B. Dhia, N. Elkhodja, J. T. Oden, and S. Prudhomme, "On the application of the Arlequin method to the coupling of particle and continuum models," *Computational Mechanics*, vol. 42, pp. 511-530, 2008.
- [32] J. Y. Park and S. Im, "Adaptive nonlocal quasicontinuum for deformations of curved crystalline structures," *Physical Review B*, vol. 77, p. 184109, 2008.
- [33] M. L. Parks, P. B. Bochev, and R. B. Lehoucq, "Connecting atomistic-to-continuum coupling and domain decomposition," *Multiscale Model. Simul.*, vol. 7, pp. 362-380, 2008.
- [34] B. Eidel and A. Stukowski, "A variational formulation of the quasicontinuum method based on energy sampling in clusters," *Journal of the Mechanics and Physics of Solids*, vol. 57, pp. 87-108, 2009.
- [35] M. Gunzburger and Y. Zhang, "A quadrature-rule type approximation for the quasicontinuum method," *Multiscale Model. Simul.*, vol. 8, pp. 571-590, 2010.
- [36] Y. Zhang and M. Gunzburger, "Quadrature-rule type approximations to the quasicontinuum method for long-range interatomic interactions," *Computer methods in applied mechanics and engineering*, vol. 199, pp. 648-659, 2010.
- [37] L. Beex, R. Peerlings, and M. Geers, "A quasicontinuum methodology for multiscale analyses of discrete microstructural models," *International Journal for Numerical Methods in Engineering*, vol. 87, pp. 701-718, 2011.
- [38] X. Zeng, X. Wang, J. D. Lee, and Y. Lei, "Multiscale modeling of nano/micro systems by a multiscale continuum field theory," *Computational Mechanics*, vol. 47, pp. 205-216, 2011.

- [39] V. Iacobellis and K. Behdinin, "Multiscale coupling using a finite element framework at finite temperature," *International Journal for Numerical Methods in Engineering*, vol. 92, pp. 652-670, 2012.
- [40] Q. Yang, E. Biyikli, P. Zhang, R. Tian, and A. C. To, "Atom collocation method," *Computer methods in applied mechanics and engineering*, vol. 237–240, pp. 67-77, 2012.
- [41] L. Beex, R. Peerlings, and M. Geers, "A multiscale quasicontinuum method for dissipative lattice models and discrete networks," *Journal of the Mechanics and Physics of Solids*, 2013.
- [42] E. Tadmor, F. Legoll, W. Kim, L. Dupuy, and R. Miller, "Finite-temperature quasicontinuum," *Applied Mechanics Reviews*, vol. 65, p. 010803, 2013.
- [43] Q. Yang, E. Biyikli, and A. C. To, "Multiresolution molecular mechanics: Statics," *Computer methods in applied mechanics and engineering*, vol. 258, pp. 26-38, 2013.
- [44] L. Beex, R. Peerlings, and M. Geers, "A multiscale quasicontinuum method for lattice models with bond failure and fiber sliding," *Computer Methods in Applied Mechanics and Engineering*, vol. 269, pp. 108-122, 2014.
- [45] E. Biyikli, Q. Yang, and A. C. To, "Multiresolution Molecular Mechanics: Dynamics," *Computer methods in applied mechanics and engineering*, 2014.
- [46] X. H. Li, M. Luskin, C. Ortner, and A. V. Shapeev, "Theory-based benchmarking of the blended force-based quasicontinuum method," *Computer methods in applied mechanics and engineering*, vol. 268, pp. 763-781, 2014.
- [47] J. Marchais, C. Rey, and L. Chamoin, "Geometrically consistent approximations of the energy for the transition between nonlocal and local discrete models," *Computational Materials Science*, vol. 85, pp. 280-294, 2014.
- [48] L. Xiong, G. Tucker, D. L. McDowell, and Y. Chen, "Coarse-grained atomistic simulation of dislocations," *Journal of the Mechanics and Physics of Solids*, vol. 59, pp. 160-177, 2011.
- [49] L. Xiong, Q. Deng, G. J. Tucker, D. L. McDowell, and Y. Chen, "Coarse-grained atomistic simulations of dislocations in Al, Ni and Cu crystals," *International Journal of Plasticity*, vol. 38, pp. 86-101, 2012.

- [50] L. Xiong and Y. Chen, "Coarse-grained simulations of single-crystal silicon," *Modelling and Simulation in Materials Science and Engineering*, vol. 17, p. 035002, 2009.
- [51] E. Weinan, B. Engquist, X. Li, W. Ren, and E. Vanden-Eijnden, "Heterogeneous multiscale methods: a review," *Communications in computational physics*, vol. 2, pp. 367-450, 2007.
- [52] J. Wernik and S. A. Meguid, "Coupling atomistics and continuum in solids: status, prospects, and challenges," *International Journal of Mechanics and Materials in Design*, vol. 5, pp. 79-110, 2009.
- [53] R. E. Miller and E. Tadmor, "A unified framework and performance benchmark of fourteen multiscale atomistic/continuum coupling methods," *Modelling and Simulation in Materials Science and Engineering*, vol. 17, p. 053001, 2009.
- [54] W. A. Curtin and R. E. Miller, "Atomistic/continuum coupling in computational materials science," *Modelling and Simulation in Materials Science and Engineering*, vol. 11, p. R33, 2003.
- [55] B. Van Koten and M. Luskin, "Analysis of energy-based blended quasi-continuum approximations," *SIAM Journal on Numerical Analysis*, vol. 49, pp. 2182-2209, 2011.
- [56] J. S. Amelang and D. M. Kochmann, "Surface effects in nanoscale structures investigated by a fully-nonlocal energy-based quasicontinuum method," *Mechanics of Materials*, 2015.
- [57] J. Amelang, G. Venturini, and D. Kochmann, "Summation rules for a fully nonlocal energy-based quasicontinuum method," *Journal of the Mechanics and Physics of Solids*, 2015.
- [58] L. Beex, P. Kerfriden, T. Rabczuk, and S. Bordas, "Quasicontinuum-based multiscale approaches for plate-like beam lattices experiencing in-plane and out-of-plane deformation," *Computer Methods in Applied Mechanics and Engineering*, vol. 279, pp. 348-378, 2014.
- [59] L. Beex, R. Peerlings, and M. Geers, "A multiscale quasicontinuum method for dissipative lattice models and discrete networks," *Journal of the Mechanics and Physics of Solids*, vol. 64, pp. 154-169, 2014.

- [60] L. Beex, O. Rokoš, J. Zeman, and S. Bordas, "Higher - order quasicontinuum methods for elastic and dissipative lattice models: uniaxial deformation and pure bending," *GAMM - Mitteilungen*, vol. 38, pp. 344-368, 2015.
- [61] Q. Yang, E. Biyikli, and A. C. To, "Multiresolution molecular mechanics: convergence and error structure analysis," *Computer Methods in Applied Mechanics and Engineering*, vol. 269, pp. 20-45, 2014.
- [62] M. Dobson and M. Luskin, "Analysis of a force-based quasicontinuum approximation," *ESAIM: Mathematical Modelling and Numerical Analysis*, vol. 42, pp. 113-139, 2008.
- [63] R. E. Miller and E. B. Tadmor, "The quasicontinuum method: Overview, applications and current directions," *Journal of Computer-Aided Materials Design*, vol. 9, pp. 203-239, 2002.
- [64] W. K. Liu, E. Karpov, S. Zhang, and H. Park, "An introduction to computational nanomechanics and materials," *Computer methods in applied mechanics and engineering*, vol. 193, pp. 1529-1578, 2004.
- [65] H. S. Park and W. K. Liu, "An introduction and tutorial on multiple-scale analysis in solids," *Computer methods in applied mechanics and engineering*, vol. 193, pp. 1733-1772, 2004.
- [66] R. Sunyk and P. Steinmann, "On higher gradients in continuum-atomistic modelling," *International Journal of Solids and Structures*, vol. 40, pp. 6877-6896, 2003.
- [67] M. Arroyo and T. Belytschko, "Finite crystal elasticity of carbon nanotubes based on the exponential Cauchy-Born rule," *Physical Review B*, vol. 69, p. 115415, 2004.
- [68] X. Guo, J. Wang, and H. Zhang, "Mechanical properties of single-walled carbon nanotubes based on higher order Cauchy–Born rule," *International Journal of Solids and Structures*, vol. 43, pp. 1276-1290, 2006.
- [69] Y. Sun and K. Liew, "Application of the higher - order Cauchy - Born rule in mesh - free continuum and multiscale simulation of carbon nanotubes," *International Journal for Numerical Methods in Engineering*, vol. 75, pp. 1238-1258, 2008.

- [70] E. W. Wong, P. E. Sheehan, and C. M. Lieber, "Nanobeam mechanics: elasticity, strength, and toughness of nanorods and nanotubes," *Science*, vol. 277, pp. 1971-1975, 1997.
- [71] P. Poncharal, Z. Wang, D. Ugarte, and W. A. De Heer, "Electrostatic deflections and electromechanical resonances of carbon nanotubes," *Science*, vol. 283, pp. 1513-1516, 1999.
- [72] S. Cuenot, C. Frétiigny, S. Demoustier-Champagne, and B. Nysten, "Surface tension effect on the mechanical properties of nanomaterials measured by atomic force microscopy," *Physical Review B*, vol. 69, p. 165410, 2004.
- [73] R. Agrawal, B. Peng, E. E. Gdoutos, and H. D. Espinosa, "Elasticity size effects in ZnO nanowires— a combined experimental-computational approach," *Nano Letters*, vol. 8, pp. 3668-3674, 2008.
- [74] A. Asthana, K. Momeni, A. Prasad, Y. Yap, and R. Yassar, "In situ observation of size-scale effects on the mechanical properties of ZnO nanowires," *Nanotechnology*, vol. 22, p. 265712, 2011.
- [75] J.-Y. Kim, D. Jang, and J. R. Greer, "Crystallographic orientation and size dependence of tension–compression asymmetry in molybdenum nano-pillars," *International Journal of Plasticity*, vol. 28, pp. 46-52, 2012.
- [76] Y. Zhu, Q. Qin, F. Xu, F. Fan, Y. Ding, T. Zhang, *et al.*, "Size effects on elasticity, yielding, and fracture of silver nanowires: In situ experiments," *Physical review B*, vol. 85, p. 045443, 2012.
- [77] G. Jing, H. L. Duan, X. Sun, Z. Zhang, J. Xu, Y. Li, *et al.*, "Surface effects on elastic properties of silver nanowires: contact atomic-force microscopy," *Physical Review B*, vol. 73, p. 235409, 2006.
- [78] R. E. Miller and V. B. Shenoy, "Size-dependent elastic properties of nanosized structural elements," *Nanotechnology*, vol. 11, p. 139, 2000.
- [79] G. Cao and X. Chen, "Size dependence and orientation dependence of elastic properties of ZnO nanofilms," *International journal of solids and structures*, vol. 45, pp. 1730-1753, 2008.

- [80] X. Zhou, H. Zhou, X. Li, and C. Chen, "Size effects on tensile and compressive strengths in metallic glass nanowires," *Journal of the Mechanics and Physics of Solids*, vol. 84, pp. 130-144, 2015.
- [81] H. Liang, M. Upmanyu, and H. Huang, "Size-dependent elasticity of nanowires: nonlinear effects," *Physical Review B*, vol. 71, p. 241403, 2005.
- [82] V. B. Shenoy, "Atomistic calculations of elastic properties of metallic fcc crystal surfaces," *Physical Review B*, vol. 71, p. 094104, 2005.
- [83] L. Zhou and H. Huang, "Are surfaces elastically softer or stiffer?," *Applied Physics Letters*, vol. 84, pp. 1940-1942, 2004.
- [84] B. Arash, J.-W. Jiang, and T. Rabczuk, "A review on nanomechanical resonators and their applications in sensors and molecular transportation," *Applied Physics Reviews*, vol. 2, p. 021301, 2015.
- [85] J. Chaste, A. Eichler, J. Moser, G. Ceballos, R. Rurali, and A. Bachtold, "A nanomechanical mass sensor with yoctogram resolution," *Nature nanotechnology*, vol. 7, pp. 301-304, 2012.
- [86] M. Hanay, S. Kelber, A. Naik, D. Chi, S. Hentz, E. Bullard, *et al.*, "Single-protein nanomechanical mass spectrometry in real time," *Nature nanotechnology*, vol. 7, pp. 602-608, 2012.
- [87] J. Moser, J. Güttinger, A. Eichler, M. J. Esplandiu, D. Liu, M. Dykman, *et al.*, "Ultrasensitive force detection with a nanotube mechanical resonator," *Nature nanotechnology*, vol. 8, pp. 493-496, 2013.
- [88] X. Feng, C. White, A. Hajimiri, and M. L. Roukes, "A self-sustaining ultrahigh-frequency nanoelectromechanical oscillator," *Nature nanotechnology*, vol. 3, pp. 342-346, 2008.
- [89] L. G. Villanueva, R. B. Karabalin, M. H. Matheny, E. Kenig, M. C. Cross, and M. L. Roukes, "A nanoscale parametric feedback oscillator," *Nano letters*, vol. 11, pp. 5054-5059, 2011.

- [90] X. Feng, M. Matheny, C. Zorman, M. Mehregany, and M. Roukes, "Low voltage nanoelectromechanical switches based on silicon carbide nanowires," *Nano letters*, vol. 10, pp. 2891-2896, 2010.
- [91] R. Dingreville, J. Qu, and M. Cherkaoui, "Surface free energy and its effect on the elastic behavior of nano-sized particles, wires and films," *Journal of the Mechanics and Physics of Solids*, vol. 53, pp. 1827-1854, 2005.
- [92] J.-G. Guo and Y.-P. Zhao, "The size-dependent bending elastic properties of nanobeams with surface effects," *Nanotechnology*, vol. 18, p. 295701, 2007.
- [93] C. Lim and L. He, "Size-dependent nonlinear response of thin elastic films with nano-scale thickness," *International Journal of Mechanical Sciences*, vol. 46, pp. 1715-1726, 2004.
- [94] L. He, C. Lim, and B. Wu, "A continuum model for size-dependent deformation of elastic films of nano-scale thickness," *International Journal of Solids and Structures*, vol. 41, pp. 847-857, 2004.
- [95] H. Zhu and B. L. Karihaloo, "Size-dependent bending of thin metallic films," *International Journal of Plasticity*, vol. 24, pp. 991-1007, 2008.
- [96] C. Chen, Y. Shi, Y. Zhang, J. Zhu, and Y. Yan, "Size dependence of Young's modulus in ZnO nanowires," *Physical review letters*, vol. 96, p. 075505, 2006.
- [97] J. He and C. M. Lilley, "Surface effect on the elastic behavior of static bending nanowires," *Nano Letters*, vol. 8, pp. 1798-1802, 2008.
- [98] R. C. Cammarata, "Surface and interface stress effects in thin films," *Progress in surface science*, vol. 46, pp. 1-38, 1994.
- [99] H. Duan, J. Wang, Z. Huang, and B. Karihaloo, "Size-dependent effective elastic constants of solids containing nano-inhomogeneities with interface stress," *Journal of the Mechanics and Physics of Solids*, vol. 53, pp. 1574-1596, 2005.
- [100] H. S. Park, P. A. Klein, and G. J. Wagner, "A surface Cauchy–Born model for nanoscale materials," *International Journal for Numerical Methods in Engineering*, vol. 68, pp. 1072-1095, 2006.

- [101] H. S. Park and P. A. Klein, "Surface Cauchy-Born analysis of surface stress effects on metallic nanowires," *Physical Review B*, vol. 75, p. 085408, 2007.
- [102] H. S. Park and P. A. Klein, "A surface Cauchy-Born model for silicon nanostructures," *Computer methods in applied mechanics and engineering*, vol. 197, pp. 3249-3260, 2008.
- [103] M. Qomi, A. Aghaei, and A. Khoei, "Multi - scale modeling of surface effect via the boundary Cauchy – Born method," *International journal for numerical methods in engineering*, vol. 85, pp. 827-846, 2011.
- [104] A. Khoei and A. Aramoon, "A multi-scale modeling of surface effect via the modified boundary Cauchy–Born model," *Materials Science and Engineering: C*, vol. 32, pp. 1993-2000, 2012.
- [105] Q. Yang, E. Biyikli, P. Zhang, R. Tian, and A. C. To, "Atom collocation method," *Computer Methods in Applied Mechanics and Engineering*, vol. 237, pp. 67-77, 2012.
- [106] Q. Yang, E. Biyikli, and A. C. To, "Multiresolution molecular mechanics: statics," *Computer Methods in Applied Mechanics and Engineering*, vol. 258, pp. 26-38, 2013.
- [107] M. E. Gurtin and A. I. Murdoch, "A continuum theory of elastic material surfaces," *Archive for Rational Mechanics and Analysis*, vol. 57, pp. 291-323, 1975.
- [108] G. Yun and H. S. Park, "Surface stress effects on the bending properties of fcc metal nanowires," *Physical Review B*, vol. 79, p. 195421, 2009.
- [109] H. S. Park and P. A. Klein, "Surface stress effects on the resonant properties of metal nanowires: the importance of finite deformation kinematics and the impact of the residual surface stress," *Journal of the Mechanics and Physics of Solids*, vol. 56, pp. 3144-3166, 2008.
- [110] A. Khoei and P. Ghahremani, "Temperature-dependent multi-scale modeling of surface effects on nano-materials," *Mechanics of Materials*, vol. 46, p. 94, 2012.
- [111] A. Khoei, P. Ghahremani, and H. DorMohammadi, "Multi - scale modeling of surface effects in nano - materials with temperature - related Cauchy - Born hypothesis via the modified boundary Cauchy - Born model," *International Journal for Numerical Methods in Engineering*, vol. 97, pp. 79-110, 2014.

- [112] M. N. Esfahani, M. R. Sonne, J. H. Hattel, and B. E. Alaca, "Thermo-coupled Surface Cauchy–Born theory: An engineering finite element approach to modeling of nanowire thermomechanical response," *Mechanics of Materials*, vol. 94, pp. 46-52, 2016.
- [113] Q. Yang and A. C. To, "Multiresolution molecular mechanics: A unified and consistent framework for general finite element shape functions," *Computer Methods in Applied Mechanics and Engineering*, vol. 283, pp. 384-418, 2015.
- [114] E. Biyikli, Q. Yang, and A. C. To, "Multiresolution molecular mechanics: dynamics," *Computer methods in applied mechanics and engineering*, vol. 274, pp. 42-55, 2014.
- [115] H. Duan, J. Wang, and B. L. Karihaloo, "Theory of elasticity at the nanoscale," *Advances in applied mechanics*, vol. 42, pp. 1-68, 2009.
- [116] J. Wang, Z. Huang, H. Duan, S. Yu, X. Feng, G. Wang, *et al.*, "Surface stress effect in mechanics of nanostructured materials," *Acta Mechanica Sinica*, vol. 24, pp. 52-82, 2011.
- [117] A. M. Abazari, S. M. Safavi, G. Rezazadeh, and L. G. Villanueva, "Modelling the Size Effects on the Mechanical Properties of Micro/Nano Structures," *Sensors*, vol. 15, pp. 28543-28562, 2015.
- [118] M. Luskin and C. Ortner, "An Analysis of Node-Based Cluster Summation Rules in the Quasicontinuum Method," *SIAM Journal on Numerical Analysis*, vol. 47, p. 3070, 2009.
- [119] Y. Kulkarni, J. Knap, and M. Ortiz, "A variational approach to coarse graining of equilibrium and non-equilibrium atomistic description at finite temperature," *Journal of the Mechanics and Physics of Solids*, vol. 56, pp. 1417-1449, 2008.
- [120] W. K. Kim, M. Luskin, D. Perez, A. Voter, and E. Tadmor, "Hyper-QC: An accelerated finite-temperature quasicontinuum method using hyperdynamics," *Journal of the Mechanics and Physics of Solids*, vol. 63, pp. 94-112, 2014.
- [121] L. M. Dupuy, E. B. Tadmor, R. E. Miller, and R. Phillips, "Finite-temperature quasicontinuum: Molecular dynamics without all the atoms," *Physical Review Letters*, vol. 95, p. 060202, 2005.
- [122] O. Zienkiewicz, R. Taylor, and J. Zhu, "The finite element method: its basis and fundamentals. 2005," ed: Butterworth-Heinemann, 2005.

- [123] R. Tian, A. C. To, and W. K. Liu, "Conforming local meshfree method," *International Journal for Numerical Methods in Engineering*, vol. 86, pp. 335-357, 2011.
- [124] S. Timoshenko and J. Goodier, "Theory of Elasticity, McGraw-Hill, New York, 1970."
- [125] O. C. Zienkiewicz, R. L. Taylor, and J. Z. Zhu, *The Finite Element Method: Its Basis and Fundamentals: Its Basis and Fundamentals*: Elsevier Science, 2005.
- [126] S. C. Brenner and L. R. Scott, *The mathematical theory of finite element methods* vol. 15: Springer, 2008.
- [127] G. Liu and Y. Gu, *An introduction to meshfree methods and their programming*: Springer, 2005.
- [128] P. Lin, "Convergence analysis of a quasi-continuum approximation for a two-dimensional material without defects," *SIAM Journal on Numerical Analysis*, vol. 45, pp. 313-332, 2007.